FACULDADE DE ENGENHARIA DA UNIVERSIDADE DO PORTO

# Optimization of submerged-arc welding process in wind tower manufacturing

**Mihai-Alexandru Popescu**




Doctoral Program in Mechanical Engineering

Supervisor: Prof. Mário Augusto Pires Vaz

Co-supervisor: Prof. Francisco José Malheiro Queirós de Melo

May 6, 2022

© Mihai-Alexandru Popescu, 2022

# Optimization of submerged-arc welding process in wind tower manufacturing

**Mihai-Alexandru Popescu**

Doctoral Program in Mechanical Engineering

Approved in oral examination by the committee:

Chair: Prof. Armando Carlos Figueiredo Coelho de Oliveira
External Examiner: Prof. Hernâni Miguel Reis Lopes
External Examiner: Prof. Paulo Alexandre Gonçalves Piloto
Examiner: Prof. Pedro Miguel Guimarães Pires Moreira
Supervisor: Prof. Mário Augusto Pires Vaz

May 6, 2022

# Abstract

The economic implications of manufacturing processes depend mainly on planned outcomes and production management. In the large-scale production of steel structures, manufacturing errors raise the overall production costs and can cause unplanned delays. This applies to tubular steel towers used as the support structure for wind turbines as well.

The geometrical characteristics of tubular steel towers play an important role in the overall structural integrity of the wind turbine. When parts of the towers are produced with geometric errors that exceed the allowable tolerances, there is a need for them to be mended. This implies an extra re-working step that appears in the production process, which delays the delivery date, raises overall costs, and keeps qualified workers from attending to other important tasks. Because submerged-arc welding is employed in the manufacturing of steel towers, a main cause for the geometrical errors, manifesting as distortions, is welding residual stresses.

Residual stresses resulting from welding processes are influenced by welding parameters, the geometry of the part, and the chemical composition of the materials used. In this context, reducing the overall cost of manufacturing, while at the same time maintaining the quality standards implies the necessity of optimizing the welding process and procedures. The Contour Method was used in order to assess the stress state of the parts caused by different welding parameters and use these results as a basis for optimizing the welding process.

**Keywords**: Production management, Wind turbines, Structural integrity, Tubular steel towers, Submerged-arc welding, Residual stress.

# Resumo

As implicações económicas dos processos de fabrico dependem principalmente dos resultados planeados e da gestão da produção. Na produção de estruturas de aço em grande escala, os erros de fabrico aumentam os custos gerais de produção e podem causar atrasos não planeados. Isto aplica-se também às torres tubulares em aço que são utilizadas como estrutura de suporte para turbinas eólicas.

As características geométricas das torres tubulares em aço desempenham um papel importante na integridade estrutural da turbina eólica. Quando partes das torres são produzidas com erros geométricos que excedem as tolerâncias permitidas, é necessário que sejam reparadas. Isso implica uma etapa extra de retrabalho que aparece no processo de produção, atrasando a data de entrega, aumentando os custos gerais e impedindo que trabalhadores qualificados realizem outras tarefas importantes. Como a soldadura por arco submerso é empregada no fabrico de torres de aço, uma das principais causas dos erros geométricos, que se manifestam como distorções, são as tensões residuais de soldadura.

As tensões residuais de soldadura são influenciadas pelos parâmetros de soldadura, a geometria da peça e a composição química dos materiais usados. Neste contexto, reduzir o custo global de fabricação e, ao mesmo tempo, manter os padrões de qualidade, implica na necessidade de otimizar o processo e os procedimentos de soldadura. O Método do Contorno foi utilizado com o objetivo de avaliar o estado de tensão que permanece nas peças em resultado dos diferentes parâmetros de soldadura. Utilizar os resultados como base para otimizar o processo de soldadura é também um dos objetivos deste trabalho.

**Palavras-chave**: Gestão da produção, Turbinas eólicas, Integridade estrutural, Torres tubulares em aço, Soldadura por arco submerso, Tensões residuais.

# Acknowledgements

I would like to take this opportunity to express my sincere gratitude for all the help and support that I benefited from during the preparation of this work. This thesis would not have been possible to complete without the guidance, encouragement, and recommendations of my supervisors, Prof. Mário Augusto Pires Vaz and Prof. Francisco José Malheiro Queirós de Melo.
This work was financed by Programa Operacional Regional do NORTE, Operation NORTE-08-5369-FSE-000046, co-funded by the European Social Fund (FSE) through NORTE 2020.
Additionally, I would like to thank Tegopi Metalomecânica S.A. and ASM Metalomecânica S.A for their interest and support throughout, especially Eng. Alberto J.G. da Silva Malafaya Baptista, Eng. Thiago M.C. Chaves, Mr. Carlos M. da Silva, and all the wonderful people that I met during my time spent at Tegopi, that made me feel welcomed and shared their vast knowledge and experience with me.

Other contributors that have my sincere gratitude are :

- Dr. Behzad Farahani (LOME, INEGI)
- Eng. Francisco Barros (LOME, INEGI)
- Dr. Pedro Sousa (LOME, INEGI)
- Prof. Miguel Figueiredo (LET, DEMec, FEUP)
- Eng. Emília Soares (DEMec, FEUP)
- Mr. Rui Silva (LET, DEMec, FEUP)
- Eng. Nuno Viriato (LOME, INEGI)
- Mr. Andre Alves (DEMec, FEUP)
- Mr. Pedro Falcao (DEMec, FEUP)
- Mr. Domingos Carvalho (DEMec, FEUP)
- Prof. Paula Braga da Silva (UTAD)
- Prof. Jose Correia (FEUP)
- Dr. Raul Moreira (FEUP)
- Dr. Hamed Akhavan (INEGI, FEUP)
- Dr. Shayan Eslami

Besides this, I would like to offer my unquantifiable gratitude to all the people that supported me during this endeavor, my family and friends, Eng. Alexandru Zăbavă, Eng. Daniela Zăbavă, and Mustafa Ailin, my previous professors and supervisors, Prof. Cosmin Filip (OUC), Prof. Cornel Ciurea (OUC), Prof. Mirela Popa (OUC), Prof. Fatih Cetişli (PAU), Prof. Cemal Meran (PAU), Prof. Alina Diana Codreanu, Prof. Cristiana Crivăţ, and Prof. Elena Felicia Cărbune, my beloved parents, Maria and Florin, and my wife, Gislaine, for which no praise can be too high, and without whose constant and unwavering support this would not have been possible.

Mihai-Alexandru Popescu

*"There is nothing impossible to him who will try."*

Alexander the Great

# Contents


**1 Introduction** **1**
- 1.1 Scope . . . 2
- 1.2 Objectives . . . 2
- 1.3 Location and duration . . . 3
  - 1.3.1 About Tegopi . . . 4
- 1.4 Thesis structure . . . 4

**2 State of the Art** **5**
- 2.1 Introduction . . . 5
- 2.2 History of windmills . . . 10
  - 2.2.1 European windmills . . . 11
  - 2.2.2 Economic impact . . . 15
  - 2.2.3 Technological developments . . . 16
  - 2.2.4 Wind turbines in The New World . . . 17
  - 2.2.5 Wind powered electrical generators . . . 18
- 2.3 Wind resources . . . 19
- 2.4 Horizontal axis wind turbines . . . 23
  - 2.4.1 Betz's Elementary Momentum Theory . . . 25
  - 2.4.2 Wind turbine components . . . 28
  - 2.4.3 Typical tower production cycle . . . 30
- 2.5 Submerged-arc welding . . . 36
  - 2.5.1 Origins and development . . . 37
  - 2.5.2 The process . . . 38
  - 2.5.3 Principles . . . 39
  - 2.5.4 Welding parameters . . . 40
  - 2.5.5 Weld defects . . . 43
- 2.6 Residual stress . . . 46
  - 2.6.1 Problem definition . . . 52
  - 2.6.2 Weldability . . . 55
  - 2.6.3 Distortions . . . 57
  - 2.6.4 Welding residual stress and distortion control methods . . . 60
- 2.7 Experimental techniques for assessing welding residual stress . . . 62
  - 2.7.1 Objective . . . 62
  - 2.7.2 Methodology . . . 63
  - 2.7.3 Results . . . 67
  - 2.7.4 Conclusion . . . 72
- 2.8 Summary . . . 73

**3 Materials and methods** **75**
3.1 Introduction . . . 75
3.2 Structural Steel . . . 75
3.2.1 Material properties . . . 76
3.2.2 Mechanical properties . . . 79
3.2.3 Thermal properties . . . 80
3.3 Experimental work in Residual Stresses and Post-Welding Metallurgy . . . 86
3.3.1 The Contour method . . . 86
3.3.2 Microstructure and Macrostructure analysis and comparison . . . 91
3.3.3 Hardness test . . . 95
3.3.4 Charpy Impact test . . . 97
3.3.5 Geometry Acquisition and 3D Modelling of a Wind Tower using a 3D Laser Scanning Technology . . . 100

**4 Results and discussion** **103**
4.1 Introduction . . . 103
4.2 Residual Stress measurements . . . 103
4.3 Micro-structure and Macro-structure analysis . . . 107
4.4 Hardness test . . . 114
4.5 Charpy Impact test . . . 122
4.6 3D LSS . . . 126

**5 Conclusions and Future Work** **129**
5.1 Conclusions . . . 129
5.2 Future Work . . . 131

**References** **133**

**A** **141**

# List of Figures


1.1 Location map . . . 3

2.1 Gross electricity generation from renewable sources EU-28 1990-2017 . . . 6
2.2 Primary production of energy from renewable sources, EU-28, 1990-2017 . . . 7
2.3 Primary production of energy from renewable sources EU-28 1990-2017 . . . 7
2.4 Share of electricity from renewable sources 2019 . . . 8
2.5 Renewable sources generating electricity in the EU 2019 . . . 8
2.6 Electricity generation in the EU 1990-2020 . . . 9
2.7 Inland consumption of fossil fuels 2005-2020 . . . 9
2.8 Electricity from renewable sources 2020 . . . 10
2.9 Dutch windmill cross-section. . . . 14
2.10 Idealized atmospheric circulations. . . . 20
2.11 Local mean power density variation Porto area. . . . 21
2.12 Local mean wind speed variation Porto area. . . . 21
2.13 Installed capacity per district and autonomous region 2020. . . . 22
2.14 a.) Horizontal Axis Wind energy converter b.) schematic of the turbine blade assembly and nacelle . . . 23
2.15 Wind turbine diagram. . . . 24
2.16 Average turbine nameplate capacity, hub height, and rotor diameter for land-based wind projects in the United States. . . . 25
2.17 Flow conditions due to the extraction of mechanical energy from a free-stream air flow, according to the elementary momentum theory. . . . 27
2.18 Ideal power coefficient based on $v_2/v_1 ratio$. . . . 27
2.19 Nacelle layout GE Energy 1.x-100 wind turbine. . . . 29
2.20 Steel sheet, after being bevelled and before rolling. Courtesy of Tegopi. . . . 31
2.21 A large tower section. Courtesy of Tegopi. . . . 31
2.22 Steel sheet being rolled and tack welded. Courtesy of Tegopi. . . . 32
2.23 Shells after welding. Courtesy of Tegopi. . . . 32
2.24 Flanges. Courtesy of Tegopi. . . . 33
2.25 Shell on rollers. Courtesy of Tegopi. . . . 33
2.26 View from inside of a section (multiple shells being welded). Courtesy of Tegopi. 34
2.27 Completed section. Courtesy of Tegopi. . . . 34
2.28 Motofil welding robot with Miller power sources. Courtesy of Tegopi. . . . 35
2.29 ESAB welding robot (a), Miller controllers for Motofil robot (b), Motofil control panel (c). Courtesy of Tegopi. . . . 35
2.30 ESAB controllers . . . 36
2.31 SAW Process diagram. . . . 37
2.32 SAW principles . . . 40

2.33 Electrode polarity effect. . . . 41
2.34 Welding current effect. . . . 41
2.35 Electrode diameter effect . . . 41
2.36 Arc voltage effect. . . . 42
2.37 Welding speed effect. . . . 42
2.38 Electrode angle effect. . . . 44
2.39 Longitudinal and transverse residual stresses in centre cross-sections of rectangular plate with centric weld, analytical and experimental results. . . . 47
2.40 Longitudinal and transverse shrinkage, angular and bending shrinkage of rectangular plate with single- side welded centric jointing seam. . . . 48
2.41 Decoupling and mutual influence of temperature field, stress and deformation field and microstructural state field. . . . 49
2.42 Plastic zone and local stress-strain cycles in quasi-stationary temperature field of moving heat source. . . . 50
2.43 Example of temperature field isotherms around welding heat source moving uniformly and linearly in an infinite plate. . . . 50
2.44 Temperature field around moving line source in plates of different materials, equal heat output $q$ and source velocity $v$. . . . 51
2.45 Parameters with major influence on strength of welded joints (primarily heat affected zone) constituting part of their weldability. . . . 52
2.46 Three bar analogy. Room temperature (a); middle bar heated (b); room temperature middle bar disconnected (c); room temperature middle bar connected (d). . . . 53
2.47 Existing approach to distortion control. . . . 54
2.48 New proposed distortion control method. . . . 55
2.49 Definition of the term "weldability". . . . 56
2.50 Extended graph of Figure 2.41 emphasizing the influence of microstructural transformation; after Buchmayr and Kirkaldy. . . . 57
2.51 Types of distortions. . . . 59
2.52 Cylindrical shell deformations. . . . 59
2.53 Rotational and deflective deformations. . . . 59
2.54 PRISMA flow diagram . . . 66
2.55 The principle of the hole-drilling method. . . . 69
2.56 The principle of the contour method. . . . 70
2.57 The principle of the split ring method. . . . 72

3.1 Door cut-out extracted from blueprint. Courtesy of Tegopi. . . . 76
3.2 Doorframe after welding. . . . 77
3.3 Sample 1. . . . 77
3.4 Sample 2. . . . 77
3.5 Stress-strain relationship for carbon steel at elevated temperatures . . . 80
3.6 Reduction factors for stress-strain relationship of carbon steel at elevated temperatures. . . . 82
3.7 Stress-strain relationship of S355 at elevated temperatures. . . . 82
3.8 Relative thermal elongation of carbon steel. . . . 83
3.9 Specific heat of carbon steel. . . . 84
3.10 Thermal conductivity of carbon steel. . . . 85
3.11 Superposition principle for the contour method. Stresses are plotted on one quarter of the original body. . . . 87
3.12 Specimen 1 extracted from Sample 1. . . . 87

3.13 Specimen 2 extracted from Sample 2. . . . . 88
3.14 Specimen 1 from door cut-out prepared for EDM cutting. . . . . 88
3.15 ONA AF35 EDM machine at Iteum. . . . . 89
3.16 Specimen 1 after cutting. . . . . 89
3.17 Specimen 2 after cutting. . . . . 90
3.18 Specimen 1 during topography measurement at CATIM. . . . . 90
3.19 Specimen 1 during cutting. . . . . 91
3.20 Struers RotoPol-21. . . . . 92
3.21 Second Struers rotary polishing unit. . . . . 92
3.22 Specimen 1 after polishing. . . . . 93
3.23 Specimen 2 after polishing. . . . . 93
3.24 Zeiss Axiophot optical microscope . . . . . 94
3.25 Specimen 1 numbered locations. . . . . 94
3.26 Specimen 2 numbered locations. . . . . 95
3.27 Vickers test principle. . . . . 96
3.28 Wolpert Dia testor 2 RC. . . . . 96
3.29 Specimen 1 Hardness measurement points. . . . . 97
3.30 Specimen 2 Hardness measurement points. . . . . 97
3.31 Sample 1 Charpy specimen locations. . . . . 98
3.32 Sample 2 Charpy specimen locations. . . . . 99
3.33 Impact testing setup with the cooling device. . . . . 100
3.34 3D LSS setup. . . . . 101
3.35 3D LSS setup mounted. . . . . 101
3.36 3D LSS setup 2. . . . . 102

4.1 Sample 1 raw CMM measurements . . . . . 104
4.2 Sample 2 raw CMM measurements . . . . . 104
4.3 Averaged surfaces resulting from the averaged points for Sample 2. . . . . 105
4.4 Resulting averaged smooth surface for Sample 2. . . . . 105
4.5 3D residual stress profile for Sample 2. . . . . 106
4.6 2D residual stress profile for Sample 2. . . . . 106
4.7 Macro-structure Specimen 1. . . . . 108
4.8 Macro-structure Specimen 2. . . . . 108
4.9 Base metal Specimen 1 Location 1 (magnification 10x, scale 100 µm). . . . . 109
4.10 Transition zone between HAZ-Weld metal Specimen 1 Location 2 (magnification 5x, scale 200 µm). . . . . 109
4.11 HAZ Specimen 1 Location 3 (magnification 50x, scale 50 µm). . . . . 110
4.12 Weld metal Specimen 1 Location 5 (magnification 5x, scale 200 µm). . . . . 110
4.13 Base metal Specimen 2 Location 1 (magnification 10x, scale 100 µm). . . . . 111
4.14 Transition zone between Base metal-HAZ-Weld metal Specimen 2 Location 7 (magnification 5x, scale 200 µm). . . . . 111
4.15 HAZ Specimen 2 Location 2 (magnification 50x, scale 50 µm). . . . . 112
4.16 Weld metal Specimen 2 Location 3 (magnification 5x, scale 200 µm). . . . . 112
4.17 HAZ areas of both Specimens; Scale 200µm . . . . . 113
4.18 HV values Sample 1 Line 1. . . . . 115
4.19 HV values Sample 1 Line 2. . . . . 115
4.20 HV values Sample 1 Line 3. . . . . 116
4.21 HV values Sample 1 Line 4. . . . . 116
4.22 HV values Sample 2 Line 1. . . . . 117

4.23 HV values Sample 2 Line 2. . . . . 117
4.24 HV values Sample 2 Line 3. . . . . 118
4.25 HV values Sample 2 Line 4. . . . . 118
4.26 HV values HAZ Sample 1. . . . . 119
4.27 HV values HAZ Sample 2. . . . . 119
4.28 Hardness values comparison. . . . . 120
4.29 3D Hardness profiles Sample 1. . . . . 121
4.30 3D Hardness profiles Sample 2. . . . . 121
4.31 The energy absorbed/temperature curve for A type specimens at -20°C, -40°C, -60°C,-80°C. . . . . 124
4.32 Energy absorbed for A type specimens at -20°C, -40°C, -60°C,-80°C and B type specimens at- 20°C. . . . . 124
4.33 Fracture surface of Charpy test pieces A4 at -20°C. . . . . 125
4.34 Fracture surface of Charpy test pieces B1 at -20°C. . . . . 125
4.35 Fracture surface of Charpy Impact test pieces A1 at -40°C, -60°C and -80°C. . . 126
4.36 A-9-meter-long cylindrical part of a wind tower section. . . . . 126
4.37 A 3D view of the tower profile and b) a top view of the tower with its dimensions obtained by 3D LSS. . . . . 127

# List of Tables


2.1 Thermal efficiency factor $k$ of welding processes. . . . . 51
2.2 Manufacturing measures. . . . . 61
2.3 Initial search terms and results . . . . . 64
2.4 Search results after refinement . . . . . 64
2.5 Assigned numbers for primary studies . . . . . 65
2.6 Data extracted from studies . . . . . 66
2.7 Data extracted from primary studies . . . . . 68

3.1 Chemical composition of S355 J0+N. . . . . 78
3.2 Chemical composition of S355 J2+N. . . . . 78
3.3 Toughness properties of S355J0+N and S355 J2+N. . . . . 78
3.4 Chemical composition of the flux used in the welding process. . . . . 78
3.5 Chemical composition of the wires used in the welding process. . . . . 78
3.6 Mechanical properties of the flux-wire combination as welded. . . . . 78
3.7 Nominal values of yield strength fy and ultimate tensile strength fu for hot rolled structural steel. . . . . 79
3.8 Stress-strain relationship for carbon steel at elevated temperatures . . . . . 81
3.9 Reduction factors for stress-strain relationship of carbon steel at elevated temperatures. . . . . 81
3.10 Charpy specimen type and and location. . . . . 98

4.1 Impact values Sample 1. . . . . 122
4.2 Impact values Sample 2. . . . . 123
4.3 Impact values Sample 1 at lowered temperatures. . . . . 123

A.1 Stress-strain relationship of S355 at elevated temperatures. . . . . 142

# Abbreviations

| | |
|---|---|
| AC | Alternative current |
| ANN | Artificial neural network |
| CGSC | Coarse-grained supercritical zone |
| CMM | Coordinate Measuring Machine |
| CNC | Computerized Numerical Control |
| CWM | Computational welding mechanics |
| BM | Base metal |
| DC | Direct current |
| DCEN | Direct Current Electrode Negative |
| DCEP | Direct Current Electrode Positive |
| DHD | Deep-hole drilling |
| EDM | Electrical discharge machining |
| EN | European Norm |
| FE | Finite element |
| FEA | Finite element analysis |
| FEM | Finite element method |
| FGSC | Fine-grained supercritical zone |
| HAWT | Horizontal axis wind turbine |
| HAZ | Heat affected zone |
| HDM | The hole drilling method |
| IC | Intercritical zone |
| ISO | International Organization for Standardization |
| KV/T | The energy absorbed/temperature curve |
| LCR | Longitudinal critically refracted waves |
| LN2 | Liquid Nitrogen |
| LSS | Laser scanning system |
| MAG | Metal Active Gas welding |
| MIG | Metal Inert Gas welding |
| MMA | Manual Metal Arc welding |
| OM | Optical microscopy |
| PRISMA | Preferred Reporting Items for Systematic Reviews and Meta-Analyses |
| PSR | Primary slice removal mapping |
| SAW | Submerged-arc welding |
| SC | Subcritical zone |
| TIG | Tungsten Inert Gas welding |
| VWT | V: Charpy V-notch – W: notch in weld metal – T: notch through the thickness |
| VHT | V: Charpy V-notch – H: notch in heat affected zone – T: notch through the thickness |
| WEDM | Wire Electrical discharge machining |
| WM | Weld metal |
| 2D | Two dimensional |
| 3D | Three dimensional |

# Chapter 1

# Introduction

Reducing costs while at the same time maintaining high-quality standards requires the careful planning of the entire production process taking into account all possible mishaps that can occur, which can prove to be a difficult task. When unforeseen circumstances occur, they derail the entire process and can lead to delays in delivery and an increase in total costs. Moreover, when working with steel structures that need to behave in a reliable mode in regards to fatigue endurance, extra care needs to be taken during all steps of the production process. Wind turbines are subjected to a large number of loads, some of them steady, such as a steady wind stream, or unsteady loads, such as crosswinds and wind turbulence. Due to the cyclical nature of the loading conditions, the tower itself needs to behave well in regard to fatigue. One of the main by-products of the welding process is welding residual stress, and while compressive residual stress is beneficial, tensile residual stress is very detrimental to steel structures and can lead to a shorter lifespan, especially when constantly subjected to cyclical loading. To reduce production costs and time, it is necessary to assess the welding residual stress present in the parts after welding and its effects, in order to prevent distortions and achieve a product that will have a long service life [1, 2].

> "Most designers think that welding is related to black magic . . . A few do try to adjust their designs to help the welding engineers, but when they look into the subject, they find it too confusing and so abandon hope." [3]

## 1.1 Scope

This Ph.D. was developed in an industrial framework in partnership with TEGOPI – Indústria Metalomecânica S.A. A subject was proposed in accordance with the long-term goals of the company to streamline production and solve a problem that the company was facing. Unplanned outcomes in the form of large distortions after welding have a large impact on the production process, and there is a need to rectify the parts and bring them within acceptable tolerances. This in turn causes major delays when occurring often enough. Therefore, in order to ascertain the reasons for the unplanned and unpredictable distortions, the contour method provides the necessary basis for assessing the welding residual stress present in the parts.

## 1.2 Objectives

The economic considerations of production processes are of the highest importance for any manufacturing company and therefore when the process is stalled or prolonged by unforeseen circumstances this reduces profit margins and the quality of the end products. Considering these factors, the objective of this study is to optimize the production process by removing, reducing, or predicting distortions. In order to investigate the cause of the unpredictable distortions, there is a need to optimize the main part of the production process, namely the submerged-arc welding process.

To achieve this proposed optimization it is necessary to measure and understand the stress state present in the parts after welding and characterize the changes that occur.

The initial outline of the project was to produce welded specimens that vary the welding parameters individually, to their respective range extremes according to the internal welding specifications of the company, and by using the contour method to assess which combination of parameters produces the maximum and minimum residual stresses.

Parallel to this approach, a 3D Laser geometry acquisition system was proposed that would permit measuring the distortions present in the parts after welding, which combined with recorded welding parameters and other geometric characteristics would provide the basis for setting up an Artificial Neural Network (ANN) to predict future distortions.

## 1.3 Location and duration

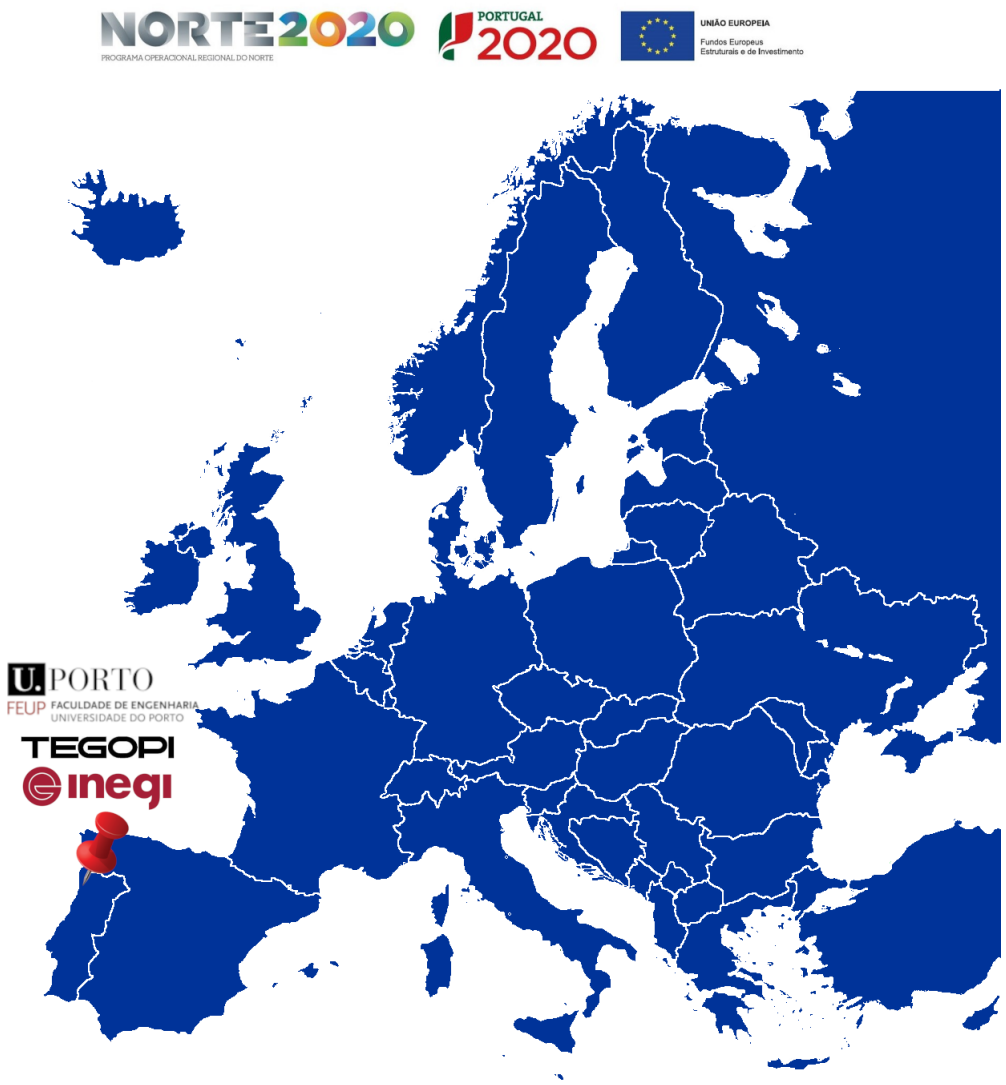



Figure 1.1: Location map

This work was mainly developed at two locations in Portugal; the primary location was Faculdade de Engenharia da Universidade do Porto (FEUP) in Porto, Portugal and the second one was TEGOPI – Indústria Metalomecânica S.A. located in Vila Nova de Gaia. The project began in May 2017 at FEUP and since April 2018 at Tegopi, with time being spent between the two locations. Additionally, to these main locations, smaller tasks have been performed with the support of INEGI as well as with other institutions. Tegopi provided the subject topic, representing one of the issues that occur during production and a limited number of welded samples. Unfortunately, due to financial issues, Tegopi withdrew from the project in October 2019. Subsequent samples

were generously provided by A. Silva Matos Industries.

### 1.3.1 About Tegopi

The main body of work and analysis is developed in collaboration with “TEGOPI – Indústria Metalomecânica S.A.”, a company from Porto, Portugal. Established in 1946 as a privately owned limited company, "Teixeira Gomes  Pinho, Lda". In the mid-60s, large projects in the fields of petrochemical, cellulose, and cement, positioned the company in the spectrum of steelworks, including design, fabrication, and commercialization of traveling, portal, and semi-portal cranes (rolling bridges), becoming market leaders within a few years, which continues to this day. In 1988, the company became a publicly-traded company and changes its name to "TEGOPI - Indústria Metalomecânica, SA" and two years later, part of its capital stock is purchased by two other companies, "Francisco António Fernandes, SA" (FAF) and "Grupo Quintas  Quintas". In 1993, the latter bought the shares of FAF, becoming the main shareholder, and one year later, the Quintas  Quintas Group held 100% of the capital stock. From this moment onwards, TEGOPI became more and more involved in exports, above all dedicating itself to new ranges of production: welded components, lifting and moving equipment, wind energy converter steel structures, and electric equipment modules. The wind tower support structures represented about 70% of their orders portfolio in 2018 and their products can be seen in countless wind farms all over the globe. The company provides lifting and moving equipment, steel structures, wind towers, and welded components [4].

## 1.4 Thesis structure

The thesis begins with the introduction and definition of the objectives included in Chapter 1. The state of the art is presented in Chapter 2, which provides relevant information on horizontal axis wind turbines (HAWT) and submerged-arc welding (SAW) as well as the impact of welding parameters on the characteristics and properties of the weld. A description of the materials and methods involved is provided in Chapter 3. In Chapter 4 the material and testing method are presented. Conclusions, general remarks, and a future perspective of the work are provided in Chapter 5.

# Chapter 2

# State of the Art

This chapter is devoted to describing the state of the art in what concerns energy production from wind turbines due to the fact that the thesis subject is about welding of tubular steel towers that are the support structures of wind turbines. The chapter is divided in two main parts, the first part is dedicated to describing the evolution of wind turbines and the second part to the welding process used in the manufacturing process.

## 2.1 Introduction

Wind has played a part in the history of humankind since the dawn of time, playing an even more important role in recent years due to the ill effects of fossil fuels on climate change, their finite nature, and an ever-increasing demand for energy. Harvesting wind power to produce electrical energy has proved to be a viable alternative, with renewable energy being produced in the European Union (EU-28) increasing by two-thirds between 2007 and 2017. The quantity of renewable energy produced in the EU-28 increased overall by 64% between 2007 and 2017, with a 5.1% increase per year. In 2017 electric energy generated by wind power became, for the first time, the primary source of generated renewable energy followed closely by hydroelectric power, as shown in Figure 2.1. In 2017 renewable energy sources represented 17.5% of total energy consumed in the EU, on the path to the 2020 target of 20%, shown in Figure 2.2 per country, the primary

production of renewable energy within the EU-28 was 226.5 million tons of oil equivalent (Mtoe) as can be seen in Figure 2.3 [5, 6].

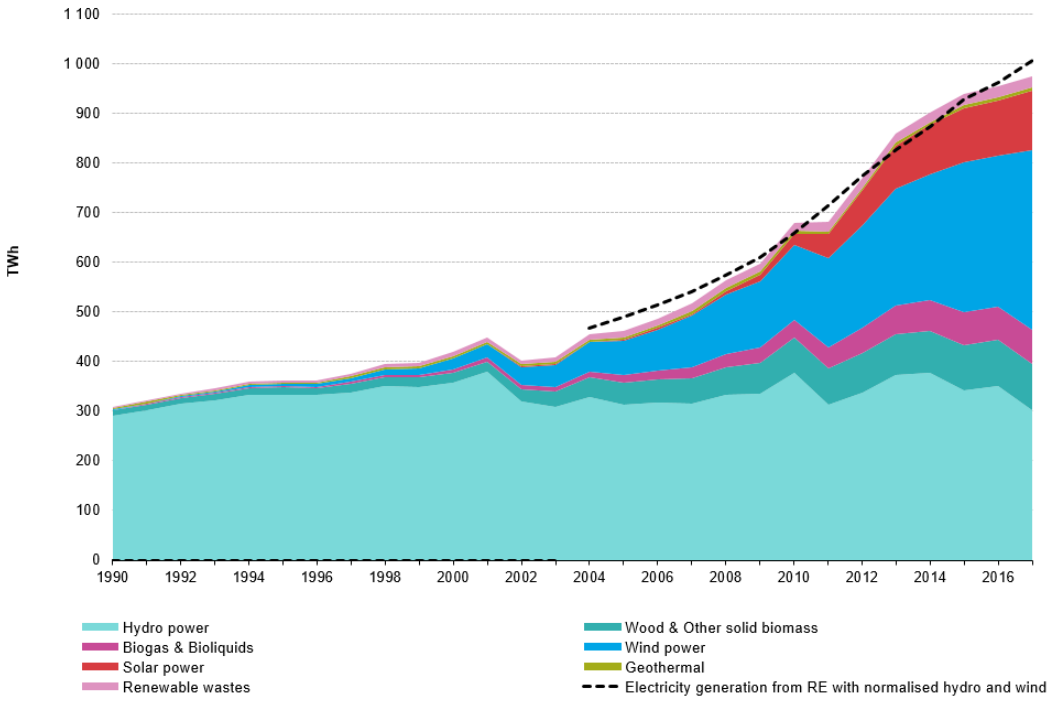



Figure 2.1: Gross electricity generation from renewable sources EU-28 1990-2017

Total energy consumption in the EU generated from renewable sources reached almost one-third (32%) in 2018 with wind energy being the highest contributor (36%). For 2019, this figure increased to 34% (Figure 2.4), with hydroelectric and wind accounting for 35% each (Figure 2.5). In 2020 the amount of renewable energy consumed by the EU reached 37.5% as shown in Figure 2.8. With the new European Green Deal, came the highly ambitious goal of becoming the world‘s first carbon-neutral continent by 2050.

These point to an increased demand for wind energy converters. In order to provide a longer service life and reduce maintenance costs, a need for more structurally sound structures arises. In order to achieve this goal, it is necessary to gain more insight into the manufacturing process of the support systems of wind energy converters and the factors that influence their service life. One of the most important of these factors is welding residual stress and its structural effects.

Residual stresses represent internal stresses that are present in a part or structure in the absence of any external loads or internal thermal gradient. In the particular case of welding, they are caused by non-uniform heating and cooling of the base/welding materials during the process. During

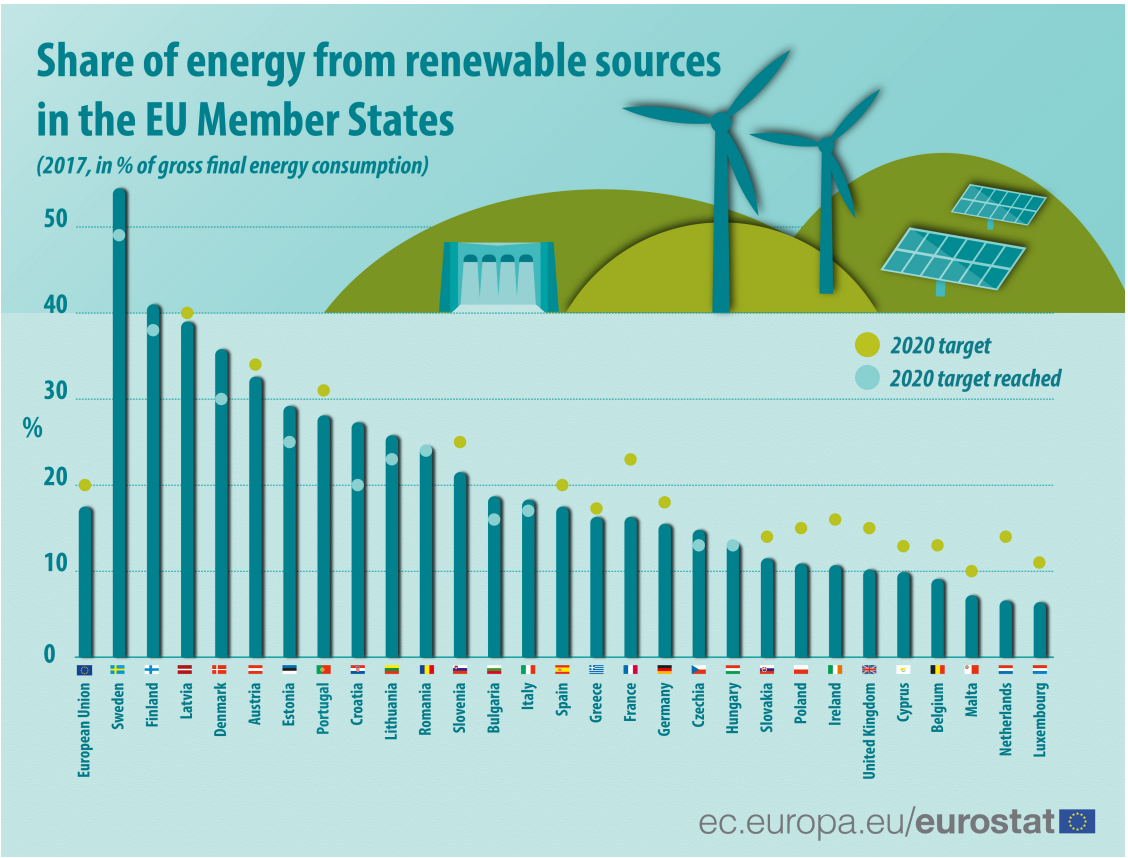



Figure 2.2: Primary production of energy from renewable sources, EU-28, 1990-2017

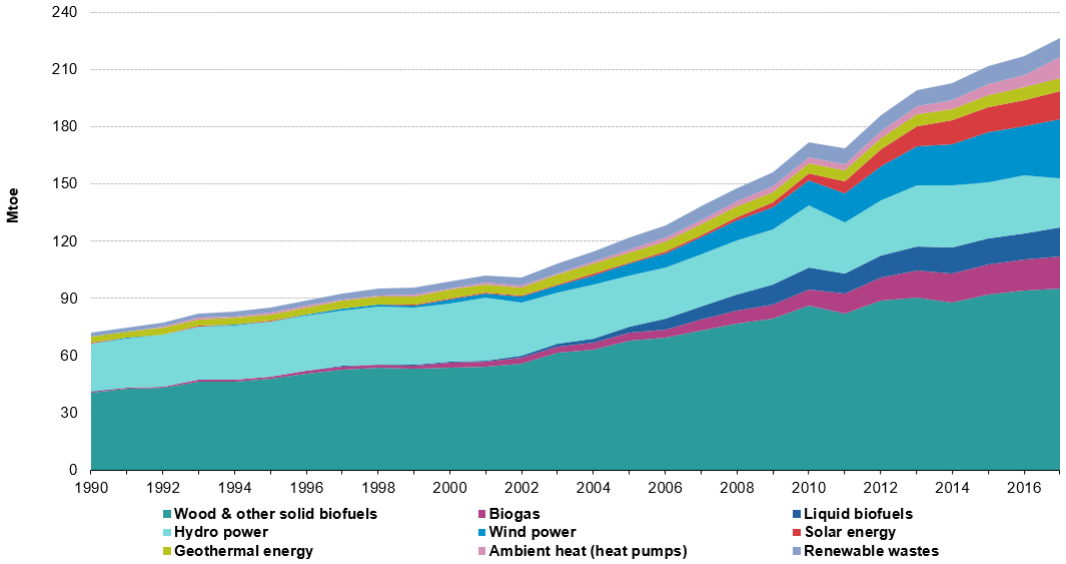



Figure 2.3: Primary production of energy from renewable sources EU-28 1990-2017

welding localized heating occurs in the part, which causes it to expand, but the surrounding colder area restricts this expansion. Because the metals yield strength is temperature dependent, the

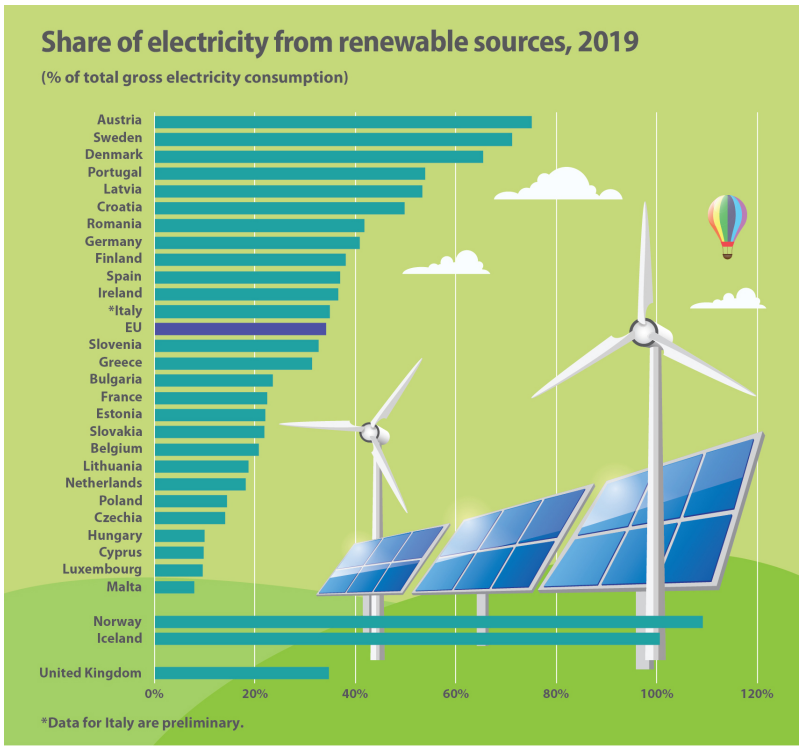



Figure 2.4: Share of electricity from renewable sources 2019

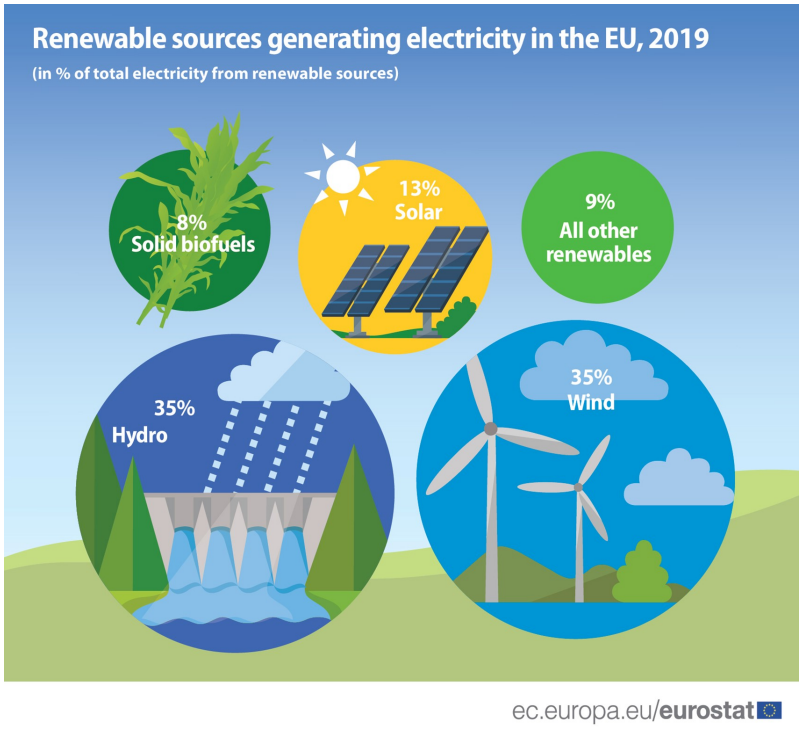



Figure 2.5: Renewable sources generating electricity in the EU 2019

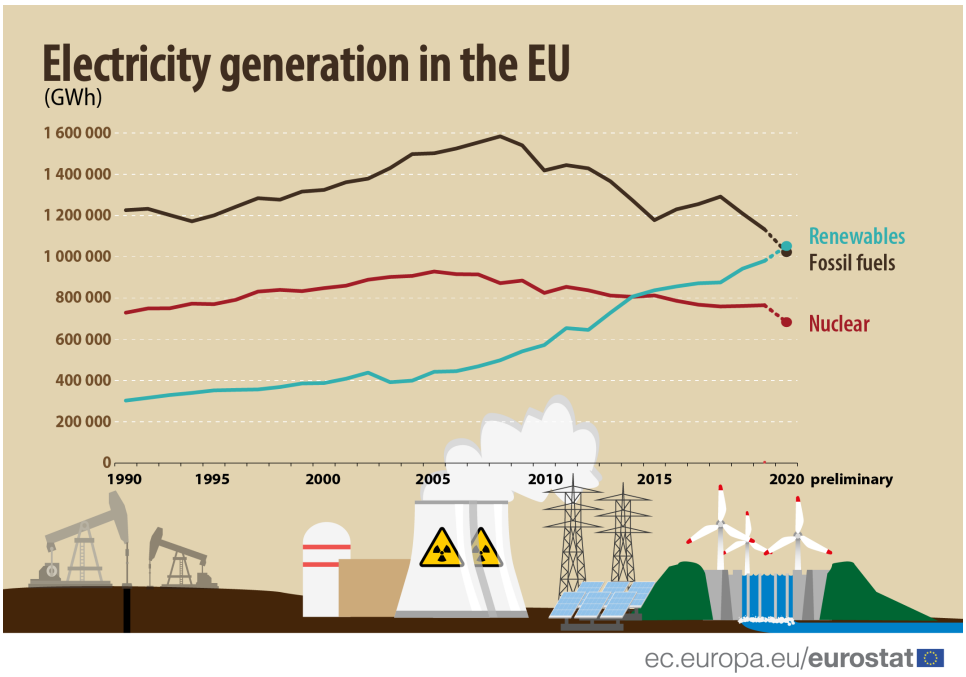



Figure 2.6: Electricity generation in the EU 1990-2020

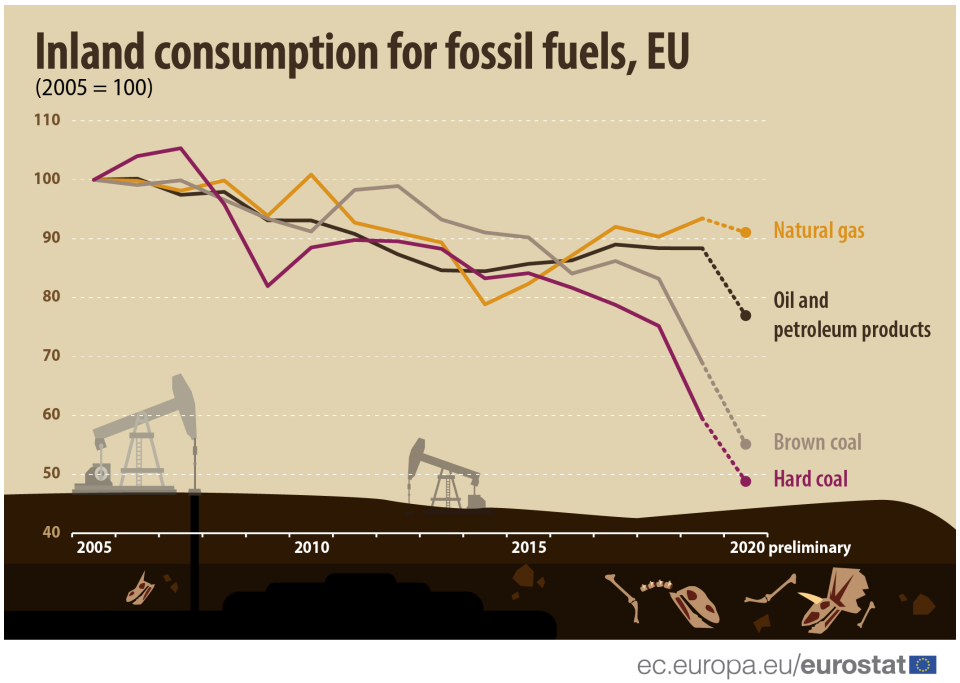



Figure 2.7: Inland consumption of fossil fuels 2005-2020

localized heating/cooling process gives rise to internal thermal stresses due to volumetric changes, which can lead to distortions, deformations, metal shrinkage, dimensional instability, change in microstructure, brittle fracture, and cold cracking, also aggravated by gas inclusions and other

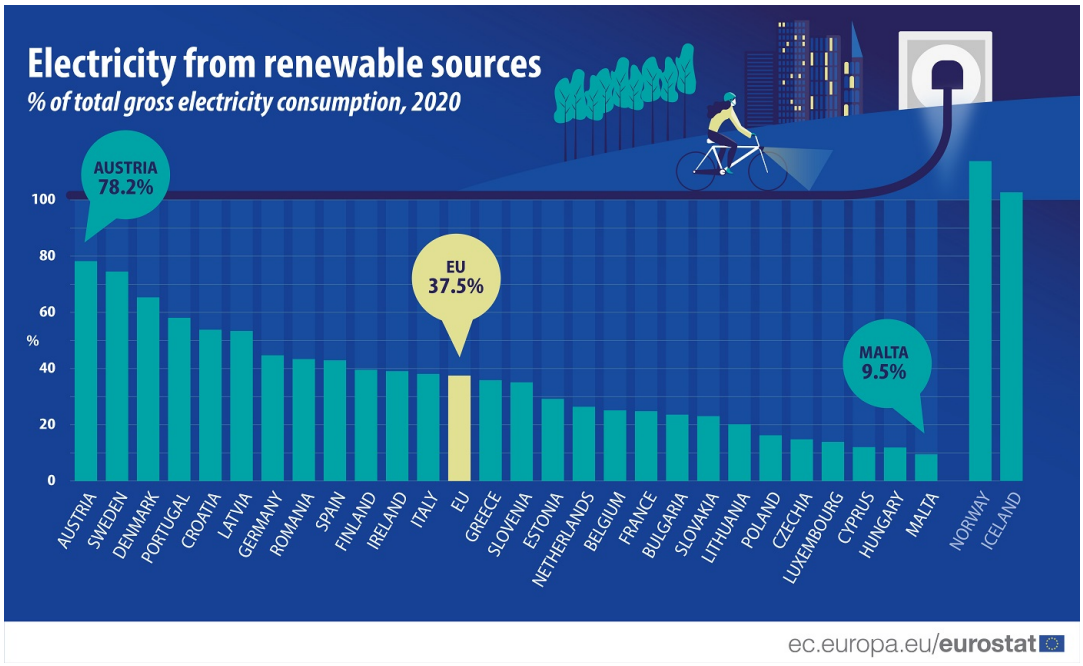



Figure 2.8: Electricity from renewable sources 2020

impurities. Tensile residual stresses are very detrimental to fatigue life and performance, as well as a major factor contributing to the degradation and failure of high-value engineering parts or structures even when subjected to loading at levels below the yield strength. The service life worsens even further when residual stresses are present in marine environments or in the presence of hydrogen sulfide. Because welding is one of the most used procedures for joining materials in many industrial areas ranging from the energy sector to aeronautics and transportation, the need for accurate measurement and prediction tools that assess the magnitude and distribution of residual stresses is of critical importance in order to assess and prescribe tools to improve the structural integrity of welded parts and structures [7–18].

Thus, it can be said that the demand for wind energy converters within the EU will increase in the future and a necessity for reducing the overall production and maintenance costs is highly desirable.

## 2.2 History of windmills

The harnessing of wind power stretches far into humanity‘s past beginning with early sailors and merchants using the wind to power their ships up rivers, lakes, and seas. Later it began being

used to power early windmills to mill grains or pump water. Some authors have suggested that evidence of ancient stone windmills has been found in Egypt which dates back to as far as 2000 BC, although there is no definitive proof that Egyptians, Phoenicians, Greeks, or Romans had any knowledge regarding windmills [19–22].

The word windmill in itself refers to a wind-powered machine that produces flour from grains via grinding or milling. Some of the first attestable windmills appeared in the Middle East; they had a vertical axis of rotation and were employed to assist in the milling of grains. A few of these ancient examples that have survived to the present day are in the north-eastern area of modern-day Iran, in the small village of Nashtifan. A few centuries later, news about Chinese windmills arrived in Europe, and just like the Persian windmills, they had a vertical axis of rotation but were used for draining rice fields, this structure was composed of bamboo and used fabric sails. The first European horizontal axis windmills came around 1200 AD from the Duchy of Normandy, although there exists some other information regarding a post windmill existing in the province of Brabant. From these few isolated examples, windmills expanded through the rest of Europe at a fast pace and a large number of post windmills were already in use in 13th century Germany. Besides the post windmills, which are made entirely of wood, tower windmills began making their appearance a couple of centuries after. This type of windmill differs from the post type by the fact that the windwheel rests on a circular tower made of stone. It is believed that this type originated in the south of France and spread through the Mediterranean world from which it took its name. The next step in the development of windmills came from the Netherlands in the 16th century, the main difference was the fact that the millhouse was fixed and only the tower cap could turn with the windwheel, thus harnessing to a fuller extent the power of the wind. This leap in development permitted the increase in size and range of applications of windmills [19–21, 23, 24].

### 2.2.1 European windmills

#### 2.2.1.1 Post windmills

The most important part of these windmills is the post or trestle, from which it has taken its name. The trestle refers to a centrally placed post, braced by four diagonal bars, which extends vertically to the halfway point of the total height of the millhouse. There it meets the meal beam which supports the millstone and acts as a midpoint of the millhouse, with the upper level being called

the stone floor and the lower level the meal floor. The windwheel, consisting usually of four large sails is mounted in the upper part of the structure and is connected via the wind shaft to the mechanisms that spin the millstone. These mechanisms consist of a cogwheel that spins a vertical shaft through a smaller horizontal spindle gear, also called a wallower, which in turn works the millstone. The entire millhouse could be turned in the direction of the wind by moving the tail, which was connected to the back of the structure and extended almost to the ground level. A series of posts were placed concentrically around the millhouse and by employing a rope winch, the entire structure could be turned. The sails consisted of fabric in Central Europe while in Northwestern Europe wooden sails were used. The outer shape of the structure varied locally, and they were exclusively used for milling grains [20, 25–32].

#### 2.2.1.2 Hollow Post mill

Due to the necessity of reclaiming landmass, early 15th-century Dutch "engineers" made efforts to employ wind power for driving scoop wheels for pumping water. The existing post or trestle windmills of the time were unsuitable for this purpose. This necessity inspired a new way to use pre-existing technologies. Thus, the hollow post mill came into being. This type of windmill worked in a similar manner to the post windmill but differed in a major way; the structure that contains the scoop wheel drive needed to be stationary, so the design of the post windmill was modified to only permit the rotation of the top part, containing the windwheel, cogwheel, and wallower on a bearing. The power was transmitted via a hollow shaft to the scoop wheel drive through an extended wallower shaft. This windmill is known as "Kokermolen" or "Wimpolen" and was used mainly for draining, with milling and sawing being used after the draining was complete [20, 25–32].

#### 2.2.1.3 Tower windmill

The tower windmill refers to the type that was widespread in the Mediterranean regions and originally consisted of a fixed windwheel placed on a circular stone tower with six or twelve triangular cloth sails. Later versions of this type permitted to yaw the wind shaft to a limited number of positions by manual labor as to provide some orientation into the wind [20, 25–32].

#### 2.2.1.4 Dutch windmill

The main driving force behind developing a new type of windmill was the same as in the case of the hollow post windmill, the necessity to provide a stationary lower structure where machines and mechanisms can operate in better conditions. Therefore, it was only natural to build part of the structure firm on the ground and to only allow the rotation of the roof cap which contained the windwheel. This design change represented a cornerstone in the development of larger and more powerful windmills. With a larger structure, this type of windmill could accommodate a large array of machines. It was employed for driving scoop wheels, grain millstones, heavy pan grinders for dye milling, hammering machines, and wood saws.

In the 19th century, Dutch windmills became the most versatile and powerful type, with a large range of applications. The outer shape also suffered some modifications during this time, mainly in the sense of aerodynamic refinement, with Dutch windmills becoming the main type of windmill in use and being the most widespread. An example of the components of a Dutch windmill is shown in Figure 2.9 [20, 25–32].

Dutch windmill Components :

1. Brake
2. Cog wheel
3. Windshaft
4. Rail bearing
5. Wallower
6. Vertical shaft
7. Sack "take-off"
8. Spur wheel
9. Spindlegear
10. Spindle
11. Stone crane
12. Feed of grain
13. Stone floor
14. Millstones
15. Mealslide
16. Lift for millstones
17. Meal floor

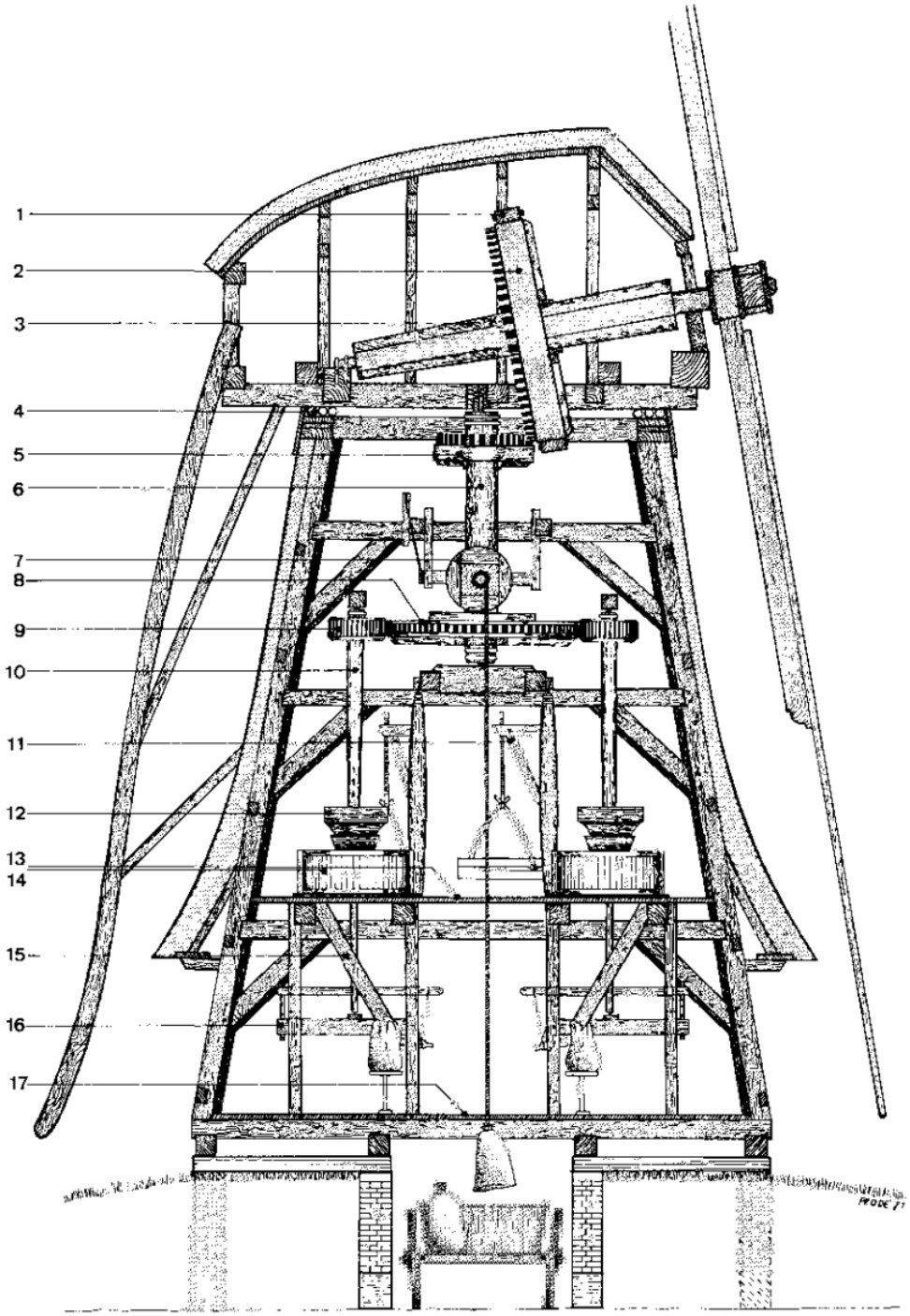



Figure 2.9: Dutch windmill cross-section [20].

#### 2.2.1.5 Paltrock mill

The Paltrock mill structure is similar to post windmills, where the entire millhouse rotates and is supported on a wooden or iron rim bearing that was laid on the ground or placed on a brick substructure. The millhouse rotates via rollers or small wheels. They were first built as wood sawmills as close as possible to the water to unload the logs directly from cargo boats. They were also used to mill grains but not as widespread as sawmills [20, 25–32].

### 2.2.2 Economic impact

Economically wise, European windmills provided a much-welcomed source of income for local rulers, with "mill laws" being in effect until the late 19th century. The local population of a certain area was only allowed to use a specific mill located in their area and furthermore, a mill construction ban kept their expansion in check. After the abolishment of mill laws late in the 1800s, coupled with a new freedom of trade approach, the construction of new windmills saw a sharp increase. In no other country did this boom have such a high impact as in the Netherlands, which apart from the milling of grains was using wind power to drain land masses reclaimed from the sea. Thus, it can be accurately said that the Netherlands could not have become an economical power without fully utilizing the wind power available to them. During the 17th century, the Netherlands became a powerhouse of international trade and started using windmills for other industrial operations. They were used in the manufacturing of spices, dyes, oils, and most importantly sawed wood. It is estimated that around 1200 windmills were in use in the Zaan area, close to Amsterdam, in the year 1700. The important economic advantage provided by windmills continued to increase into the 19th century, with approximately 200 000 windmills operating in Europe of which approximately 10 000 in the Netherlands. The 19th century brought about the industrial revolution, with new ideas springing all across the European continent. Some of these ideas, such as the steam engine had an impact on industries, and thus on windmills, with numbers beginning to decrease. Even with the introduction of steam engines, windmills put up a stern fight, with new windmills being built up until the early 20th century. This points to the fact that even though wind energy was uncertain and unpredictable, this did not prove to be such a large impediment. The rapid decline of windmills began when rural areas started to gain access to the electric grid, which made them obsolete. Due to the labor-intensive milling, process and

high maintenance costs windmills started to be less and less practical. Around 1943 the number of windmills in the Netherlands decreased to a staggering 1400. In the current day and age, windmills are gaining in popularity and are becoming protected cultural heritage landmarks. The interest in restoring and preserving them is growing in part due to more access to government funding. The total number of windmills that are in a relatively good state of preservation today is around 1000 in the Netherlands, 400 in Germany and about 160 in Belgium [19–21, 23–32].

### 2.2.3 Technological developments

Advances in windmill technologies from the Middle Ages up until the 17th century were sporadic, with improvements resulting mostly from empirically gained knowledge. Some of the first studies on windmill technology came from Italian Renaissance artists, such as Leonardo da Vinci and Veranzo among others, which mostly contributed with idealistic machines that never achieved any practical importance. Only in the late 17th century and early 18th century did windmill technology start to become an interest of mathematically oriented research. The subject was approached in more detail by great minds such as Gottfried Wilhelm Leibniz, Daniel Bernoulli, and Leonhard Euler. Around the middle of the 18th century, Meikle and Lee came up with a system that permitted the automatic yawing of the Dutch windmill by implementing a fantail. Some 40 years later, Meikle invented the first attestable spring sails. They contained hinged shutters that were connected to an iron rod, which permitted the fast opening and closing. Later these shutters were fitted with steel springs. During these times, the Dutch windmill achieved its developmental and technological peak. Although these innovations became a mainstay in Great Britain, the spring sails had a lower aerodynamic efficiency than classic cloth sails. The next step in the development of windmill sails came in the 19th century with the extensive research of Charles Augustin de Coulomb and Danish professor Poul La Cour. However, around this time windmills were already becoming obsolete. Poul La Cour was a visionary in the sense that even though his research would not have any practical implications for windmills, it could be applied in a new way, namely to obtain electrical current by using wind power. In the latter parts of the 19th century, new materials began to be used in the construction of windmills, which until that point had been built mostly of wood. Cast iron was used for the windshaft, but it quickly became apparent that the

traditional oak would perform better because of its damping properties and higher fatigue capabilities. Some of the last developments in this dying technology came about when Albert Betz, which formulated the principles of wind energy conversion, in cooperation with Major Kurt Bilau developed the "Ventikanten" sail. This new sail had adjustable flaps, which permitted some speed and power regulation. By the 1940s, they had equipped around 130 windmills with these new sails and obtained a high increase in the power output [19–21, 23, 24, 30–32].

### 2.2.4 Wind turbines in The New World

By the early 19th century, windmill technology was brought to the Americas, specifically on the East Coast of the United States, in the British and Dutch settlements. When the movements to the West started, early settlers needed to pump water due to the lack of surface water. However, the large European windmills were too heavy and large as well as difficult to assemble, so consequently, they became smaller and lighter. The downside was that the cloth sails were difficult to reef every time the wind was too strong and became a problem. The solution came from Daniel Halladay, a mechanic from Connecticut who, inspired by steam engine safety valves came up with a new design that permitted some sort of self-regulation of the windwheel blades. He also added a larger number of wooden blades, until the whole surface of the windwheel was covered. He managed to build and sell a large number of these windmills to Railroad companies. Another step in the development of American windmills came from Reverend Leonhard R. Wheeler, which added an extra wind vane that permitted to turn the entire windwheel out of the wind. This model was called the "Eclipse" and soon became the standard American wind turbine. The two windmill models were presented at the World Exhibition of 1876 in Philadelphia and saw great interest from farmers due to the simple and quite cheap design. Soon the number of windmills being manufactured increased, and many variants were developed. In 1930, around 100 companies were producing and selling windmills, with around six million being produced by then. However, once the electrification of rural American took place their numbers began to decrease, with around 150 000 units still being in existence in the USA today [19–21, 23–32].

### 2.2.5 Wind powered electrical generators

The generation of electrical power from wind was probably first attempted in rural America by inventive farmers that re-purposed the water pumping windmills into electrical generators. This happened in a period when the electrical grid was not large enough to reach these more remote parts of the country. However, the stepping-stone toward modern wind turbines was set by a Danish professor by the name of Poul La Cour in the city of Askov, Denmark. In 1891, with support from the government, he built an experimental wind turbine and testing station that was used to drive a "dynamo" and followed the traditional design of a European windmill. An astonishing fact is that he recognized the need to store the generated energy and thus used the direct current to produce hydrogen via electrolysis and stored it. The success of Poul La Cour's concepts became more apparent when the Lykkengard Company began building electricity-generating wind turbines modeled on the Askov test station. Following his early success, in collaboration with the Lykkengard Company, La Cour had constructed, by 1918, around 120 operational wind turbines that were powering rural areas of Denmark. Their turbines had various sizes with an output range of 10-35 kW and a rotor of approximately 20 m. The rotor had four shutter sails and yawing was performed by two fantails. The electrical generator was driven by a long shaft and intermediary gearbox and was placed at the base of a lattice tower. The interest in wind-powered energy generators began to decrease following the end of World War I, in part due to the price of Diesel fuel, which was inexpensive at the time. The situation reverted again when World War II started and fuel prices soared, and formerly decommissioned wind turbines were brought back into use. With the end of World War II, fuel prices decreased again, and cheap oil began to be widely available. The environmental impact of fossil fuels was not yet fully understood and thus attempts at harnessing wind power for generating electricity were present but at a much smaller scale. The next step in the development of modern wind turbines was taken by the F.L. Smidth Company. They manufactured the Smidth "Aeromotor" wind turbines with a power output of around 50 kW at a wind speed of 11 m/s, with a rotor diameter of 17.5 m, which sat on a lattice or concrete tower. Other endeavors were undertaken, but the ones that deserve mentioning are the work of Albert Betz, Major Kurt Bilau, Palmer Cosslett Putnam, and Ulrich Hutter. Some projects were undertaken in England, France, Denmark, and Germany, that greatly expanded on the first attempts of Poul La Cour but nevertheless, they did not come to fruition because of the many issues regarding

low yields, technical issues, and poor organization. Although faced with many obstacles, wind-powered electrical generators could not compete economically with the low prices of fossil fuels. During the subsequent decades, more funding was allocated towards developing alternative energy sources by governments and companies alike, especially during the energy crisis of the 70s and thus the evolution of wind turbines accelerated. Large experimental wind turbine farms were built and tested in the 1970s and 1980s, which expanded on previously gained knowledge and led to the current modern-day horizontal axis wind turbines [20, 33–45].

## 2.3 Wind resources

"Wind results from the movement of air due to atmospheric pressure gradients. Wind flows from regions of higher pressure to regions of lower pressure. The larger the atmospheric pressure gradient, the higher the wind speed and thus, the greater the wind power that can be captured from the wind by means of wind energy-converting machinery." [19]

The current estimation of total solar power that the earth receives is approximately $1.8 \cdot 10^{11}$ MW, of which around 2% becomes wind energy and around 35% is dissipated. As such the approximate value for wind energy that can be used is $1.26 \cdot 10^{9}$ MW, which represents 20 times more than the current global energy consumption. This means that theoretically, wind energy could supply the entire energy demands of the world. The main advantage of wind energy is that it represents a free, plentiful, clean, and environmentally friendly energy source [19, 46–48].

The most important factors that govern the movement and generation of wind are:

- Uneven solar heating
- The Coriolis force
- Local geography

The uneven solar heating is a consequence of a few factors. The earth's elliptical rotation around the sun, with the surface being perpendicular at the equator and parallel at the poles, creates masses of low-density warmer air at the equator and high-density cold air at the poles that tend to displace each other, creating the meridional circulation. The axis of rotation is tilted at approx. 23.5 °, which gives rise to seasonal changes. The surface itself is topographically uneven and covered with different materials that have varying reflective and absorbing rates of solar radiation,

which leads to high-temperature differences at the same latitudes. The Coriolis effect is caused by the self-rotation of the earth, and it manifests as local directional changes in the atmosphere. It is dependent on latitude, with the highest values at the poles, and diminishes towards the equator and on wind speed, increasing proportionally with an increase in wind speed. The combined effect of uneven solar heating and the Coriolis force is the break-up of the meridional cell in three distinct cells in each hemisphere, each with its own circulation pattern. These cells are deflected by the Coriolis force and create corresponding wind flow patterns shown in Figure 2.10. The local geography affects the wind speeds, with natural geographical features and man-made structures interfering and creating obstructions, variations, or local increases in wind intensity. Higher wind speeds are observed where rough terrain is present and with height increases [19, 49]. A typical example is shown in Figures 2.11 and 2.13, where it can be seen that the roughness and altitude in the interior lead to increases in wind speeds and thus to a higher power density. Wind energy represents an important sector in which INEGI had a sizeable contribution, being involved in approximately 80% of the wind parks installed in Portugal as of 2020 [50].

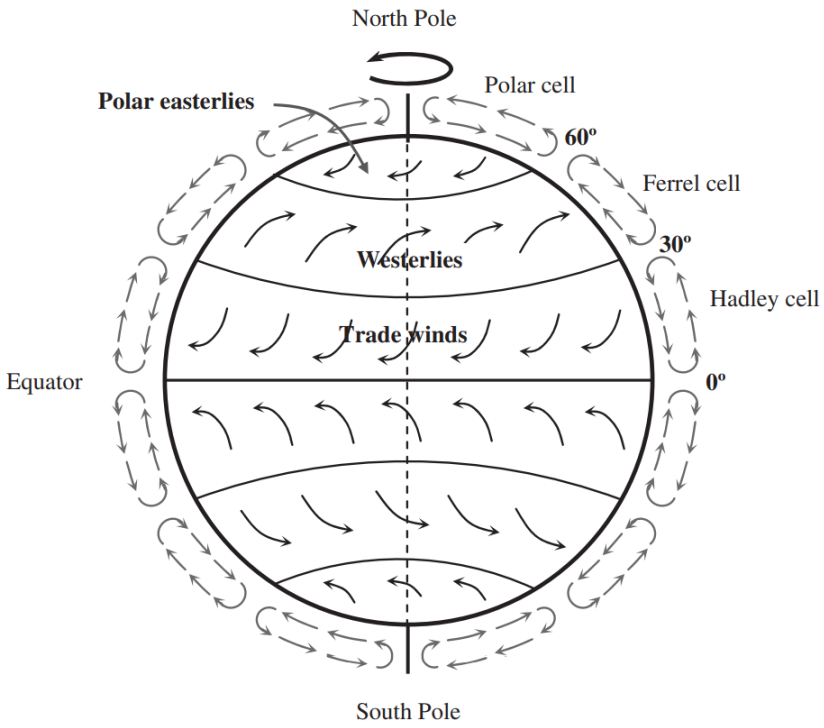



Figure 2.10: Idealized atmospheric circulations [19].

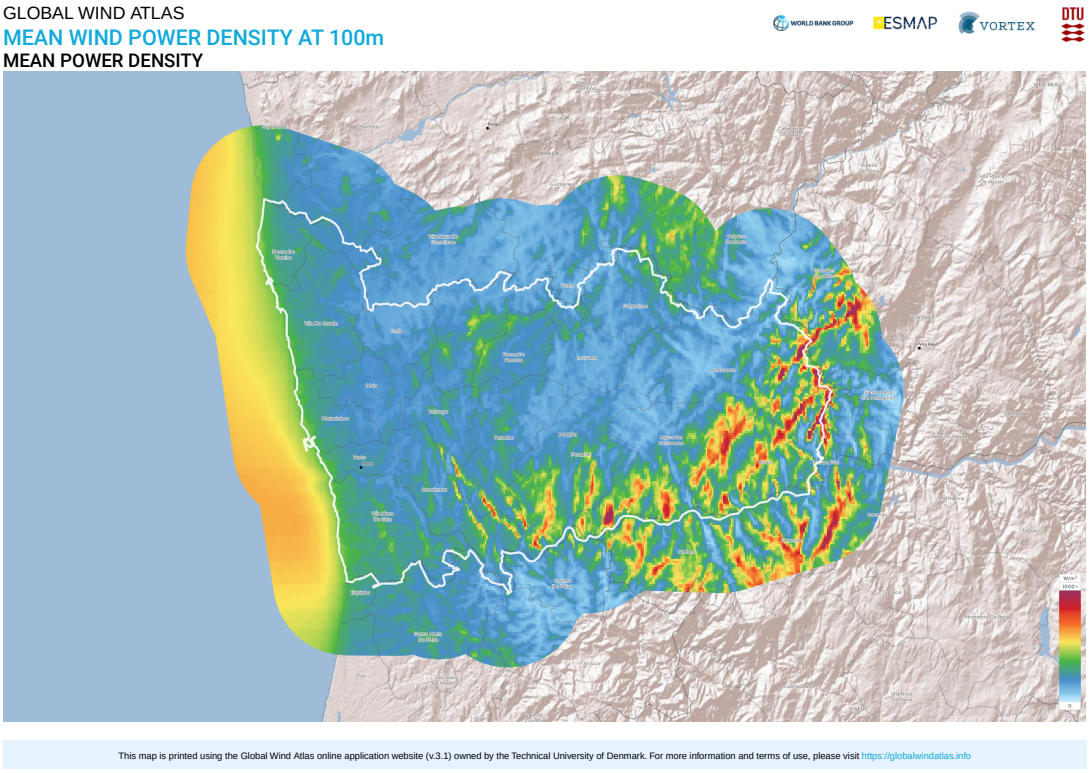



Figure 2.11: Local mean power density variation Porto area [51].

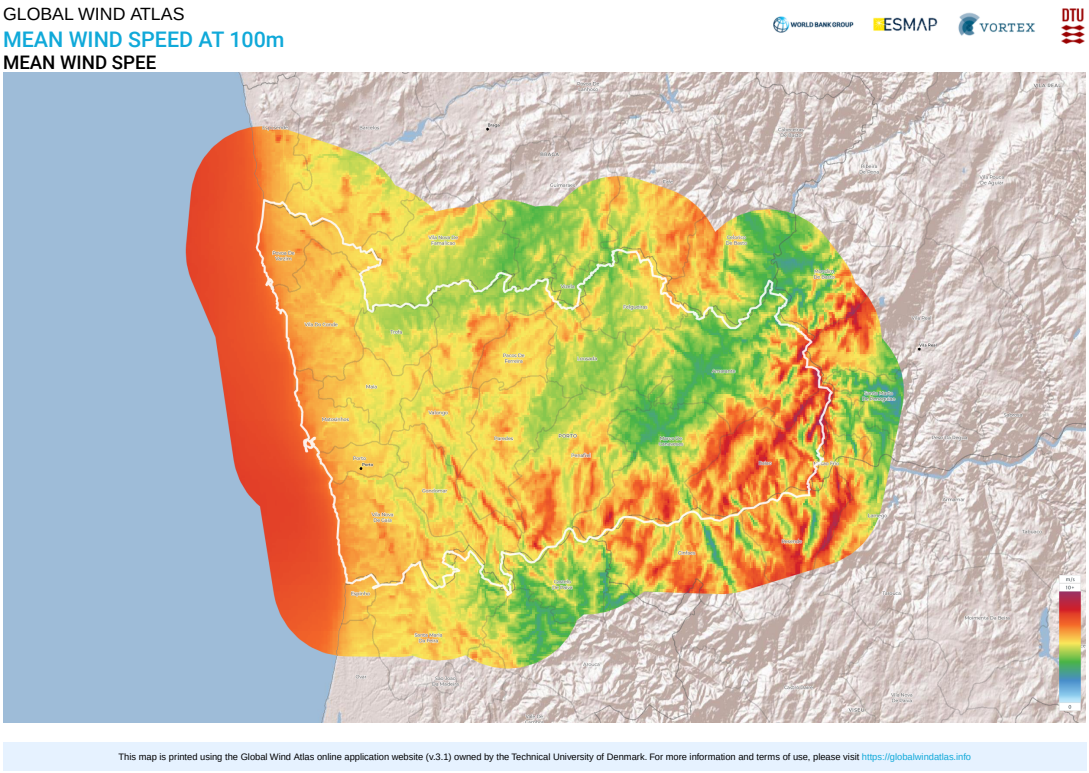



Figure 2.12: Local mean wind speed variation Porto area [51].

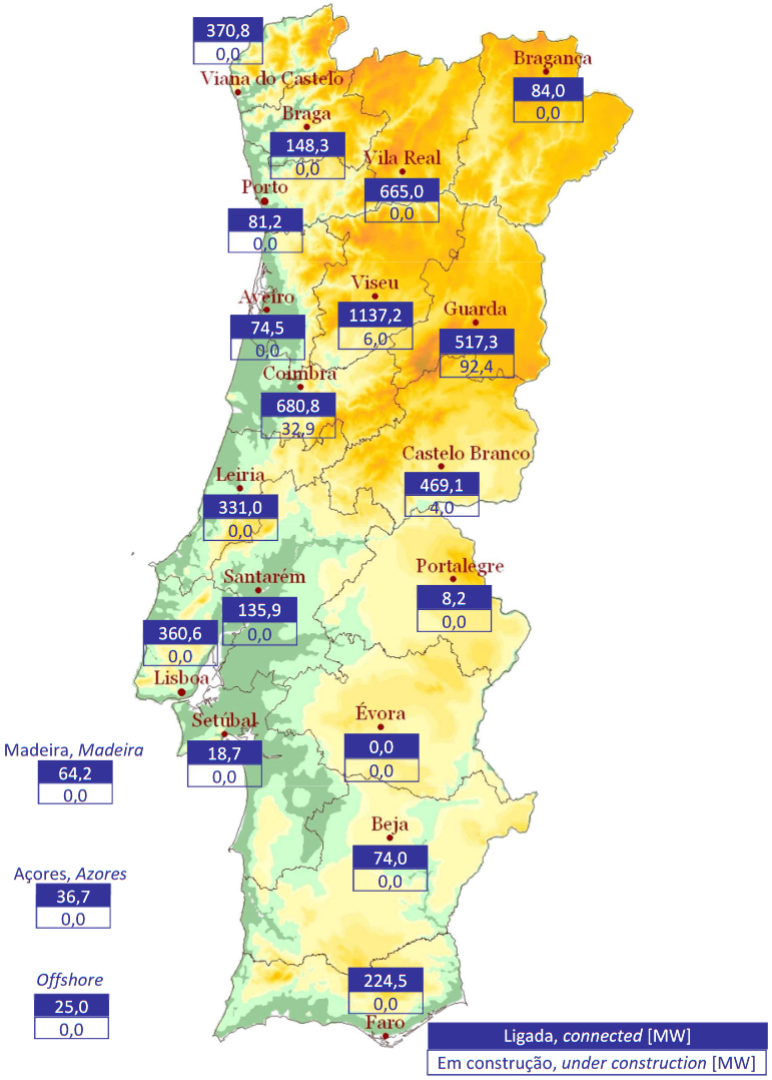



Figure 2.13: Installed capacity per district and autonomous region 2020 [50].

## 2.4 Horizontal axis wind turbines

Horizontal axis rotors are in use since antiquity, but the major developments toward modern wind turbines took place in the 19th century. During the 1980s, large experimental wind turbines were constructed by large industrial companies that took advantage of state subsidies or were part of state programs. Besides some experimental wind turbines that implemented vertical axis rotors, almost all high-yield wind turbines utilized this layout. The most common wind energy converters in use today are horizontal axis wind turbines, which convert the kinetic energy of wind into electrical energy by means of three large rotating blades. These turbines have the main rotor shaft and electrical generator at the top of a tower and most have a gearbox, converting the slower rotation of the blades into a quicker rotation that is more suitable to drive an electrical generator, an example is shown in Figure 2.14 and 2.15. Horizontal axis wind energy converters work on propeller-type concepts, wherein the rotor's axis of rotation is placed horizontally. The concept is the dominant one in use today mainly because the rotor speed and power output can be easily controlled by pitching the blades about their longitudinal axis, the blade shape allows for aerodynamic optimization and the technological advances in the development of propeller design. Together, these advantages account for the fact that virtually all modern wind turbines follow this approach.

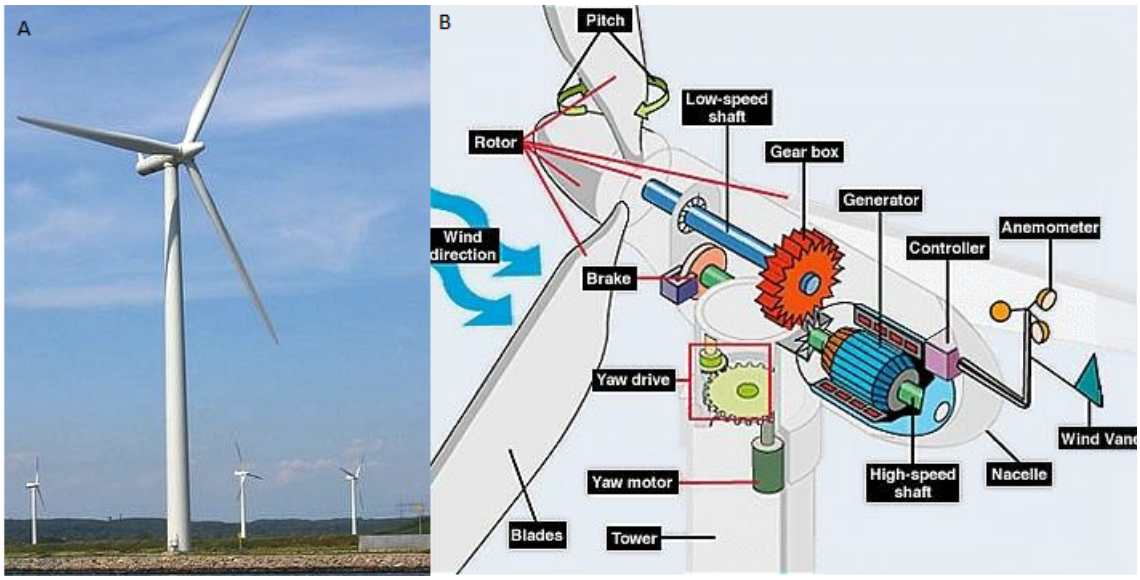



Figure 2.14: a.) Horizontal Axis Wind energy converter b.) schematic of the turbine blade assembly and nacelle [52].

Because this type of turbine produces the overwhelming majority of wind power in the world

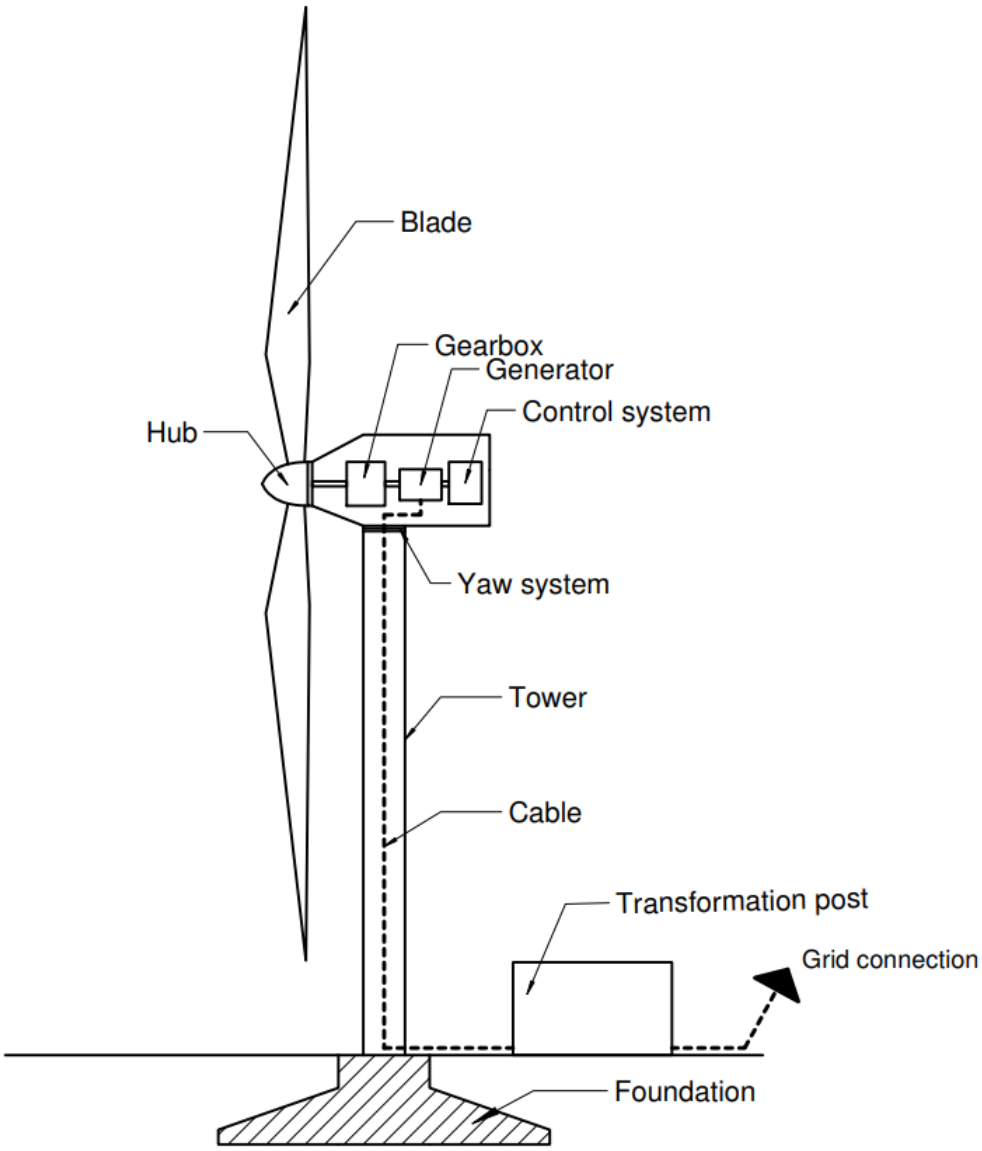



Figure 2.15: Wind turbine diagram.

today, demand has seen a steep increase in recent years. Driven by investments and innovation wind turbines have become more efficient than ever before. The maximum ideal efficiency of wind energy converters is given by Betz's Law which gives the maximum energy which can be extracted from air passing through the effective disk area of a wind turbine as 59.26% (16/27) [40]. Due to friction, drag, and other inefficiencies, only part of this kinetic energy is being harvested now. Other important variables for wind turbine efficiency are the wind factor capacity, which represents the energy produced by a turbine relative to its total energy potential, wind speed, air density, and temperature, with the ideal location and orientation for wind farms being as close

as possible to seashore line; eventually offshore. Turbines that reach higher altitudes can take advantage of the constant wind speed and an increase in the size of the tower means that the blades can be larger, thus increasing the total area of the disk, in turn increasing energy production. One predominant method of increasing efficiency has been to increase the turbine rotor size, either by retrofitting current turbines with larger blades or by designing taller towers, which allow a larger rotor to be fitted. As a direct result of the need for taller towers, designers started using lighter and stiffer materials in the manufacturing processes. Currently, the most common support system for wind turbines is a conical tubular steel tower. Because the tower represents 35-65% of the total weight of the turbine, it accounts for a large percentage of the transportation costs; thus, by using lighter materials in the tower, the transport and construction cost of the turbine can be reduced. One way designers dealt with the need for taller towers is by increasing the diameter of the tubular towers, but this comes with a big downside, namely because an increase in diameter implies an increase in the amount of material used by a factor of at least four and is limited by transportation capabilities. By accompanying the large tower with a larger rotor, a higher level of efficiency can be reached and justifying the higher production costs [19, 20, 22, 24, 53–56].

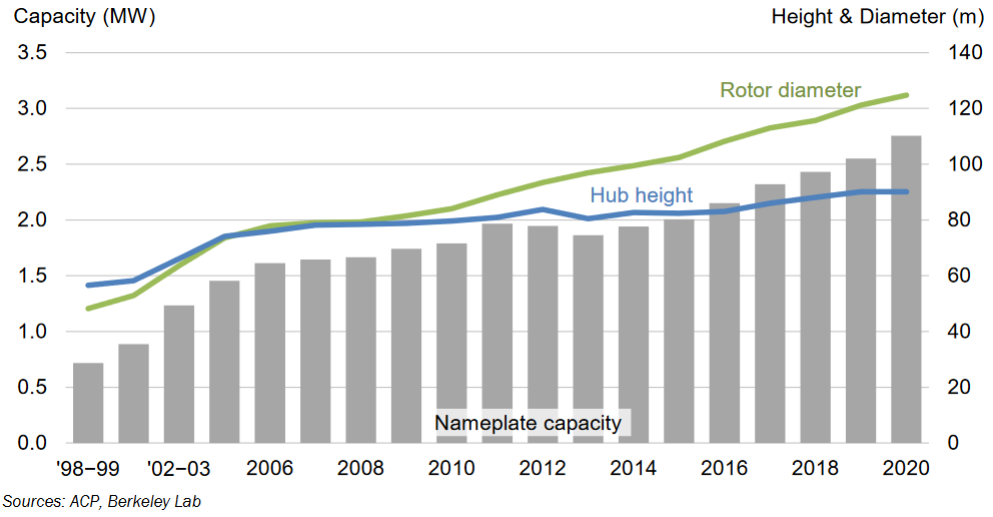



Figure 2.16: Average turbine nameplate capacity, hub height, and rotor diameter for land-based wind projects in the United States [57].

### 2.4.1 Betz's Elementary Momentum Theory

Betz's elementary momentum theory starts with the kinetic energy of an air mass (Equation 2.1) and uses it to describe the energy (Equation 2.2) which can be extracted from the airflow. The

power coefficient (Equation 2.3) is the ratio of extractable mechanical power to the power contained in the air stream and depends on the ratio of the air velocities before and after the converter (Figures 2.17 and 2.18) [20,40,41].

$$E = \frac{1}{2} \cdot m \cdot v^2 \qquad \text{(Nm)} \tag{2.1}$$

$E$ = kinetic energy

$m$ = air mass

$v$ = velocity

$$P = \frac{1}{2} \cdot \rho \cdot A \cdot v^3 \qquad \text{(W)} \tag{2.2}$$

$P$ = power

$\rho$ = air density

$A$ = swept area

$v$ = air velocity

$$C_p = \frac{P}{P_0} = \frac{1}{2}\left[1 - \left(\frac{v_2}{v_1}\right)^2\right]\left[1 + \frac{v_2}{v_1}\right] \qquad (-) \tag{2.3}$$

$C_p$ = power coefficient

$P$ = mechanical power output of the converter

$P_0$ = the power of the free-air stream flow without mechanical power being extracted

$v_1$ = air velocity before the converter

$v_2$ = air velocity after the converter

The maximum value of $C_p$ is obtained when the ratio $v_2/v_1 = 1/3$ and is known as the "Betz factor". An in depth explanation and analysis can be found in the literature [20].

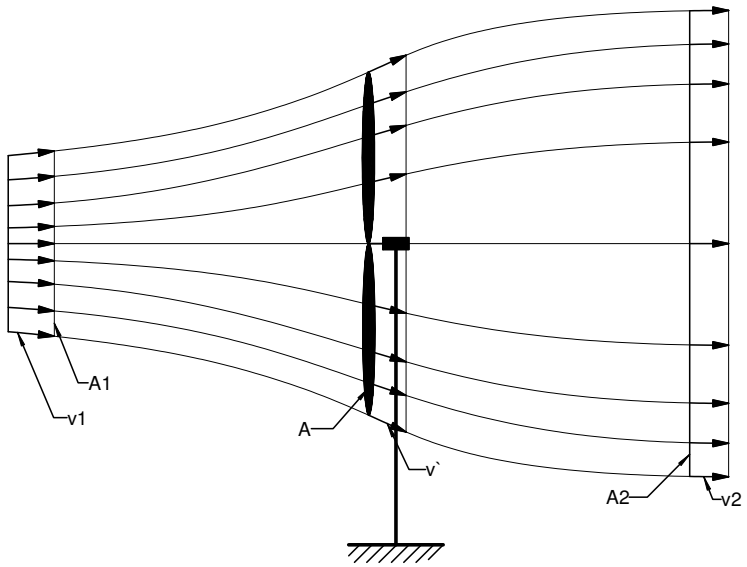



Figure 2.17: Flow conditions due to the extraction of mechanical energy from a free-stream air flow, according to the elementary momentum theory [20].

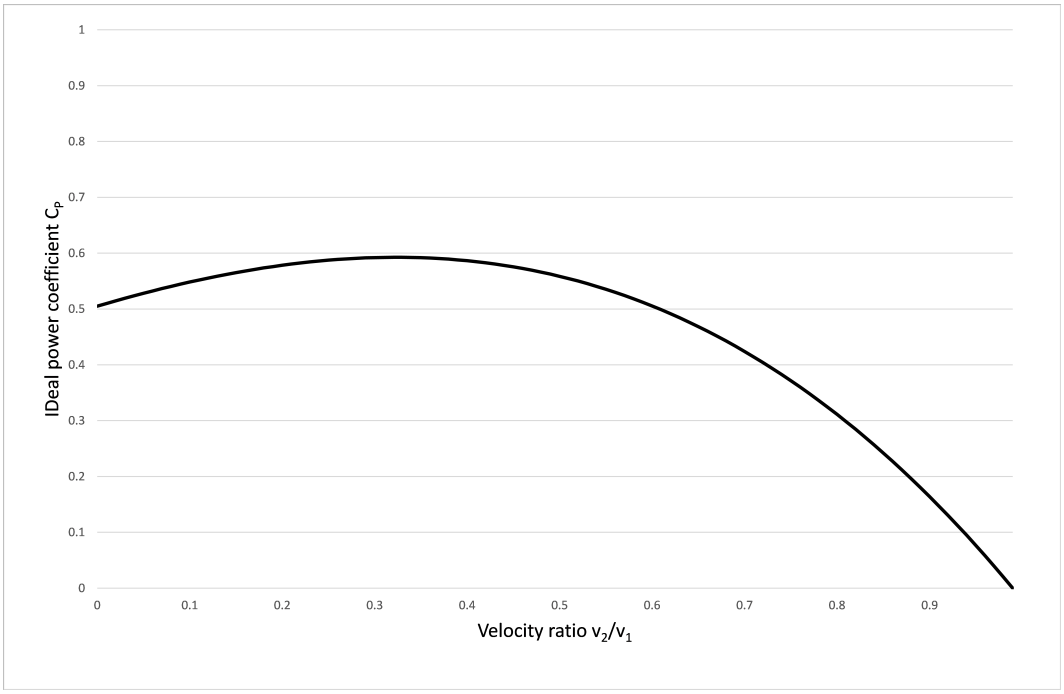



Figure 2.18: Ideal power coefficient based on $v_2/v_1 ratio$.

### 2.4.2 Wind turbine components

The main components in modern horizontal-axis wind turbines are:

- Rotor
- Nacelle
- Tower

**The rotor** refers to all rotating parts that are outside of the nacelle and comprises the rotor blades, rotor hub, and the blade pitch mechanism. The materials that were in use in the past for blade manufacturing were aluminum, titanium, steel, fiber composite materials, and wood. Most modern-day wind turbine blades are manufactured from fiber composites such as glass fiber, carbon fiber, or even Kevlar in certain cases. To manufacture the blades fiber mats are laid in layers inside a mold which is then subsequently impregnated with a resin and cured. In order to connect the blades to the rotor hub, different approaches can be undertaken. They can have a steel flange connection, cross-bolt connection, bonded-in flanges or sleeves, or bonded-in bolts. The rotor blades are also fitted with a lightning protection system, which consists of a metallic receptor placed at the tip of the blade and a conductor that connects them to the earthing system of the wind turbine. Besides the lightning protection system, the blades also require an ice warning or de-icing system in certain locations, which ensures that in the case of ice depositions on the blades it can trigger a warning that will stop the turbine or in the case of the de-icing system melt the ice deposits. **The nacelle** encompasses the mechanical drive train, electrical system, tower head bearings, and the yawing system. Although arranging the drive train in the nacelle has disadvantages, this is currently the standard design. **The tower** is the support structure for the nacelle and rotor and represents an essential part of wind turbines. The tower dictates the specific energy yield of wind turbines, which increases with height. It also represents roughly 30 % of the total costs. Usually as the height increase, costs of manufacturing, erection, and servicing increase accordingly. Besides its height, another important factor is its stiffness, which dictates the material required and consequently the construction costs. Besides the main components wind turbines also have auxiliary systems for control and measurement purposes and electrical connections to the main grid [20–24, 58].

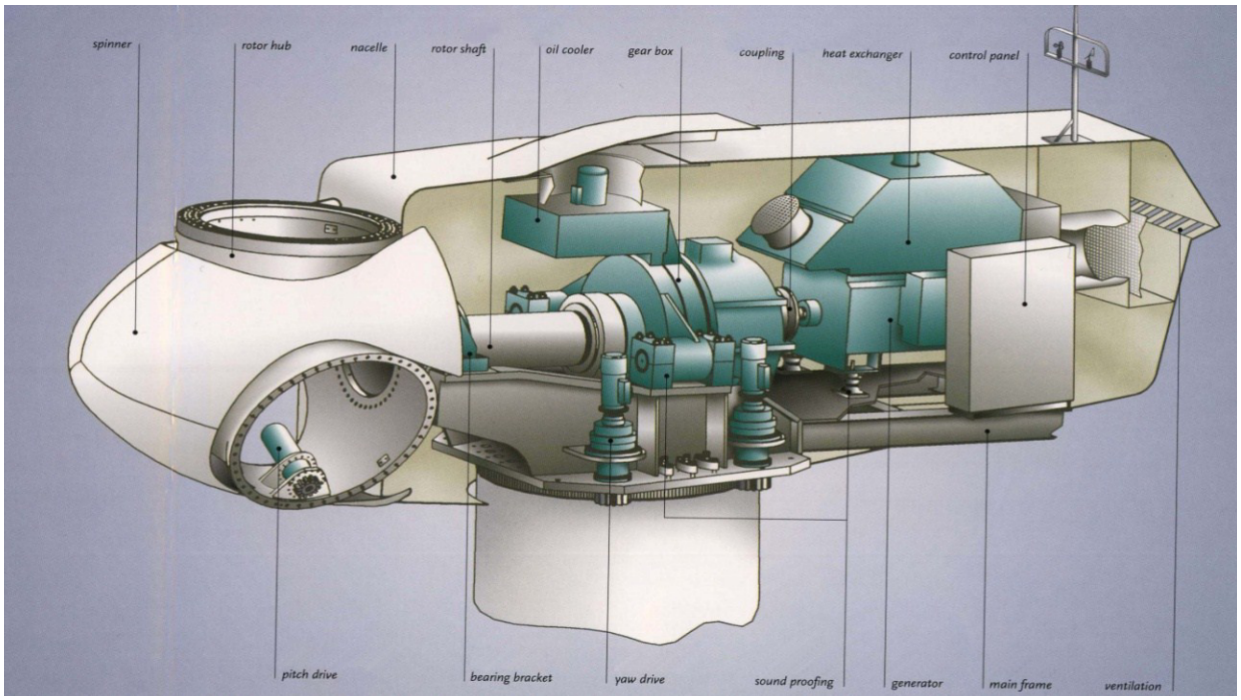



Figure 2.19: Nacelle layout GE Energy 1.x-100 wind turbine.

#### 2.4.2.1 Loads

Wind turbines are subjected to loads and stresses that are unique. Although the worst loading scenario would be due to extreme weather conditions or seismic activity, the continually alternating loads that occur under normal wind conditions are just as concerning. Alternating loads present an extra dimension of difficulty due to fatigue. In order to transform wind power into electricity, there is a need for large surfaces due to the nature of air density. This in turn translates into larger blades and rotor area, which implies the need for large tower heights. Large structures tend to have an elastic behavior, and thus the alternating loads are problematic in the sense that they induce vibrations and resonances that produce high dynamic loading. Wind turbines must be designed taking into consideration these loading patterns. First, they must be able to withstand the extreme loads that can occur due to extreme weather conditions or seismic activity. Secondly, the wind turbine needs to have a long service life due to the high costs involved, and thus withstand complex fatigue conditions where the magnitude, frequency, and duration of the loads can rapidly change. Another important problem is determining when to group the loads into load cases. The main load types that act on wind turbines can be divided into three main groups, gravitational loads, inertial forces and aerodynamic loads [20].

### 2.4.3 Typical tower production cycle

The production cycle of the steel tubular towers that support the wind turbine starts with large steel plates of variable thickness, depending on the specifications of the tower design. These plates, shown in Figure 2.20, are then cut by means of large Computer Numerical Control (CNC) machines that give the shape of the future shells.

The tower is divided, usually, into three to seven sections depending on the client's specifications and the height of the tower, each section being composed of several shells that have flanges at the ends, as can be seen in Figure 2.21. After aligning them carefully for assembling, their end flanges will be bolted together, and the bottom flange connected to the foundation. For manufacturing each particular shell, the first necessary step after plasma and oxy-acetylene flame cutting is the preparation of the bevels, in conformity with internal welding specifications.

The shape of the bevels depends on the thickness of the steel sheet and on the type of weld that will be applied. It is very important that the surface of the bevels is properly ground and



Figure 2.20: Steel sheet, after being bevelled and before rolling. Courtesy of Tegopi.



Figure 2.21: A large tower section. Courtesy of Tegopi.

cleaned to expose the steel, remove the Iron oxides and ensure no impurities are present when the weld pool solidifies. Any impurities can compromise the structural integrity of the weld and require additional material removal and re-welding. In this case, there are two types of welds that can be applied, longitudinal, where the sheet is welded to itself to create the tubular shape, circular between two shells, and circular between shell and flange. The steel sheet, after being cut, is then cold rolled to meet its particular diameter and checked with gauges for its tolerance‘s conformity, shown in Figure 2.22. After rolling, tack welds are applied longitudinally to make sure the shape and diameter are kept at desired values. The next step is the longitudinal weld, which is performed by semi-automated submerged arc welding robots with operators controlling



Figure 2.22: Steel sheet being rolled and tack welded. Courtesy of Tegopi.



Figure 2.23: Shells after welding. Courtesy of Tegopi.

the process. The welds are performed using the submerged-arc welding procedure and are multi-pass type. After the longitudinal welds (Figure 2.23) are finished the weld seams are checked by quality control operators by means of ultra-sonic tests, visual inspection, and magnetic particle testing, with any defects being marked and mended before the shell moves to the next step of the production process.



Figure 2.24: Flanges. Courtesy of Tegopi.

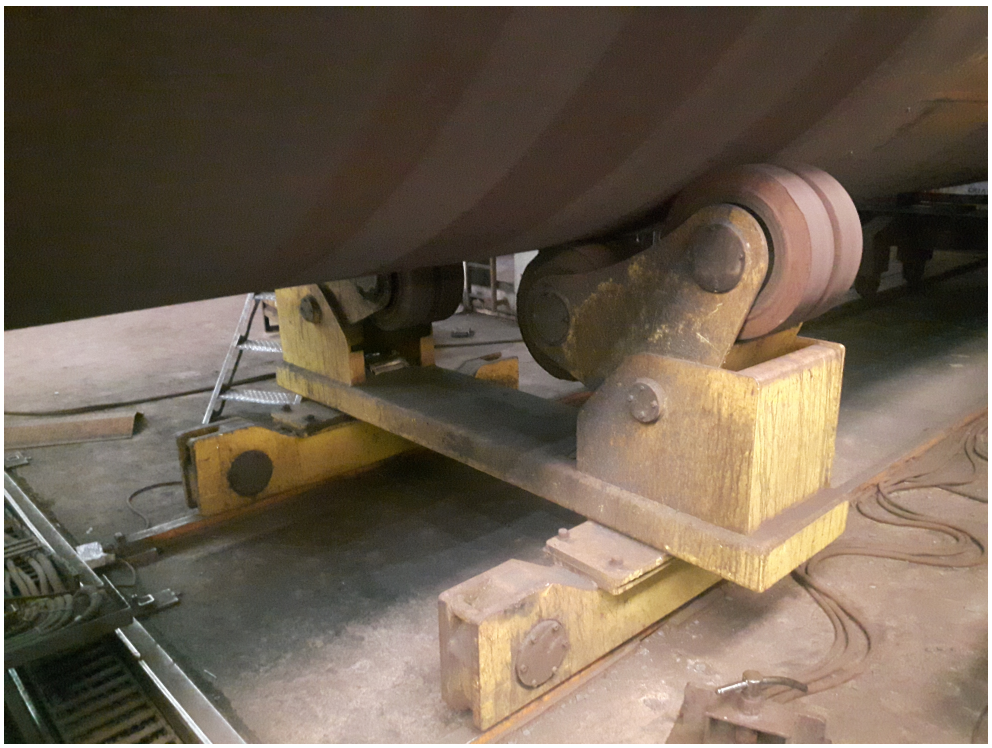


Figure 2.25: Shell on rollers. Courtesy of Tegopi.

The next step is to join the shells to each other and to the flanges (Figure 2.24). They are positioned on large roller beds and tack-welded together (Figures 2.25 - 2.26), afterwards the welding operators start performing the circular welds, and quality control check the integrity of said welds.




Figure 2.26: View from inside of a section (multiple shells being welded). Courtesy of Tegopi.



Figure 2.27: Completed section. Courtesy of Tegopi.




Figure 2.28: Motofil welding robot with Miller power sources. Courtesy of Tegopi.



Figure 2.29: ESAB welding robot (a), Miller controllers for Motofil robot (b), Motofil control panel (c). Courtesy of Tegopi.

Once the sections are finished, they will be sandblasted and painted, with the necessary equipment being internally mounted, e.g. floors, ladders, bolts, etc. With the sections being fully completed (Figure 2.27), they are ready for shipping to clients and ready for immediate erection on-site.

The welds are performed by several welding robots, some are older models produced by ESAB




Figure 2.30: ESAB controllers

which have been retrofitted, and others by Motofil and fitted with Miller Sumit Arc 1250 AC power sources and Miller SubArc 1250 DC power sources, controllers, and welding heads. The ESAB machines have a USB port in the back of the controllers for data back-up and transfer [59, 60], which offers the possibility of recording the parameters used during welding, while the Motofil/Miller machines have a USB port in the control panel. These are shown in Figures 2.28, 2.29 and 2.30. The welding speed for longitudinal welds is controlled by the welding operator by means of the controller, and for the circular weld by the rolling beds, which have a constant speed, but it can be modified between welding passes.

## 2.5 Submerged-arc welding

Welding techniques can be traced back to prehistoric times, but due to the fact that the only available heat sources were wood and coal, only low-temperature processes such as soldering or forging could be employed. What came to be known as welding only started being properly understood and developed in the second half of the 19th century. During World War II, shipbuilders started using welding instead of riveting on a large scale. However, out of the almost 5000 merchant vessels built in the USA during this time, approximately 1000 suffered structural failures. Although the process was well established at the time, not enough knowledge and practical experience were present in the design and manufacturing of large welded structures. These developments emerged when it became possible to generate a high enough electrical current and safely store oxygen

and acetylene in tanks. These together offered the possibility to generate enough heat to create a molten pool that solidified and thus creating a bond between parts [1, 2, 61, 62].

### 2.5.1 Origins and development

In 1936 Kennedy, Jones and Rodermund applied and obtained a US patent, registration number 2.043,960, covering electrical arc welding under a blanket of granulated welding flux, which completely submerged the welding zone, designated by Submerged-arc welding (SAW). The first applications used one wire and generally welding currents up to 1000 A. Soon after, refinements were made to the welding equipment and the welding current went up to 4000 A with thicker wires [2, 62].

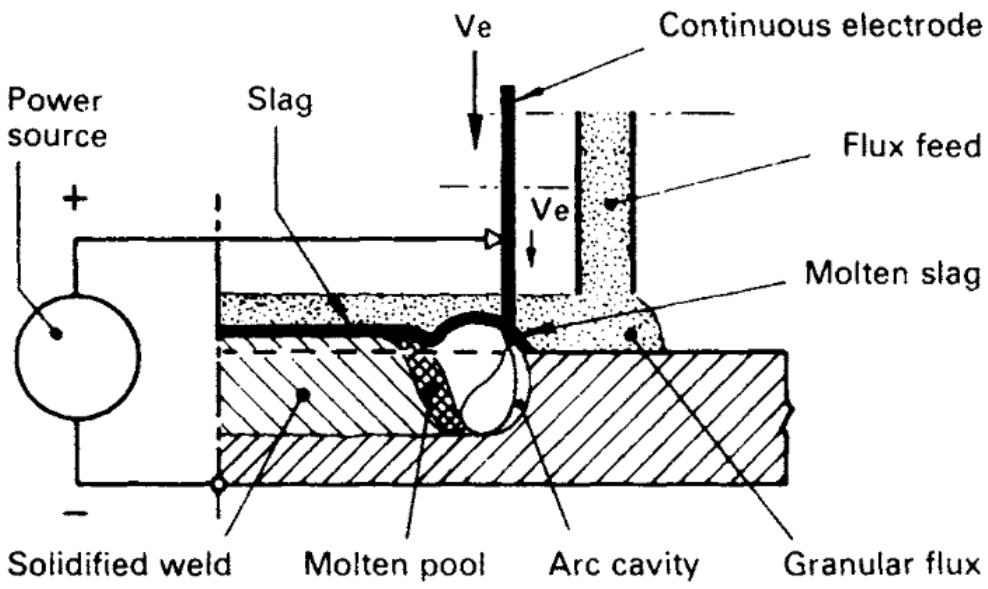



Figure 2.31: SAW Process diagram [62].

The deposition rates were around 55kg/h at the time, and new improvements started to appear, including series arcs, parallel welding, and multi-power, which became well-established methods. The configuration and properties of the electrode wire and flux had to change as requirements for the mechanical properties of the joints became more demanding and difficult to achieve. Because of the flexibility of the submerged arc welding process, variants with more than one wire started to be developed and used. Different electrical connections give different types of penetration beads and changes in the electrode stick-out were used to change burn-off rates. The applications of

SAW welding in different areas of the industry highlight the versatility of the process, from pipe welding, shipbuilding, bridge building, pressure vessel construction, rebuilding, and surfacing, to the motor industry and general fabrication [62–65].

### 2.5.2 The process

Welding is the most common and most important technique used for joining metallic parts. The core of the process is the melting of the areas that will be joined with or without filler materials while keeping the diffusion and dissipation of the heat to a minimum. The process of submerged arc welding is a well-known, high productivity, and widely used method of fusing metal parts together. The process consists of an electrical arc or arcs that are struck between wire electrodes and a workpiece that is covered with a layer of powdered flux. The arc is completely concealed by the blanket of flux, which removes the presence of smoke and fumes. Since the molten pool and arc are concealed, there is a need for devices that assist the positioning of the welding head with regard to the workpiece. The flux blanket provides protection from the atmosphere and allows for the addition of elements that help control the quality of the weld seam. The properties of the flux are dictated by the manufacturing method, which influences its properties and conditions of use. The final shape and contour of the weld beads are also influenced by the flux due to the fact that the molten slag rises to the surface and gives its shape, and well-made welds using this method are characterized by smooth contours. The electrode wires used usually contain alloys such as manganese or silicone that act together with the elements present in the flux to give an extra dimension of control to the properties and quality of the welds. Because the two are separate, the welding engineer has the possibility of varying the wire and flux combination in order to obtain desired outcomes, an option that is not possible in the case of manual metal arc welding. The wire diameters that can be used range from less than 1mm up to 6mm, which combined with the wide range of welding currents allow for workpieces with thicknesses from 3mm up to 100mm to be welded. The (SAW) process provides deep penetration, and high deposition rates, and is usually used for joining thick steel parts, although it can be used in automatic welding for thinner components. The equipment provides versatility since it can be stationary or mobile in relation to the workpiece. In summary, submerged-arc welding is applicable to a wide range of thicknesses and materials, since the arc and molten pool are covered by the blanket of flux, the radiation,

smoke, and fumes are kept to a minimum. Welding can take many forms and is a versatile and adaptable process. One of the few downsides is the fact that the welding must occur on a flat or near flat position vertically or horizontally. Submerged arc welding consistently provides the highest level of efficiency among the commonly used processes. Particularly because the arc is partly insulated from the surroundings, in the sense of heat radiation, by a blanket of flux powder and slag covering, although the slag is also itself a source of heat loss [1–3, 61, 62, 66].

The submerged-arc welding process can applied, but not limited to:

- Pipe welding
- Shipbuilding
- Bridge building
- Pressure vessel manufacturing
- Rebuilding and surfacing
- Automotive industry
- General fabrication

### 2.5.3 Principles

A power source, AC or DC is connected to the workpiece, as shown in Figure 2.32, the consumables consist of a continuous electrode and a granular flux, which is laid on the workpiece via a hose connected to a flux hopper. In order to prevent the electrode from overheating the current passes to the electrode close to the arcing point. The arc creates a gas-filled cavity in front of the arc and molten metal pool, which is covered by molten slag. Behind the molten pool, the weld solidifies and a thin layer of solid slag is present on top of it, which requires removal after cooling. Due to the cover provided by the flux, there is no radiation like Manual Metal Arc (MMA) and Metal Inert Gas (MIG) welding and almost no smoke generation. The flux is partially consumed and the unfused part is automatically recovered and reused. The ratio of wire to flux weight is usually equal but can vary depending on flux type and welding parameters. The equipment used in the submerged arc welding process consists of wired feeders and power sources, control boxes, flux hopper, welding head, and accessories. The accessories are usually comprised of a wire straightener, a flux recovery unit, and cross sliders among others. To increase production rates and minimize costs, the type of weld and corresponding joint preparation must be carefully

chosen. The joint preparation depends largely on plate thickness, type of joint and structural requirements. The next important step is choosing the appropriate welding conditions that affect the weld seam [1, 2, 62].

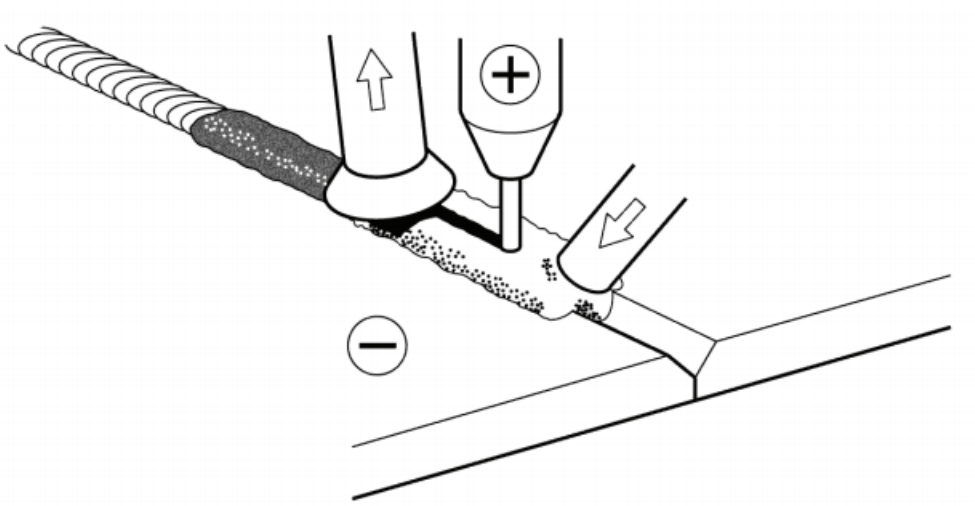


Figure 2.32: SAW principles [2].

### 2.5.4 Welding parameters

#### 2.5.4.1 Electrode polarity

Positive polarity provides the best surface appearance, deep penetration, good bead shape, and high resistance to porosity, while a negative polarity has lower penetration and higher burn-off rates because the maximum heat develops at the tip of the electrode instead of the work-piece surface. When changing from Direct Current Electrode Positive (DCEP) to Direct Current Electrode Negative (DCEN) it is necessary to increase the arc voltage in order to obtain similar results as with DCEP. Alternating current requires arc voltage somewhere between DCEP and DCEN. Usually, both AC and DC are used in tandem welding configurations with the leading electrode using DC and the trailing one using AC [1, 2, 62, 67–73].

#### 2.5.4.2 Welding current

The welding current influences the melting rate of the electrode, thus determining deposition rates. An increase in current produces higher deposition rates and vice versa, while also influencing the

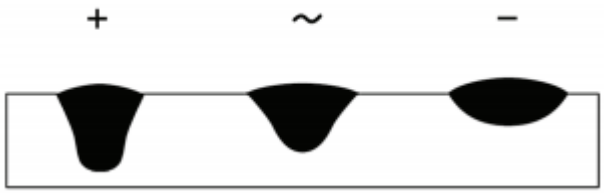



Figure 2.33: Electrode polarity effect [2].

depth of penetration. If the current is either too low or too high, it can lead to instability or undercutting. Welding current is determined based on wire diameter, plate thickness, type of joint, and desired deposition rate [1, 2, 62, 67–73].

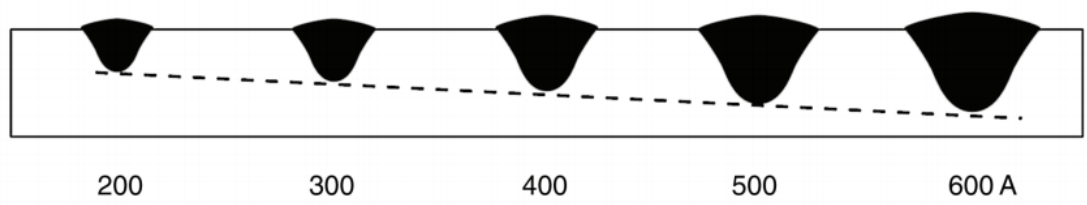



Figure 2.34: Welding current effect [2].

#### 2.5.4.3 Electrode diameter

The usually used wire diameter ranges between 1.0-6.0 mm. Wire diameters can be employed to obtain different outcomes, i.e. smaller diameters give deeper penetration while using the same current and a narrower weld bead. Smaller wire diameters also provide superior arc starting and stability. Thicker diameters in conjunction with a low current can easily bridge a wide joint [1, 2, 62, 67–73].

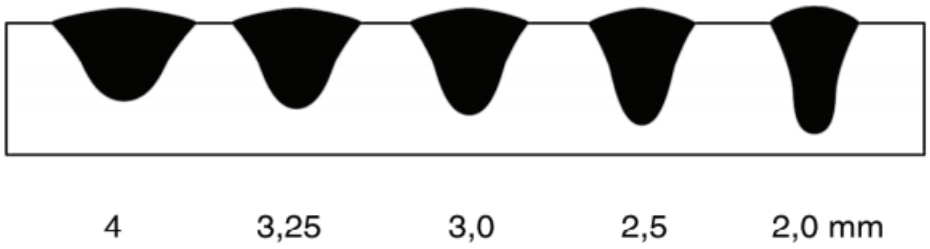



Figure 2.35: Electrode diameter effect [2].

#### 2.5.4.4 Arc voltage

Arc voltage has a large effect on the shape of the weld beads, with higher voltages resulting in wider and flatter weld beads. Arc voltage affects dilution rather than penetration and depending on the joint type the effect of arc voltage variations can have different outcomes. In a no-gap butt-weld configuration an increase in arc voltage produces wider and more diluted weld beads, while with a V beveled butt-weld configuration a high arc voltage can cause a lack of fusion. Moreover, when arc voltage is higher, flux consumption increases, and thus more alloying elements are present in the weld. Low arc voltage can result in a convex weld shape [1, 2, 62, 67–73].

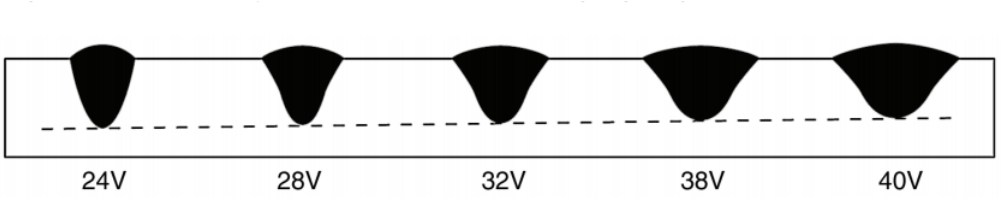



Figure 2.36: Arc voltage effect [2].

#### 2.5.4.5 Welding speed

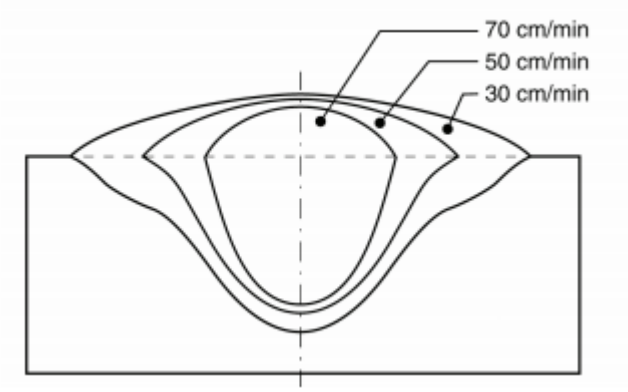



Figure 2.37: Welding speed effect [2].

The velocity of the electrode relative to the workpiece is called welding speed. For the same welding current, the width of the weld bead decreases at high speeds and increases with lower speeds. When a high welding speed is utilized, the result is a narrow weld with little penetration, and the likelihood of porosity, root defects, poor fusion, magnetic blow effect, undercutting, or irregular weld beads increases. On the other hand, if the speed is low burn-through can occur, and

if combined with high arc voltage it can lead to solidification cracks and a mushroom-shaped weld bead. Welding speed is usually limited by the welding current that can be tolerated by flux type, with special fluxes manufactured especially to allow high-speed operation. Higher speed can be achieved by using a twin wire configuration [1, 2, 62, 67–73].

#### 2.5.4.6 Stick out

Electrode extension has an effect on the resistance heating which happens in the electrode. When the extension is short, the heating is small and penetration is deep while increasing the extension leads to an increase in the temperature of the electrode, lower penetration but higher deposition rates. Regular extensions are around the 25-30 mm range [1, 2, 62, 67–73].

#### 2.5.4.7 Electrode angle

Because the angle between the workpiece and electrode influences the application point, it has a strong effect on shape, and penetration and can lead to undercutting [1, 2, 62, 67–73].

#### 2.5.4.8 Flux depth

Flux depth is not usually taken into consideration, although using too shallow flux can cause a rough surface or porosity and excessive flux cover can lead to worse bead appearance and dissatisfactory slag removal, or even spillage in the case of circumferential welds [1, 2, 62, 67–73].

### 2.5.5 Weld defects

Common defects, such as lack of fusion, slag inclusion, porosity, or uneven weld beads can be avoided by correctly utilizing corresponding weld procedures. When multiple runs are used special care must be taken to avoid narrow gaps between the weld beads in which slag might become trapped. Other defects, which are not related to the general welding conditions, can be avoided by maintaining the flux and wires in appropriate condition and careful preparation of the joint [2, 62].

#### 2.5.5.1 Porosity

Porosity is a common occurring defect, which can be influenced by a multitude of factors. It can manifest as pinholes or pores, easily visible on the surface of the weld bead, or under the surface, in

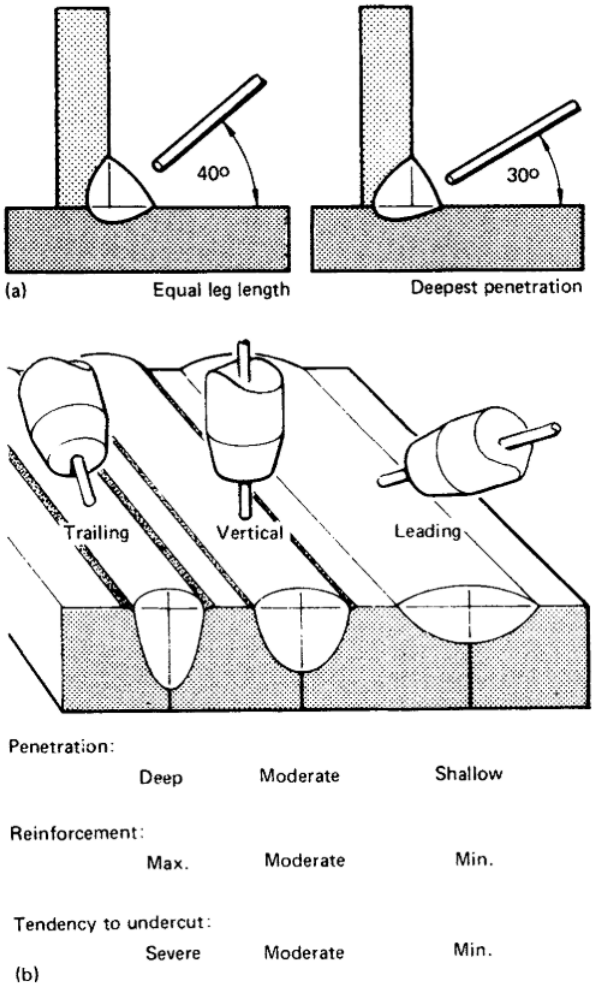



Figure 2.38: Electrode angle effect [62].

which case ultrasonic testing is required to reveal them. Porosity can be a result of contamination of the joint surface with oil, paint, grease, dirt, or moisture present in the flux. These defects can be avoided by thoroughly cleaning the surfaces before welding and by ensuring the flux is dry and kept in a warm environment [2, 62].

#### 2.5.5.2 Hydrogen-induced cracking

Hydrogen cracking or cold cracking usually occurs in the heat-affected zone during the cooling phase, in some cases even hours after the initial welding. The main causes are hydrogen diffusion from the weld metal, martensite phase formation, and shrinkage stresses. The presence of moisture in the flux can result in hydrogen cracking, thus the flux should always be kept in a dry

environment. According to welding procedures high carbon content steels (>0.40) and large thicknesses require welding at high temperatures or by preheating/post-heating the workpiece. Other important factors that influence hydrogen cracking are the use of a clean wire and avoiding a hardened Heat Affected Zone (HAZ) by utilizing minimum energy input. Although in SAW, hydrogen cracking is not as common as in the case of other welding techniques, such as MMA, when it does occur, the cracks can be detected by ultrasonic testing. In the 1970s this phenomenon, also known as "chevron cracking" was investigated and moist flux was identified as a defining factor [2, 62].

#### 2.5.5.3 Solidification cracking

Hot cracking, also called solidification cracking, occurs due to the high welding speeds and relatively large weld pools that result from the SAW process. They are located along the center-line of the weld beads and are usually the result of narrow deep welds or mushroom-shaped weld beads. The main factors that influence this defect are the chemical composition of the weld, the solidifying pattern, and the amount of strain. Higher than usual contents of phosphorus, carbon, or sulfur in the parent material can increase the risk of hot cracking and can be counteracted by utilizing a wire with higher manganese content and high silica fluxes. In order to prevent hot cracking, high welding speeds, large root gaps, and long deep weld pools should be avoided. In certain cases, a longitudinal groove can be seen on the surface of weld beads that is caused by shrinkage but is only superficial and can be confused with hot cracking [2, 62].

#### 2.5.5.4 Arc blow

Arc blow occurs due to magnetic forces that act around the arc and can cause arc deflection and defective welds. This phenomenon only occurs when using a DC power source. Even when the electrode is in the correct position, the arc may deflect and the weld pool will be deposited around it. To prevent this, the position of the earthing point is vital, while dual earthing points also can fix the issue [2, 62].

#### 2.5.5.5 Undercutting

Undercutting appears when the weld metal does not manage to fill the cavity. Undercutting defects can occur when the voltage range has been passed. When the voltage is too low, the result is

a convex and narrow weld bead, while increasing the voltage can produce undercutting at the edges of the weld beam. In addition, when using high weld speeds, the result can be a high convexity weld coupled with undercutting. This issue can be avoided by using a different wire angle position [2, 62].

#### 2.5.5.6 Slag inclusions

Slag inclusions are not encountered usually in SAW welding, but when they do occur, they tend to happen in between passes in a multi-pass weld. Extra care must be taken between the passes and all slag must be carefully removed [2, 62].

#### 2.5.5.7 Uneven weld beads

Uneven weld beads can be caused when using a high welding current (>1100 A) combined with small wire diameters. The main cause of this defect is the high arc pressure on the molten weld pool, which results in a too high penetration for the wire size, molten metal ejections over the edges, and also possible lack of fusion. This can be prevented by increasing the wire diameter [2, 62].

#### 2.5.5.8 Poor impact strength

Poor impact strength occurs when slow cooling is involved. The good penetration of SAW implies that even for thicker workpieces the best results are obtained by using as few passes as possible. However, due to the high heat input, it is preferable to use multiple passes to prevent this defect [2, 62].

## 2.6 Residual stress

"Residual stress is that which remains in a body that is stationary and at equilibrium with its surroundings. It can be very detrimental to the performance of a material or the life of a component. Alternatively, beneficial residual stresses can be introduced deliberately. Residual stresses are more difficult to predict than the in-service stresses on which they superimpose. For this reason, it is important to have reliable methods for the measurement of these stresses and to understand the

level of information they can provide. It can be detrimental when it reduces the tolerance of the material to an externally applied force, as is the case with welded joints" [7, 8].

Welding is the non-detachable joining or coating of components or base materials under the application of heat or pressure, with or without the use of filler material [74].

The area closest to the heat source is heated up quickly, while the surrounding area is relatively cooler. Due to the high thermal gradient, the material expands but the cooler area constricts this expansion giving rise to thermal residual stresses. In certain areas, the stresses exceed the yield limit, which is lowered at high temperatures, and results in tensile stress close to the weld bead and compressive stress further away from it. A typical example of longitudinal and transverse residual stress measurements in a rectangular plate with a single-sided centric jointing weld is shown in Figure 2.39 [1].

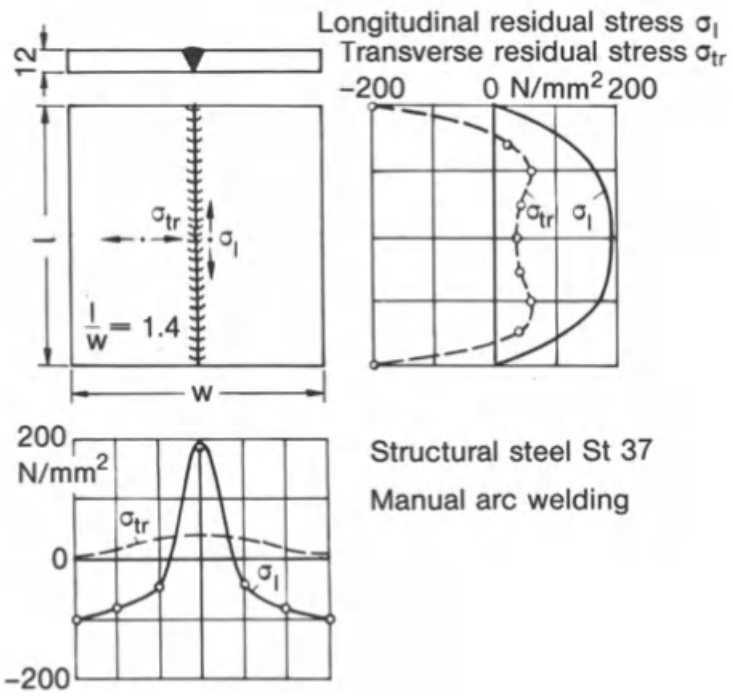



Figure 2.39: Longitudinal and transverse residual stresses in centre cross-sections of rectangular plate with centric weld [1, 75].

These stresses are the result of inhomogeneous permanent plastic deformations, which, at the material element, can be divided as follows:

- volumetric or "dilatoric" strains resulting from thermal expansion, chemical conversion, microstructural transformations or changes in state.
- distortional or "deviatoric" strains as a result of plastic and visco-plastic deformation.

and are shown in Figure 2.40.

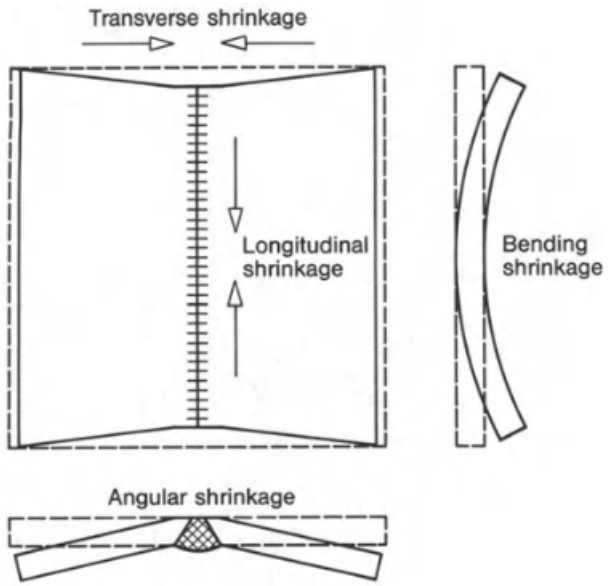



Figure 2.40: Longitudinal and transverse shrinkage, angular and bending shrinkage of rectangular plate with single- side welded centric jointing seam [1].

Depending on the scale on which they act, residual stresses can be divided as follows:

- First order ($\sigma^I$) or type I macrostresses, which act on macroscopic level.
- Second order ($\sigma^{II}$) or type II, which act at the intragranular level.
- Third order ($\sigma^{III}$) or type III, which act at the atomic level.

Most of the parameters that influence welding residual stress and welding deformations have a non-linear, transient, and temperature-dependent effect, which prevents one from making any type of generalization. In order to reduce the complexity of the phenomenon, a decoupling into the main parts is necessary, thermodynamic, mechanical, and microstructural processes, as shown in Figure 2.41 [1].

Welding residual stresses and distortions are originating from the localized high heat input over a relatively short period of time. When a moving heat source travels across the workpiece it produces differential temperature fields. Temperature fields during welding are transient and

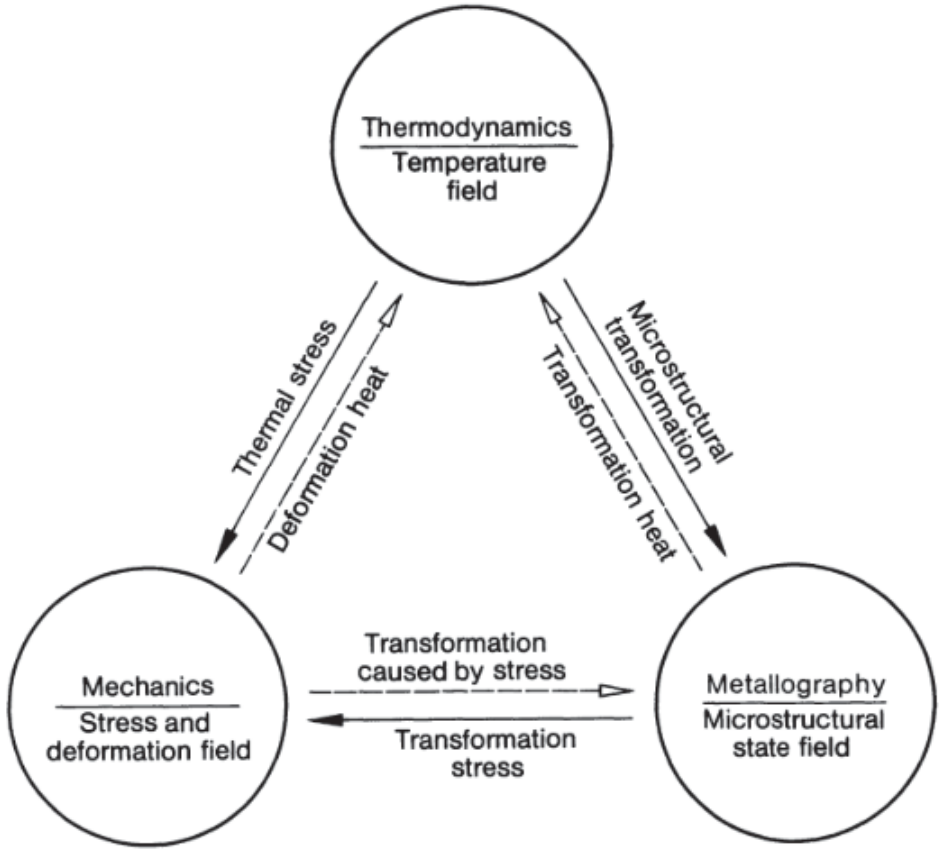



Figure 2.41: Decoupling and mutual influencing of temperature field, stress and deformation field and microstructural state field [1, 76]

very inhomogeneous because of the high thermal conductivity of carbon steels. They have a big influence on the stress state of the steel workpiece during and after welding. This is illustrated in Figures 2.42 - 2.44.

The heat input is the main factor that influences the properties of steel welds. It can be calculated as follows [78]:

$$Q = k \cdot \frac{U \cdot I}{v} \cdot 10^{-3} \qquad (\mathrm{kJ/mm}) \tag{2.4}$$

where:

$k$ = thermal efficiency (Table 2.1)

$U$ = arc voltage [V]

$I$ = welding current [A]

$v$ = travel speed [mm/s]

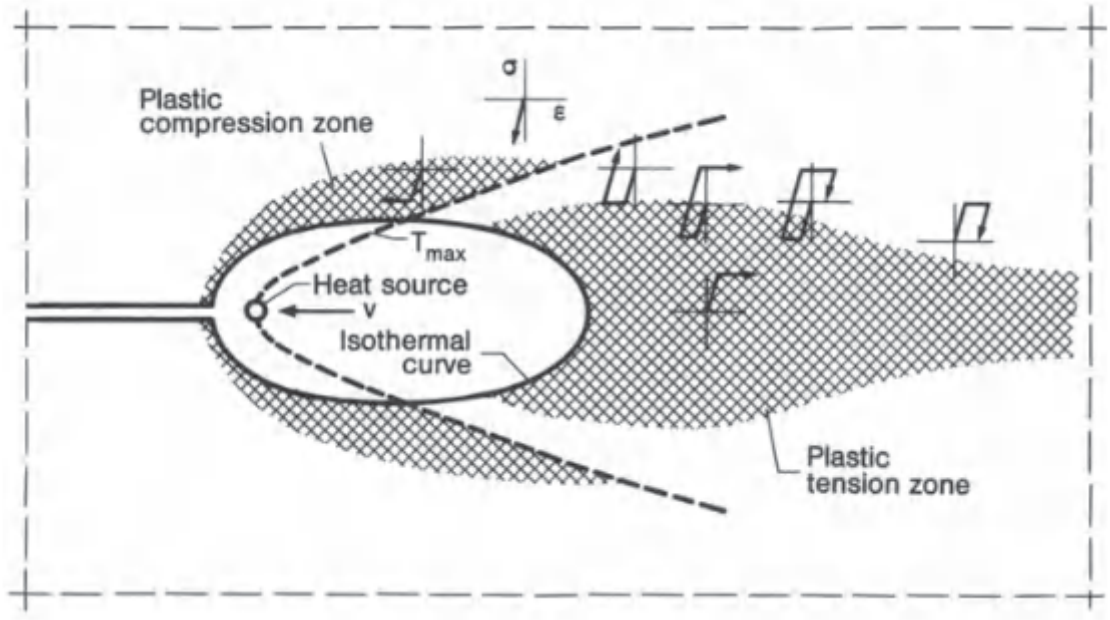



Figure 2.42: Plastic zone and local stress-strain cycles in quasi-stationary temperature field of moving heat source [1].

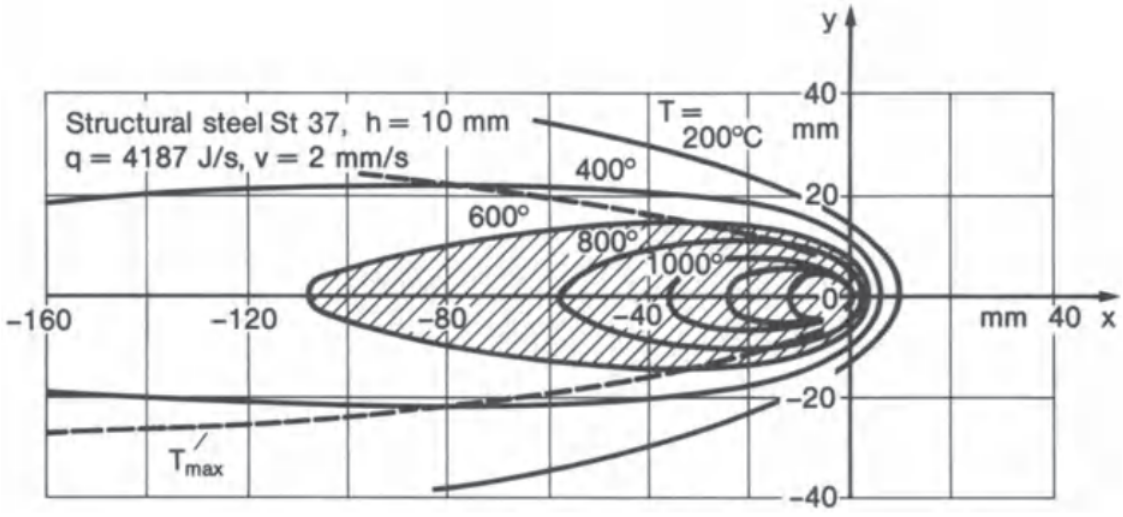



Figure 2.43: Example of temperature field isotherms around welding heat source moving uniformly and linearly in an infinite plate [1, 77].

Welding residual stress, simultaneously with other causes, can give rise to hot cracks, cold cracks, brittle fractures, and early instability, affect serviceability as a result of distortion or warpage, and impair manufacturing. Manufacturing processes that can cause residual stresses are welding, casting, hot or cold working, machining, coating, surface treatment, heat treatment, and age hardening. Usually, welding residual stresses occur in parts that have already been subjected

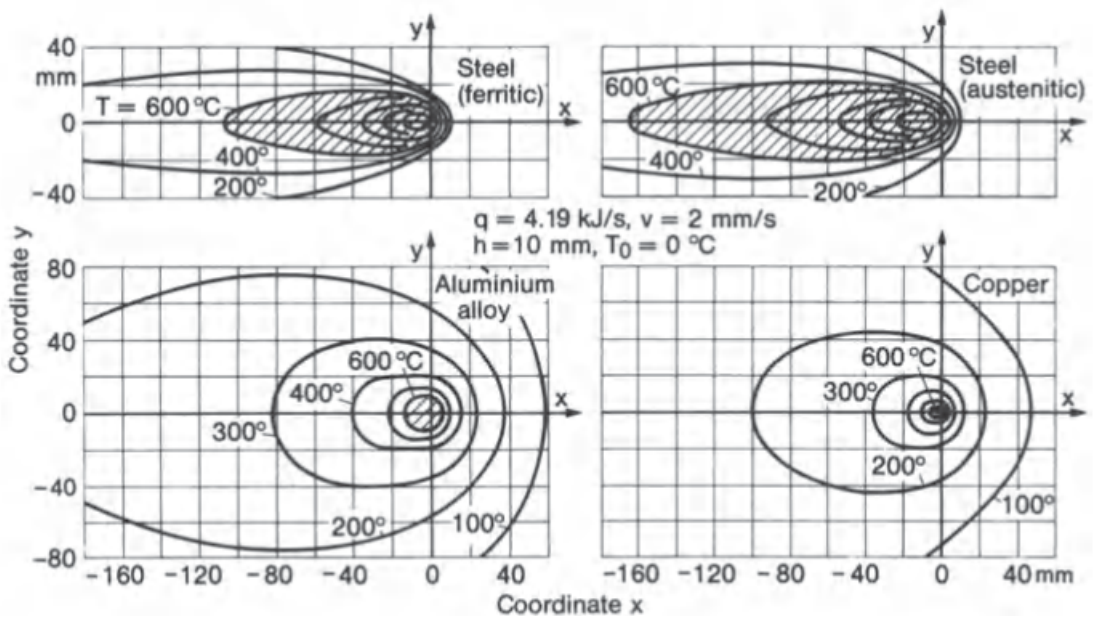



Figure 2.44: Temperature field around moving line source in plates of different materials, equal heat output $q$ and source velocity $v$ [1, 77].

Table 2.1: Thermal efficiency factor $k$ of welding processes [78]

| **Process no.** | **Welding process** | ***k*** |
|---|---|---|
| 12 | Submerged arc welding | 1.0 |
| 111 | Manual metal-arc welding | 0.8 |
| 131 | MIG welding | 0.8 |
| 135 | MAG welding | 0.8 |
| 114 | Self-shielded tubular-cored arc welding | 0.8 |
| 136 | Tubular-cored wire metal-arc welding with active gas shield | 0.8 |
| 137 | Tubular-cored wire metal-arc welding with inert gas shield | 0.8 |
| 141 | TIG welding | 0.6 |
| 15 | Plasma arc welding | 0.6 |

to residual stress. Thermal and transformation stresses do not occur in the homogeneous material provided all the areas of the component heat up and cool down simultaneously, i.e. provided no temperature differences occur at any time. The main factors that influence the strength of welded joint are shown in Figure 2.45 [1].

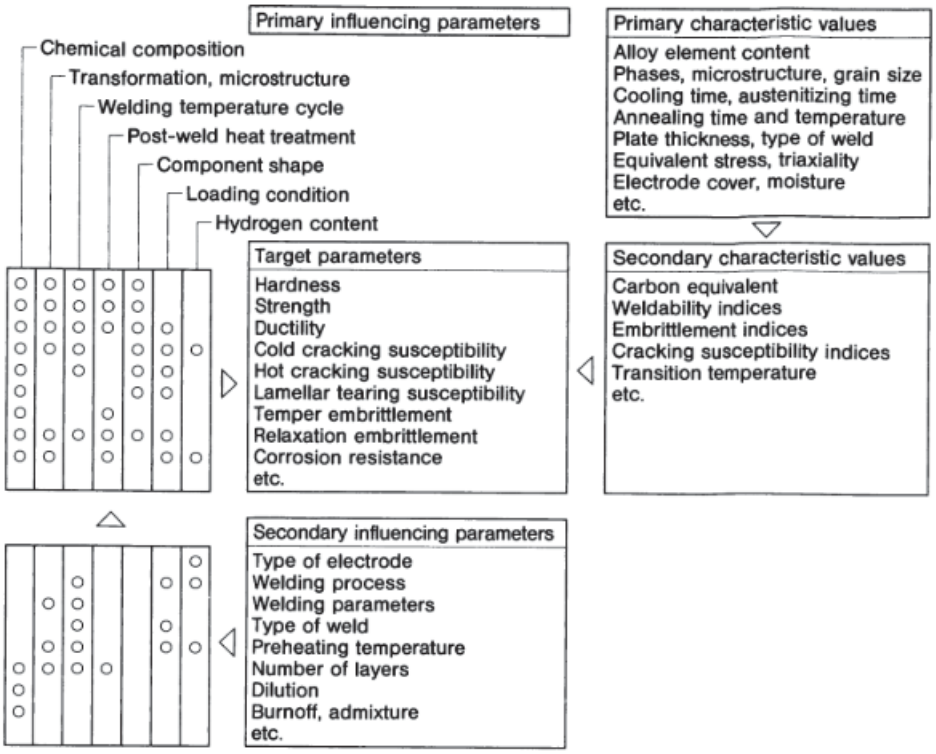



Figure 2.45: Parameters with major influence on strength of welded joints (primarily heat affected zone) constituting part of their weldability [1, 79].

### 2.6.1 Problem definition

During the welding process, the heated zone reaches a very high temperature compared to the surrounding area. As a consequence, the material expands but is restrained by the surrounding colder area, which gives rise to thermal stresses after cooling.

The three-bar analogy (Figure 2.46) is generally used to demonstrate how residual stresses form after welding. Considering three bars of equal length connected at their ends, with the one in the middle having a smaller diameter than the outer ones and zero stress at room temperature. If the middle bar is heated to a high enough temperature as in the case of welding, it will expand and pull on the sidebars creating a state of tension in the sidebars and compression in the middle bar. Because of the high temperature, the middle bar permanently deforms owing to plasticity. If the middle bar would not have been connected it would be shorter than the side bars after cooling. After cooling down to room temperature the middle bar contracts and thus induces a state of compression in the sidebars and tension in itself. Therefore, after welding it is expected that the welding region will be in tension and the base material in compression [66, 80].

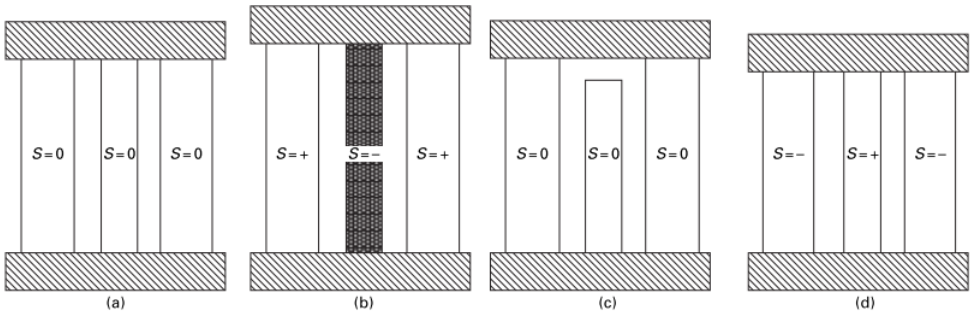



Figure 2.46: Three bar analogy. Room temperature (a); middle bar heated (b); room temperature middle bar disconnected (c); room temperature middle bar connected (d) [66].

The responsibility of dealing with distortions caused by the welding process falls in the scope of designers of welded structures and those who actually manufacture them. To effectively have some control over distortions, whether to reduce or prevent welding distortions altogether, all opportunities should be taken, most of which are available at the design stage, but are not always utilized. One of the most common oversimplifications is to treat the material and weld as homogeneous, isotropic, and stress-free. If the phase transformations of metals are not properly understood and taken into consideration, results can be unpredictable. One thing can be stated unequivocally, the use of intense heat sources in fusion welding will generate distortions. These distortions might be accepted if the magnitude or form could be predicted beforehand and taken into consideration at the design stage, even with robust estimations provided, the problem could be rendered manageable. However, this is not the case and even small changes in the factors and variables that arise during manufacturing affect the final distortion. Therefore, in order to successfully reduce distortions, designers, welding engineers, and metallurgists need to cooperate beyond a simple design change. The most common issue in the industry is the non-existence of a commonly accepted quantitative understanding of welding-induced distortions. During this process, high temperatures are needed to locally fuse the material together and ensure that the weld is structurally sound. Because yield strength varies with temperature, plastic deformations occur in thin-plate steel parts during the welding and cooling processes because of their rather slender nature, with the height and width being larger than the thickness and a very large area from which heat can quickly escape. Because of this rapid heat loss, the plastic strains cause the part to distort when completely cooled down. This issue is not usually accounted for in the initial phase of

production planning and manufacturers are faced with extra work they did not anticipate, which can prove costly and time-consuming to mend. The existing approach to controlling distortions is shown in Figure 2.47 [1–3, 66, 81].

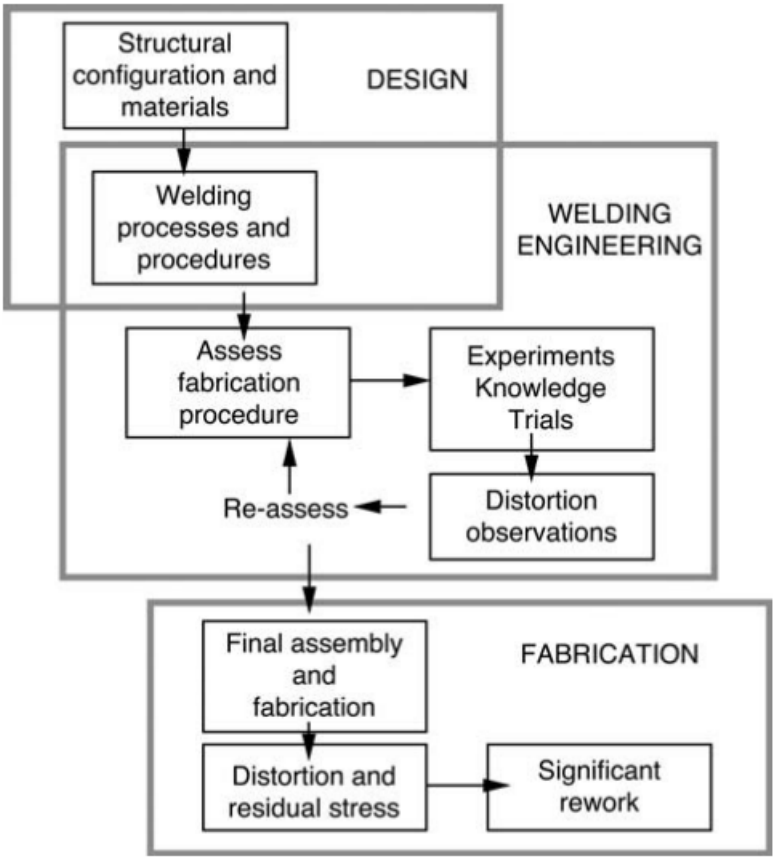



Figure 2.47: Existing approach to distortion control [3].

A new method of designing and testing the part before going into production is presented in Figure 2.48. Computational Welding Mechanics (CWM) represents the study of the complex thermo-mechanical phenomenon, which takes place during and after welding by means of physical models of real situations. The main advantage of this approach is that the welding is simulated, with full-scale experiments that can be carried out without increasing the costs or losing material and time. Another advantage that this method brings is that any parameters can be varied as needed and parametric studies can be performed easily and relatively inexpensively. The main downside is that for multi-pass submerged-arc welding it is difficult to reproduce the exact thermal cycles and results may vary significantly.

Because of recent advancements in the computational power of computers and a constant

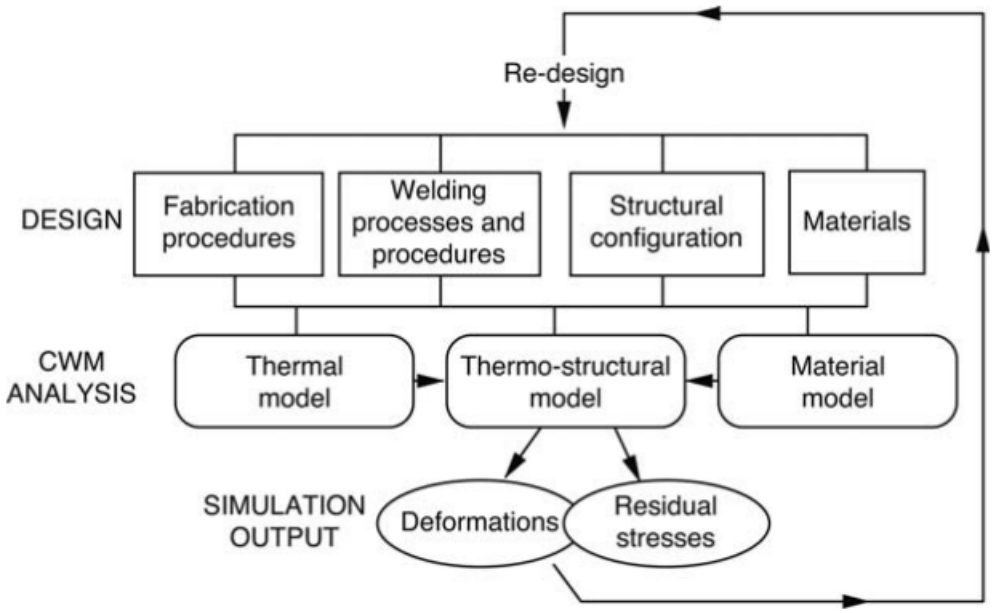



Figure 2.48: New proposed distortion control method [3].

improvement of finite element analysis, simulation tools are now a mature technology and have become an important part of the manufacturing process, proving to be highly feasible and capable of industrial application. Although commercial software for simulating welding has been developed, e.g. SYSWELD, the simplest way to perform an independent analysis is by uncoupling the thermal and mechanical effects of the welding process. First, the heat transfer problem is solved without reference to the mechanical aspects being considered, and only afterward, after simple algebraic transformations, the resulting temperature fields can be applied as loads on an elastic model of the studied part [3].

"To minimize distortions and departures from the specified design as a result of welding, a quantitative calculation of the deformations produced during different assembly and welding procedures is necessary" [82].

### 2.6.2 Weldability

Weldability refers to the welding suitability of the material, welding reliability of the design, and the welding feasibility in manufacturing; welding reliability of the design is assessed primarily on the basis of welding residual stress analysis while welding feasibility is assessed on the basis of welding deformation analysis, shown in Figure 2.49 [1].

In conformity with the classification presented in Figure 2.49, the parameters which have a major influence on weldability, can be grouped into:

- Material parameters e.g. chemical composition, microstructure, etc.;
- Design parameters e.g. dimensions, support system, loads, thickness and welding procedure;
- Manufacturing parameters e.g. welding velocity, bevel shape, welding sequence, tacking, preheating;

Decoupling, as presented in Figure 2.41, into Temperature fields, Stress and deformation fields, and Microstructural state fields; has proven its worth for FEA-based numerical analysis, in the sense that it provides good results for residual stress and welding deformations. It is important to incorporate microstructural transformations in the analysis (Figure 2.50), which depend not only on the chemical composition of the material but also on its thermal history (particularly the welding-related history). The influence of microstructure makes itself noticeable, especially in the heat-affected and fusion zone of the weld.

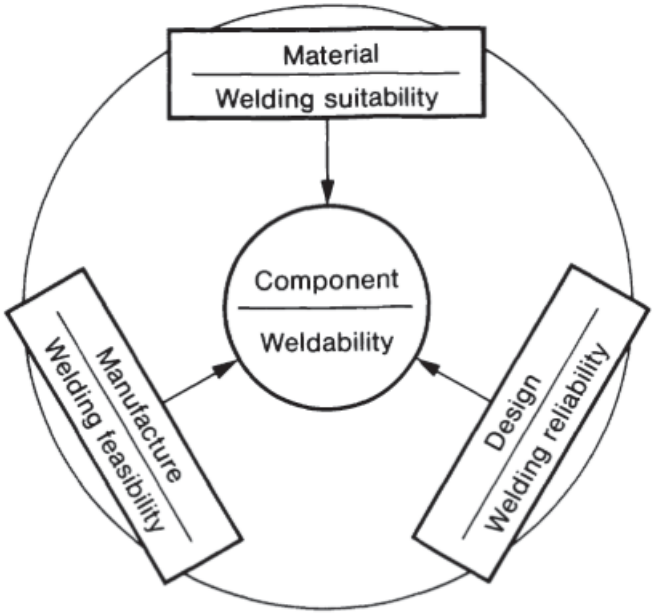



Figure 2.49: Definition of the term "weldability" [1, 83].

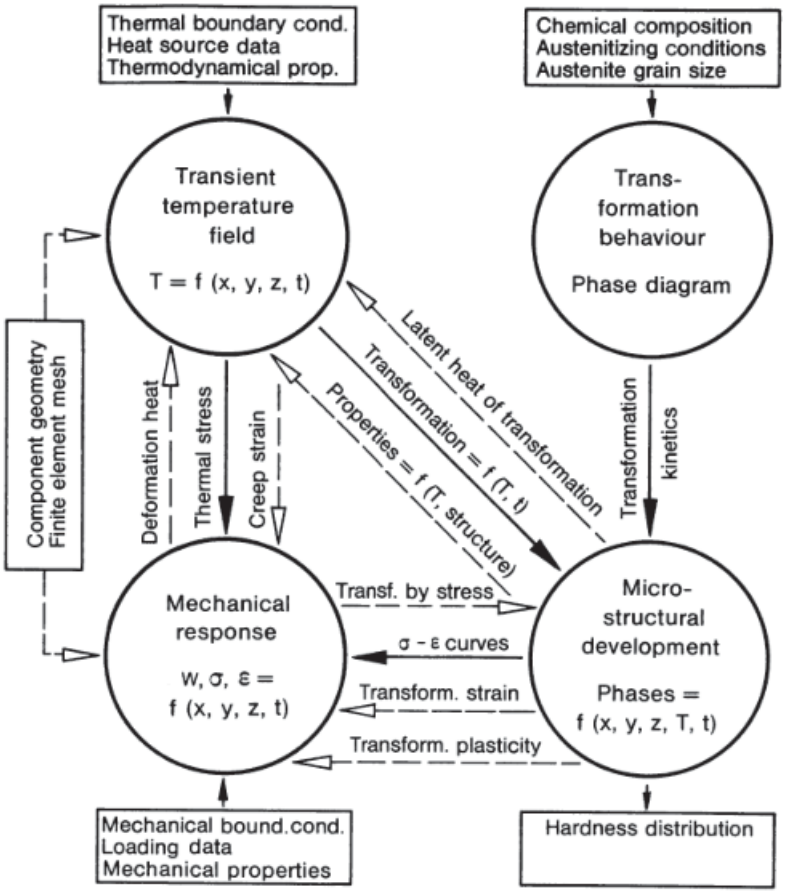



Figure 2.50: Extended graph of Figure 2.41 emphasizing the influence of microstructural transformation [1, 84].

### 2.6.3 Distortions

As a direct consequence of welding residual stress, temporary or permanent welding deformations, displacements or rotations can occur and the terms used to describe them are shrinkage, distortions, or warpage. Distortions are a manifestation of residual stress, if the welded structure possesses high stiffness, the residual stresses will be present in the structure without deforming, conversely if the structure can deform, part of the residual stress will be released via the deformation. The usual practice in the industry is to achieve high dimensional precision with low residual stress. Longitudinal shrinkage occurs at the weld seam and manifests as shortening in this area, which is restricted by the surrounding material which has not been affected by the welding temperature field. Transverse shrinkage of the weld seam manifests as a transverse shortening and closing of the weld groove. When the part is welded on one side this results in angular shrinkage, or if this shrinkage is restrained in bending distortions. This type of shrinkage is especially high in

the case of single-side multi-pass welds. In thin plates, compressive residual stresses can cause an unstable transverse deformation, known as buckling or warpage, which results in deflections normal to the plate. In transverse shrinkage, the part shrinks in the direction perpendicular to the welding direction. Angular change takes place in fillet and butt welds, where the angle of the plates changes after welding. Rotational distortion appears when a part opens as the welding progresses. Longitudinal shrinkage takes place when the part shrinks in the welding direction. Compressive residual stresses cause elastic instability, which leads to buckling. Bowing, or camber distortions, commonly known as longitudinal distortions are caused by non-balanced residual stresses with respect to the neutral axis of the part. These distortions usually form when the magnitude of residual stresses surpasses the yield strength of the material and plastic deformations occur, in the form of shape change. Another cause for distortions is the phase transformations that occur at high temperatures and produce volume changes in the material. When the steel part is heated and rapidly cooled, austenite that has a face-centered cubic structure transforms into martensite that has a tighter body-centered tetragonal structure. This phenomenon causes a volume change in the material structure and an increase in residual stress in the welded region. The six distortion types can be further divided into in-plane and out-of-plane modes. The transverse shrinkage, rotational distortions, and longitudinal shrinkage represent the in-plane modes, which are usually negligible and are taken into consideration by starting with larger parts when needed. While these modes receive little attention, the latter ones represent some of the most common distortions that can appear during welding and are difficult to control and predict. Structures comprised of thin section panels that are welded together are the most affected by these distortions. When buckling distortions appear, they usually are of large magnitude, and control methods should be applied to remove the source of the buckling. When thicker sections are used, they are more resistant to buckling distortions; the residual stresses usually result in bowing or angular out-of-plane modes. Angular distortions are caused by a similar mechanism to that seen in buckling, but the distortion is transverse to the welding direction and caused by shrinking near the fusion zone, resulting in an angle change. For mild steels, the areas above the 600°C isotherms have a lower yield strength and correspond to the middle bar in the three-bar analogy. As the weld cools down, this area shrinks owing to plastic deformations, thus lifting the plate and causing angular distortion. Bending distortions, also known as bowing or camber distortion, are caused by residual stresses,

which have not been balanced with respect to the neutral axis of the part. The welded region will shrink due to the phenomenon detailed previously and because it is located below the neutral axis of the stiffener cross-section causing longitudinal bending, thus lifting the center of the stiffener. Some of the main types of encountered distortions are shown in Figures 2.51 - 2.53 [1–3, 66].

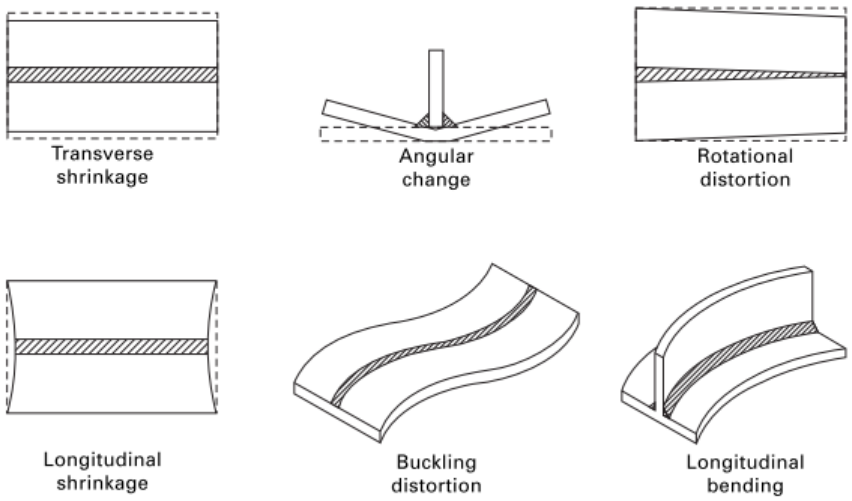



Figure 2.51: Types of distortions [66].

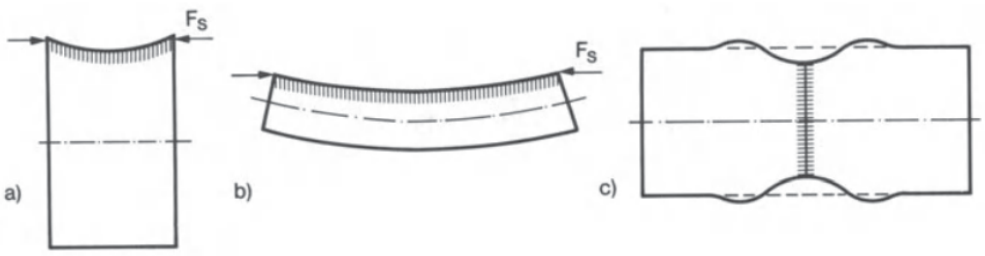



Figure 2.52: Cylindrical shell deformations [1].

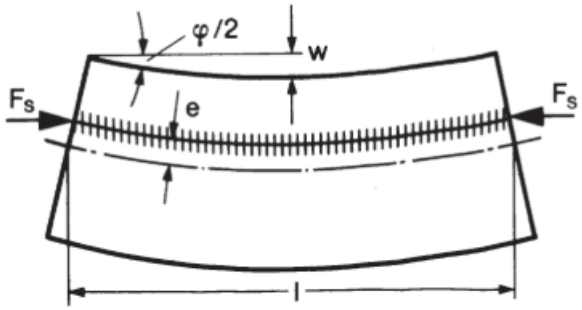



Figure 2.53: Rotational and deflective deformations [1].

### 2.6.4 Welding residual stress and distortion control methods

There are certain measures that can be undertaken that can address the problem of residual stresses and distortions. A problem that arises when dealing with these mitigating methods is that they can lead to the exhaustion of the material's ductility. Thus, the components failure limit may be closer than the state in which it was prior to applying any mitigating methods. The only way to remove this damage is to completely recrystallize the component by annealing. These measures can be further divided based on when they take place in regard to the actual welding process. Design and material measures can be applied prior to the welding process while manufacturing measures can be applied prior, during, or after welding [1–3, 66, 81].

Some of these measures are as follows:

- Appropriate design
- Presetting/offsetting
- Mechanical restraints
- Preheating
- Limiting the heat input and control of other weld parameters
- Thermal tensioning and heat sink welding
- Sequential welding
- Flame straightening/heat treatment
- Mechanical stress relief

The design of welded structures should render welding residual stresses and distortions controllable and fall under the responsibilities of the design engineer. They include but are not limited to configuration, dimensioning, sub-division into assemblies, joint type, etc. The main design measures that can be used are as follows [1–3, 66, 81]:

- Reducing weld length, plate thickness, throat thickness
- Use intermittent welds as opposed to continuous welds
- Use fillet welds as opposed to butt welds
- Subdivide into assemblies

The material selection process is based on the engineering requirements of the end product. It should ensure that the result is free of defects, have the required strength, and, poses the elastic

deformation capabilities required by the service loads. The main material characteristics that influence weld residual stresses and deformations are as follows [1–3, 66, 81]:

- $T_m$ - Melting temperature [°C]
- $a$ - Thermal diffusivity [$mm^2/s$]
- $\alpha$ - Thermal expansion [$1/°C$]
- $E$ - Elastic modulus [$kN/mm^2$]
- $\sigma_Y$ - Yield limit [$N/mm^2$]
- $K_{1c}$ - Fracture toughness [$N/mm^{3/2}$]

There is a wide range of manufacturing measures that can be applied to welded structures but they have limitations. If a structure was not properly designed they cannot fully remedy this issue. Some measures which can be applied are presented in Table 2.2.

Table 2.2: Manufacturing measures [1–3, 66, 81]

| **Prior/during welding** | **Post-weld** |
|---|---|
| Prefabrication | Annealing |
| Dimensional accuracy | Cold stretching |
| Groove cross-section and shape | Cold stretching |
| Multi-layer welding and layer sequence | Flame stress relieving |
| Tandem welding | Vibration stress relieving |
| Weld sequence | Hammering |
| Back-step welding | Rolling |
| Symmetrically simultaneous welding | Spot compression |
| Tacking | Spot heating |
| Preheating | Hot straightening |
| Simultaneous cooling | Cold straightening |
| Counter aligning | Flame straightening |
| Pre-shaping | Laser shock peening(LSP) |
| Bracing/fixing | |

## 2.7 Experimental techniques for assessing welding residual stress

### 2.7.1 Objective

The objective of this systematic review is to identify the latest experimental techniques used for assessing residual stress in welded parts or structures that can be used in the case of wind energy converter support systems.

A systematic review of the scientific literature in a specific area is important for identifying research questions, as well as justifying future research in the said area and synthesizing existing work in a manner that is fair and thorough [85].

The reasons for conducting a systematic review are:

- To summarize existing evidence, empirical evidence, benefits, and limitations in the current research area.
- To identify gaps in the current research knowledge in order to suggest areas for further investigation.
- To provide the necessary framework and background for future research activities.
- To examine the extent to which the empirical evidence supports or contradicts theoretical hypotheses or assists in the generation of new hypotheses.

Systematic reviews have a few advantages over traditional literature. A well-defined methodology makes it less likely that results will be biased, although it does not protect against publication bias in the primary studies. They can provide information about the effect of some phenomena across a wide range of settings and empirical methods. If studies give consistent results, systematic reviews provide evidence that the phenomenon is robust and transferable; otherwise, if the studies give inconsistent results, the sources of variation can be studied. In the case of quantitative studies, it is possible to combine data using meta-analysis techniques; this increases the likelihood of detecting real effects that individual smaller studies are unable to detect. On the other hand, systematic reviews require considerably more effort than traditional literature reviews; in addition, increased power for meta-analysis can also be a disadvantage since it is possible to detect small biases as well as true effects [85].

### 2.7.2 Methodology

The research question being addressed in the current study is:

- What are the current experimental techniques used to assess welding residual stress?

The systematic review has been elaborated and conducted by using the Preferred Reporting Items for Systematic Reviews and Meta-Analysis (PRISMA) method and guidelines in conjunction with "Guidelines for performing Systematic Literature Reviews in Software Engineering" developed by Barbara Kitchenham et al. at Keele University(US) and the University of Durham(UK) and adapted for the topic at hand. Several other studies on systematic review methodology were consulted during the process of conducting the review [85–89].

The databases chosen for the searches are Scopus, Science Direct, and Engineering Village. The initial search began with identifying relevant search terms. The first search was performed using "residual stress", "experimental technique" and "welding" using the Boolean operator AND between them. Subsequently, because a large number of studies returned when introducing the search terms, "residual stress" was replaced with "residual stress assessment" to narrow the search to studies that performed a type of measurement of this variable. The initial search results and keywords used are presented in Table 2.3. After the second search resulted in a very large number of studies, the search was narrowed down even further by applying the following filters, studies that were published between 2015 and 2019, in English and in the case of Scopus limited to articles only, as well as rearranging the search terms.

- Scopus search thread - "TITLE-ABS-KEY ( welding AND residual AND stress AND assessment AND experimental AND technique ) AND ( LIMIT-TO ( PUBYEAR , 2019 ) OR LIMIT-TO ( PUBYEAR , 2018 ) OR LIMIT-TO ( PUBYEAR , 2017 ) OR LIMIT-TO ( PUBYEAR , 2016 ) OR LIMIT-TO ( PUBYEAR , 2015 ) ) AND ( LIMIT-TO ( LANGUAGE , "English" ) ) AND ( LIMIT-TO ( DOCTYPE , "ar" ) ) ";
- Engineering Village search thread - "(((welding residual stress assessment experimental technique)) AND ((english WN LA) AND ((2019 OR 2018 OR 2017 OR 2016 OR 2015) WN YR)))";

In the case of Science Direct the terms "welding residual stress assessment experimental technique" was applied in the "Title, abstract or author-specified keywords" part of the Advanced Search window and "2015-2019" in the "Year(s)" section. The results from this search are shown

in Table 2.4. After retrieving the titles of the studies from the refined search, the full-text articles were downloaded and introduced in Mendeley, a reference-managing tool. Another three studies were identified from other sources, and because they were relevant to the subject, they were added to the total. Two studies were removed because that one was an Editorial and the full text was not available for the second one, afterwards a duplicate check was performed using Mendeley which resulted in 27 individual studies.

Table 2.3: Initial search terms and results

| Search terms | Database | No. of results |
|---|---|---|
| residual stress AND experimental technique AND welding | Scopus | 583 |
| | ScienceDirect | 22758 |
| | Engineering Village | 331 |
| residual stress assessment AND experimental technique AND welding | Scopus | 60 |
| | ScienceDirect | 7076 |
| | Engineering Village | 36 |

Table 2.4: Search results after refinement

| Database | No. of results |
|---|---|
| Scopus | 11 |
| ScienceDirect | 13 |
| Engineering Village | 16 |

After the full-text articles were obtained, the next step was to screen the abstracts and identify the studies that are eligible for inclusion. The inclusion criteria decided upon were as follows:

- The article must include results or measurements of residual stress derived from or reached through an experimental technique.

- The measured residual stress must be a byproduct of a welding procedure.
- The welding residual stress assessment method should not be X-ray diffraction, neutron diffraction or high-energy synchrotron diffraction[1].
- The article must be published between 2015 and 2019.
- The article must be in English.

After the screening of the abstracts and deciding which studies will be included in the review, the next step was to read the full-text articles and extract the relevant information from each of them. The results of the screening and inclusion process are shown in Figure 2.54. Because of the nature of the research question, the diverse application domain, and the irregularity of the studies, it was decided to extract the most relevant data from the studies. In order to simplify the presentation of the data points extracted from the included studies and compile them in a tabular form, a number was assigned to each of them. This is shown in Table 2.5 and Table 2.6.

Table 2.5: Assigned numbers for primary studies

| No. | Title |
|---|---|
| 1 | The NeT Task Group 4 residual stress measurement and analysis round robin on a three-pass slot-welded plate specimen |
| 2 | Welding residual stress analysis and fatigue strength assessment at elevated temperature for multi-pass dissimilar material weld between alloy 617 and P92 steel |
| 3 | Assessment of the contour method for 2-D cross sectional residual stress measurements of friction stirwelded parts of AA2024-T3 |
| 4 | DBEM crack propagation in friction stir welded aluminum joints |
| 5 | Hybrid technique to assess the fatigue performance of multiple cracked FSW joints |
| 6 | Investigation of the effects of the weld groove shape on the residual stress formation in the butt-welded plates |
| 7 | Assessment of weld residual stress measurement precision: Mock-up design and results for the contour method |
| 8 | Use of Contour Method for Welding Residual Stress Assessment |
| 9 | Assessment of Primary Slice Release Residual Stress Mapping in a Range of Specimen Types |
| 10 | Investigation of residual stress development in spiral welded pipe |
| 11 | Multiscale Measurements of Residual Stress in a Low-Alloy Carbon Steel Weld Clad with IN625 Superalloy |
| 12 | Residual stress measurements in offshore wind monopile weldments using neutron diffraction technique and contour method |

[1]These methods were not considered for this study because of the lack of access to facilities that can perform them in Portugal, a large amount of time needed to obtain results and the high costs involved.

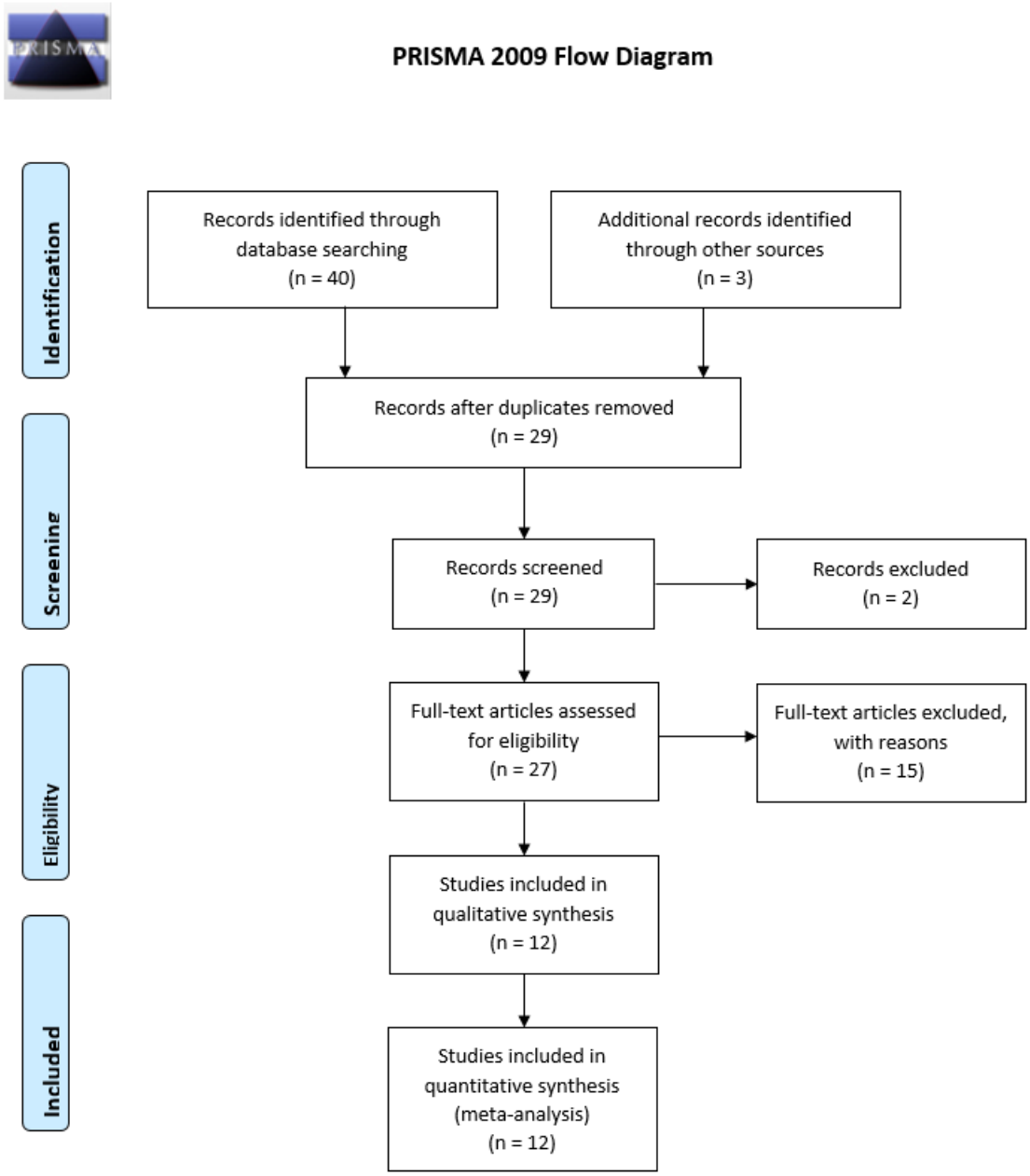



Figure 2.54: PRISMA flow diagram

Table 2.6: Data extracted from studies

| No. | Data point |
|---|---|
| 1 | Title |
| 2 | Material |
| 3 | Welding process |
| 4 | No. of weld passes |
| 5 | Filler material |
| 6 | Specimen type |
| 7 | Specimen size |
| 8 | Residual strees assessment technique |
| 9 | Comparison with numerical simulation |
| 10 | Observations |

### 2.7.3 Results

The results processed from the data extraction are variable because of a lack of information in a few studies and the fact that the articles tackled different welding techniques, as well as specimen types and materials. This information is tabulated in Table 2.7. A list of experimental techniques and methods used for assessing welding residual stress was compiled and further detailed.

Experimental techniques:

- Neutron diffraction[2]
- High-energy synchrotron diffraction[3]
- X-ray diffraction[4]
- The deep-hole drilling method
- The hole drilling method
- The contour method
- The cut-compliance method
- The slitting method
- Primary Slice Removal Mapping
- The split ring method
- The ultrasonic method

[2] See footnote 1
[3] See footnote 1
[4] See footnote 1

Table 2.7: Data extracted from primary studies

| No. | Material | Welding process | No. of weld passes | Filler material | Specimen type | Specimen size [mm] | Residual stress assessment technique | Comparison with numerical simulation |
|---|---|---|---|---|---|---|---|---|
| 1 | AISI 316L(N) steel | GTAW/TIG | 3 | AISI 316L | Plate | 198x150x18 | neutron and high energy synchrotron diffraction, surface X-ray diffraction, surface and deep hole drilling, the contour method, ultrasonics | Yes |
| 2 | Alloy 617/P92 steel | DCSP TIG | n/a | Thyssen 617 | Plate/Fatigue test specimen | n/a | the hole-drilling method | Yes |
| 3 | Aluminum alloy 2024-T3 | FSW | n/a | n/a | Plate | 200x60x4 | the cut-compliance method, the contour method | Yes |
| 4 | Aluminum alloy 2024-T3 | FSW | n/a | n/a | Plate | 194x60x4 | the contour method | Yes |
| 5 | Aluminum alloy 2024-T3 | FSW | n/a | n/a | Plate | 200x60x4 | the contour method | Yes |
| 6 | AISI 304 stainless steel | TIG/SMAW | 3 | ER 308L /E 308L-16 | Plate | 500x500x6 | the hole-drilling method | Yes |
| 7 | 316L stainless steel | GTAW | 8 | 308L | Plate | 1220x152.4x25.4 | the contour method and neutron diffraction | Yes |
| 8 | A36 steel | SAW | 1 | Lincoln L61 ø3.97 mm/Lincoln 860 flux | Plate | 6 x 76.2x25.4x12.7 + 0.5 mm shims between specimens | the contour method | Yes |
| 9 | 7050-T7451 aluminum/316 L stainless steel/Ti-6Al-4V titanium alloy/nickel alloy (Udimet-720Li) | Machining/GTAW/ EBW/Forging | 8 ( for each of the welding processes) | A52M ø0.89 mm ERNiCrFe-7A | T-section Bar/Plate/Plate/Turbine Disk | 82.55x50.80x254 t=6.35/1220x152.4x25.4/1220x152.4x25.4/ $Ø_{max=151.2}$ $H_{max=70.41}$ | primary slice removal mapping, the contour method, the slitting method | Partial |
| 10 | API 5L X70 high grade steel | n/a | n/a | n/a | Pipe | n/a | the hole drilling method/ the split ring method | Yes |
| 11 | 4330 low alloy carbon steel | GTAW weld cladding | 2 | IN625 nickel-based superalloy | Pipe | $Ø_{inner=}$126.8 L= 193.32 T=100.16 | X-Ray Diffraction, the hole drilling method, deep-hole drilling , the contour method | Yes |
| 12 | S355 G10+M steel | SAW tandem-twin | 25 (both sides) | S3Si/SA FB 1 55 AC H flux | Plate | 2600x800x90 | neutron diffraction, the contour method | Partial |

#### 2.7.3.1 The deep-hole drilling method

Deep-hole drilling (DHD) is a technique used to measure lock-in and applied residual stresses in materials and components. DHD is a mechanical strain relaxation technique that measures stress distribution along the axis of a reference hole drilled in the part or structure. This process is unique since it is capable of measuring stress without completely destroying the original component. The method consists of drilling a hole through the thickness of a part, measuring the diameter, and afterward cutting a circular slot around that hole (trepanning) by means of electric discharge machining (EDM), and then performing another measurement to detect changes in the initial diameter. The differences between the measured diameters before and after stress release enable the original residual stresses to be calculated using elasticity theory [90–92].

#### 2.7.3.2 The hole drilling method

The hole-drilling method (HDM) is a versatile method of measuring macroscopic residual stresses near the surface of a material and is one of the most used techniques because it does not involve high cost, and is quite fast and standardized. When the material is removed by drilling, relaxation occurs and the deformations around the hole are measured using strain gauges or optical methods. By using the strain data in a model, it is possible to calculate the original residual stress [93–97].

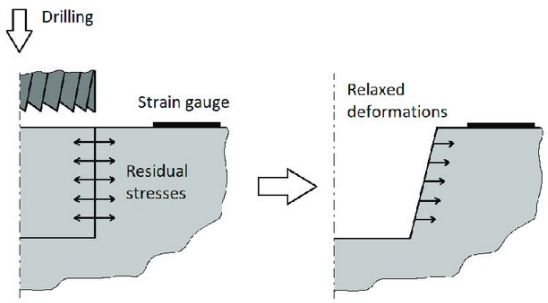



Figure 2.55: The principle of the hole-drilling method [98].

#### 2.7.3.3 The contour method

The contour method is based on the superposition principle, which assumes that materials will behave elastically during the relaxation of residual stress and that material removal introduces only negligible stress. The method starts by cutting the specimen of interest into two pieces by means of

wire EDM (electric discharge machining) and then measuring the out-of-plane deformation profile that occurs. The reverse of the resulting deformations are prescribed to a FE model and an elastic stress analysis is performed. The result is a two-dimensional map of residual stress normal to the cutting plane [16, 95, 96, 99].

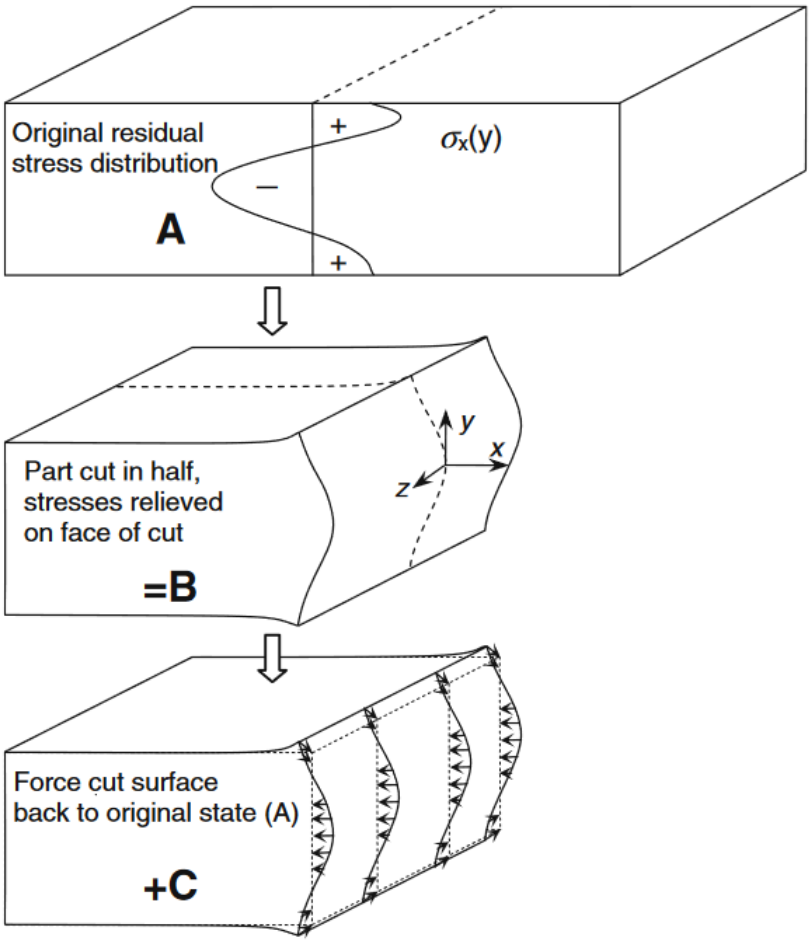



Figure 2.56: The principle of the contour method [100].

#### 2.7.3.4 The cut-compliance method

The cut compliance method was developed to measure residual stress profiles. The idea is to release them by introducing progressively a cut into the considered body. From the strain change due to progressive cutting, it is possible to calculate the distribution of the released stresses. Since the method uses fracture mechanics principles the stress intensity factor due to residual stresses is delivered as well. Being a special type of residual stress, the distribution of the contact stresses

of fatigue crack closure and the corresponding closure stress intensity factors can be suitably determined by this method. Furthermore, it enables the residual stresses in front of the crack tip to be determined, which in crack retardation plays a role as important as the closure effects. The basic theoretical relations for some frequently used fatigue specimens are analytically derived. They also can serve to evaluate the contact stresses from the commonly used unloading compliance technique, which is often used to identify crack closure effects. Some preliminary examples demonstrate the capability of the suggested method [101].

#### 2.7.3.5 The slitting method

The slitting method is a technique for measuring through-thickness residual stress normal to a plane cut through a part. It involves cutting a slit (a thin slot) in increments of depth through the thickness of the workpiece and measuring the resulting deformations as a function of slit depth. Residual stress as a function of the through-thickness position is determined by solving an inverse problem using measured deformations [102].

#### 2.7.3.6 Primary slice removal mapping

PSR mapping is a method that combines the contour method and the slitting method in order to determine multiple components of residual stress. First, the contour method is used to obtain the residual stress normal to the cutting plane. Next thin slices are removed parallel to the contour method plane. During slice removal, the residual stress will change by an amount called the PSR stress. By using elastic superposition, all the determined stresses are summed to obtain the initial residual stress present in the part [16].

#### 2.7.3.7 The split ring method

The Split-ring test is mostly adopted for industrial inspection of components. The approach in this method is to measure the deflection in components after sectioning. The deformation measurements are then combined with an elasticity solution to obtain the residual stresses in a tube or pipe. Many researchers have analyzed the split ring test and provided different equations for the estimation of residual hoop stress in a pipe. In the splitting method, the longitudinal cut is made in a ring of pipe through the wall thickness. The ring has been marked before splitting. After

splitting, the marked points are displaced due to the release of residual stress which causes to open or close the ring. A moment must be applied at two ends to bring the ring to its original position. The moment would be equivalent and opposite in direction to the residual moment which caused the deformation after splitting [18].

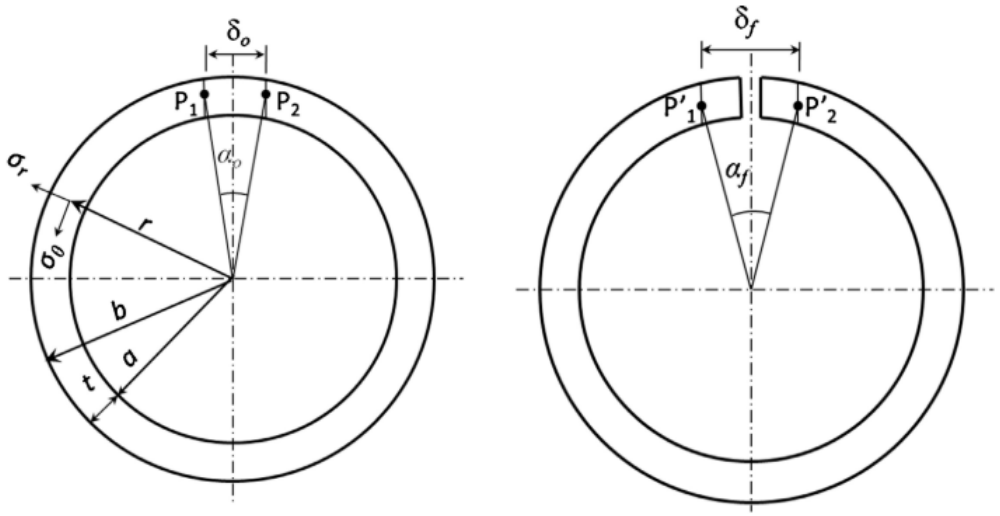



Figure 2.57: The principle of the split ring method [18].

#### 2.7.3.8 The ultrasonic method

Ultrasonic methods are based on the velocity of ultrasonic waves that are sent through the part. Changes in the speed of the waves can be detected when stress is present. Different types of waves can be used to achieve this, but a common technique is that of longitudinal critically refracted waves (LCR) [96].

### 2.7.4 Conclusion

Although all of the presented techniques can obtain residual stress measurements and distributions from welded parts, in the particular case of wind-energy converter support structures, namely steel tubular towers, the most easily employed methods are the contour method and primary slice release mapping mainly because of the large dimensions of the parts involved. The contour method provides an accurate measurement of the in-plane residual stress and its distribution but can induce some stress during the cutting process as well as some inaccurate results if not performed accordingly. If the need for a more in-depth measurement of residual stress arises, primary slice

removal mapping can be employed, even if the process is more time-consuming. The relatively low costs involved in using these techniques recommend them when the need for accurate welding residual stress measurements may arise.

## 2.8 Summary

Wind power has played a part in human history since the dawn of time, first powering ships and later powering our world. During the production process of HAWT support systems, SAW and the parameters chosen plays a very important role. The welding process has an effect on the mechanical properties, microstructure, distortions, and residual stresses of the resulting structures and defines its behavior. The changes that occur in the material and their non-linear nature govern its life cycle, performance, and structural integrity.

# Chapter 3

# Materials and methods

## 3.1 Introduction

In this chapter, the chemical composition and mechanical properties of the materials used in the experimental work are presented. Additionally, a detailed description of the specimens and procedures are provided.

## 3.2 Structural Steel

Structural steel represents a type of steel mainly used in the construction sector that comes in a variety of products. Most structural steel usable products come in the form of plates or beams with typical cross-sections. The properties of structural steel are regulated by standards in most industrialized countries. The most common shapes that structural steel comes in are I profiles, H profiles, T profiles, U profiles, L profiles, Z profiles, hollow sections, rail profiles, bars, rods, or plates. All European structural steels must comply with EN 10025.

While most structural steel products are made by hot or cold rolling, others are manufactured using welding procedures. The European standard that governs the design of steel structures is EN 1993. Structural steel comes labeled with a code, which describes its properties, manufacturing method, and material properties. A typical denomination is described as S355JR+NL, where S denotes structural, 355 denotes the yield strength in $N/mm^2$ or the equivalent MPa, and JR denotes

the material toughness by reference to Charpy impact test values and NL designates normalized. The minimum yield strength at a nominal thickness of 16 mm is 235, 275, 355, 420, 450, and 460, although some grades are more commonly used than others. Higher grades are available in quenched and tempered material (500, 550, 620, 690, 890, and 960).

In the case of tubular steel towers that support wind energy converters, structural steel plates and flanges are used for manufacturing.

### 3.2.1 Material properties

The two samples analyzed were provided by two companies: *Tegopi* and *ASM*. The samples were extracted from door cut-outs with circumferential welds between two shells (Figures 3.1 and 3.2); Tegopi used *S355J0+N* steel with *ESAB OK flux 10.72* and *ESAB OK Autrod 12.22 (4 mm)* wire with a double-V bevel for the butt weld, while ASM used *S355J2+N* steel with *OERLIKON OP121TT flux* and *OERLIKON OESD3 (4 mm)* wire with a single-U bevel. The samples obtained from Tegopi (Figure 3.3) and ASM (Figure 3.4) will be henceforth referred to as **Sample 1 (Tegopi)** and **Sample 2 (ASM)**. Both samples were welded using multi-pass SAW adjusting the parameters in accordance with their internal welding specifications. The chemical composition of the steels is shown in Tables 3.1 and **??**, while the chemical composition and mechanical properties of the flux-wire combinations are shown in Tables 3.4 - 3.6. The chemical, mechanical and thermal properties were obtained from the manufacturers and standards.

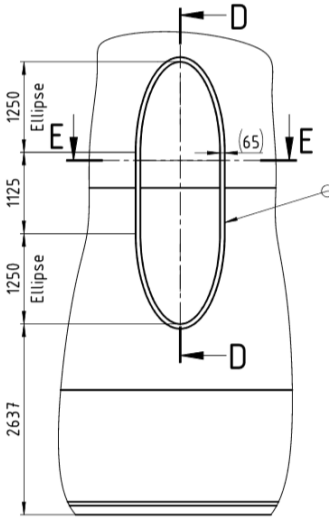



Figure 3.1: Door cut-out extracted from blueprint. Courtesy of Tegopi.



Figure 3.2: Doorframe after welding.



Figure 3.3: Sample 1.

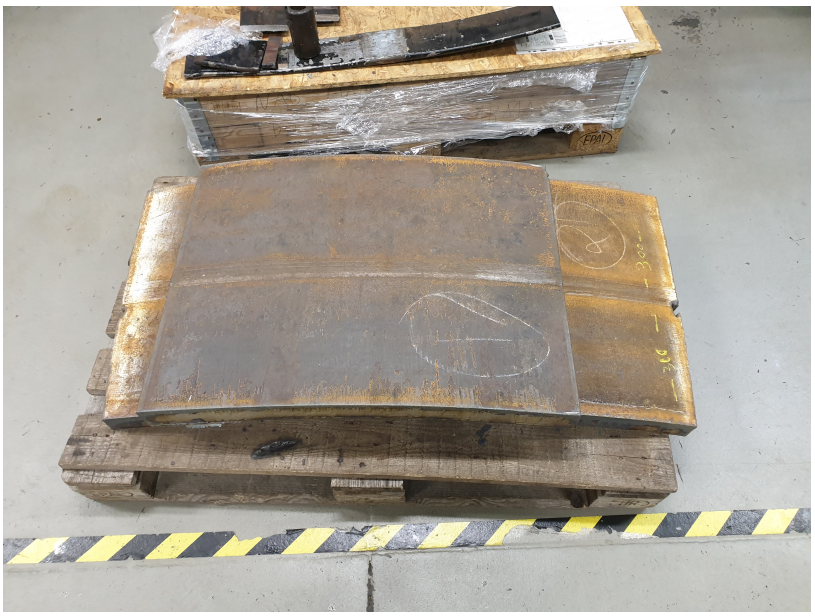


Figure 3.4: Sample 2.

Table 3.1: Chemical composition of S355 J0+N.

| **C [%]** | **Mn [%]** | **Si [%]** | **P [%]** | **Cu [%]** | **Ni [%]** | **Cr [%]** | **Mo [%]** | **Al [%]** | **V [%]** | **Nb [%]** | **Ti [%]** | **Sn [%]** | **N [%]** | **B [%]** | **H [%]** |
|---|---|---|---|---|---|---|---|---|---|---|---|---|---|---|---|
| 0.17 | 1.49 | 0.24 | 0.01 | 0.030 | 0.030 | 0.030 | <0.005 | 0.031 | < 0.005 | 0.022 | <0.005 | <0.005 | 0.006 | < 0.005 | 0.0003 |

Table 3.2: Chemical composition of S355 J2+N.

| **C [%]** | **Mn [%]** | **Si [%]** | **P [%]** | **Cu [%]** | **Ni [%]** | **Cr [%]** | **Mo [%]** | **Al [%]** | **V [%]** | **Nb [%]** | **Ti [%]** | **S [%]** | **N [ppm]** | **B [ppm]** | **H [%]** |
|---|---|---|---|---|---|---|---|---|---|---|---|---|---|---|---|
| 0.16 | 1.38 | 0.34 | 0.011 | 0.014 | 0.082 | 0.017 | 0.0028 | 0.00 | 0.00 | 0.00 | 0.00 | 0.021 | 34.33 | 2.17 | 0.00 |

Table 3.3: Toughness properties of S355J0+N and S355 J2+N.

| Material | Impact absorbed energy [J] | | | | Impact toughness [J/cm2] | Temperature [° C] |
|---|---|---|---|---|---|---|
| | 1 | 2 | 3 | Average | | |
| S355 J0+N | 240 | 241 | 233 | 238 | 298 | 0 ° C |
| S355 J2+NR | 200 | 224 | 217 | 214 | 267 | - 20 ° C |

Table 3.4: Chemical composition of the flux used in the welding process.

| Flux analysis | Sample number | |
|---|---|---|
| | 1 | 2 |
| CaO+MgO [%] | 27 | 35 |
| $CaF_2$ [%] | 20 | 25 |
| $Al_2O_3$+MnO [%] | 28 | 20 |
| $SiO_2$+$TiO_2$ [%] | 16 | 15 |

Table 3.5: Chemical composition of the wires used in the welding process.

| Sample no. | C [%] | Mn [%] | Si [%] | P [%] | S [%] | Cu [%] | Ni [%] | Cr [%] | Mo [%] |
|---|---|---|---|---|---|---|---|---|---|
| 1 | 0.11 | 1.04 | 0.21 | 0.011 | 0.009 | 0.100 | 0.020 | 0.050 | 0.01 |
| 2 | 0.1 | 1.7 | 0.3 | 0.01 | 0.006 | 0.004 | - | - | - |

Table 3.6: Mechanical properties of the flux-wire combination as welded.

| Sample No. | Yield Strength [MPa] | Tensile Strength [MPa] | Elongation [%] | Impact Energy ISO-V [J] | | | |
|---|---|---|---|---|---|---|---|
| | | | | Temperature [C] | | | |
| | | | | -30 | -40 | -50 | -60 |
| 1 | 415 | 500 | 30 | 120 | 100 | 70 | 50 |
| 2 | $\geq$450 | 530-560 | $\geq$25 | - | $\geq$100 | $\geq$70 | - |

### 3.2.2 Mechanical properties

S355 is a low-carbon, manganese, medium tensile strength steel, which possess good welding and high impact energy absorption properties at lower temperatures. The typical mechanical properties are as follows:

- Unit mass $\rho_a = 7850\ \mathrm{kg/m^3}$
- Modulus of elasticity $E = 210\,000\ \mathrm{N/mm^2}$
- Shear Modulus $G = \frac{E}{2(1+\nu)} \approx 81\,000\ \mathrm{N/mm^2}$
- Poisson's ratio in elastic stage $\nu = 0.3$
- Coefficient of linear thermal expansion $\alpha = 12 \cdot 10^{-6}$ per $K$ (for T $\leq$ 100°C)
- Yield strength $f_y\ \mathrm{N/mm^2}$ (Table 3.7)
- Ultimate tensile strength $f_u\ \mathrm{N/mm^2}$ (Table 3.7)

Ductility requirements:

- $f_y/f_u \geq 1.10$;
- Elongation at failure not less than 15%;
- $\varepsilon_u \geq 15 \cdot \varepsilon_Y$, where the yield strain $\varepsilon_y = f_y/E$

Table 3.7: Nominal values of yield strength $f_y$ and ultimate tensile strength $f_u$ for hot rolled structural steel [103].

| Standard and steel grade | Nominal thickness of the element $t$ [mm] | | | |
|---|---|---|---|---|
| | t $\leq$ 40 mm | | 40 mm < t $\leq$ 80 mm | |
| | $f_y[N/mm^2]$ | $f_u[N/mm^2]$ | $f_y[N/mm^2]$ | $f_u[N/mm^2]$ |
| **EN 10025-2** | | | | |
| S 235 | 235 | 360 | 215 | 360 |
| S 275 | 275 | 430 | 255 | 410 |
| S 355 | 355 | 490 | 335 | 470 |
| S 450 | 440 | 550 | 410 | 550 |
| **EN 10025-3** | | | | |
| S 275 N/NL | 275 | 390 | 255 | 370 |
| S 355 N/NL | 355 | 490 | 335 | 470 |
| S 420 N/NL | 420 | 520 | 390 | 520 |
| S 460 N/NL | 460 | 540 | 430 | 540 |

### 3.2.3 Thermal properties

The mechanical properties of steel change based on temperature and rate of temperature change. For heating rates between 2 and 50 K/min, strength and deformation properties can be obtained by using the relationship in Figure 3.5, Table 3.8 and the by applying the corresponding reduction factors shown in Table 3.9 and Figure 3.6.

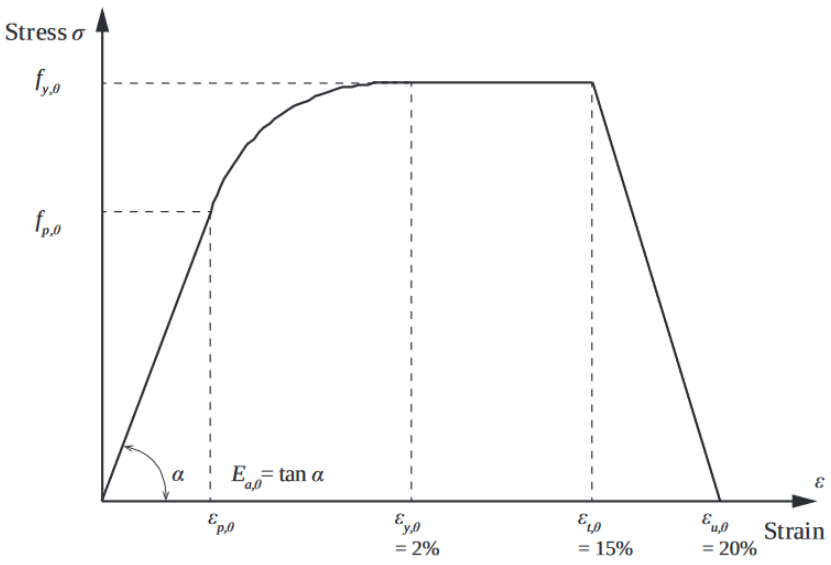



Figure 3.5: Stress-strain relationship for carbon steel at elevated temperatures [103, 104].

where:

$f_{y,\theta}$ = effective yield strength

$f_{p,\theta}$ = proportional limit

$E_{a,\theta}$ = slope of the linear elastic range

$\varepsilon_{p,\theta}$ = strain at the proportional limit

$\varepsilon_{y,\theta}$ = yield strain

$\varepsilon_{t,\theta}$ = limiting strain for yield strength

$\varepsilon_{u,\theta}$ = ultimate strain

#### 3.2.3.1 Thermal elongation

The relative thermal elongation of steel is determined using Equations 3.1, 3.2 and 3.3 [105].

Table 3.8: Stress-strain relationship for carbon steel at elevated temperatures [103, 104].

| Strain range | Stress $\sigma$ | Tangent modulus |
|---|---|---|
| $\varepsilon \le \varepsilon_{p,\theta}$ | $\varepsilon E_{a,\theta}$ | $E_{a,\theta}$ |
| $\varepsilon_{p,\theta} < \varepsilon < \varepsilon_{y,\theta}$ | $f_{p,\theta} - c + (b/a)\left[a^2 - (\varepsilon_{y,\theta} - \varepsilon)^2\right]^{0.5}$ | $\frac{b(\varepsilon_{y,\theta} - \varepsilon)}{a\left[a^2 - (\varepsilon_{y,\theta} - \varepsilon)^2\right]^{0.5}}$ |
| $\varepsilon_{y,\theta} \le \varepsilon \le \varepsilon_{t,\theta}$ | $f_{y,\theta}$ | 0 |
| $\varepsilon_{t,\theta} < \varepsilon < \varepsilon_{u,\theta}$ | $f_{y,\theta}\left(1 - (\varepsilon - \varepsilon_{t,\theta})/(\varepsilon_{u,\theta} - \varepsilon_{t,\theta})\right)$ | - |
| $\varepsilon = \varepsilon_{u,\theta}$ | 0.00 | - |
| Parameters | $\varepsilon_{p,\theta} = f_{p,\theta}/E_{a,\theta}$ $\varepsilon_{y,\theta} = 0.02$ | $\varepsilon_{t,\theta} = 0.15$ $\varepsilon_{u,\theta} = 0.20$ |
| Functions | $a^2 = (\varepsilon_{y,\theta} - \varepsilon_{p,\theta})(\varepsilon_{y,\theta} - \varepsilon_{p,\theta} + c/E_{a,\theta})$<br>$b^2 = c(\varepsilon_{y,\theta} - \varepsilon_{p,\theta})E_{a,\theta} + c^2$<br>$c = \frac{(f_{y,\theta} - f_{p,\theta})^2}{(\varepsilon_{y,\theta} - \varepsilon_{p,\theta})E_{a,\theta} - 2(f_{y,\theta} - f_{p,\theta})}$ | |

Table 3.9: Reduction factors for stress-strain relationship of carbon steel at elevated temperatures [103].

| Steel temperature $\theta_a$ | Reduction factors at temperature $\theta_a$ | | |
|---|---|---|---|
| | $k_{y,\theta} = f_{y,\theta}/f_y$ | $k_{p,\theta} = f_{p,\theta}/f_y$ | $k_{E,\theta} = E_{a,\theta}/E_a$ |
| 20 °C | 1.000 | 1.000 | 1.000 |
| 100 °C | 1.000 | 1.000 | 1.000 |
| 200 °C | 1.000 | 0.807 | 0.900 |
| 300 °C | 1.000 | 0.613 | 0.800 |
| 400 °C | 1.000 | 0.420 | 0.700 |
| 500 °C | 0.780 | 0.360 | 0.600 |
| 600 °C | 0.470 | 0.180 | 0.310 |
| 700 °C | 0.230 | 0.075 | 0.130 |
| 800 °C | 0.110 | 0.050 | 0.090 |
| 900 °C | 0.060 | 0.038 | 0.068 |
| 1000 °C | 0.040 | 0.025 | 0.045 |
| 1100 °C | 0.020 | 0.013 | 0.023 |
| 1200 °C | 0.000 | 0.000 | 0.000 |

- for 20°C $\le \theta_a <$ 750°C

$$\Delta l/l = 1.2 \cdot 10^{-5}\theta_a + 0.4 \cdot 10^{-8}\theta_a^2 - 2.416 \cdot 10^{-4} \tag{3.1}$$

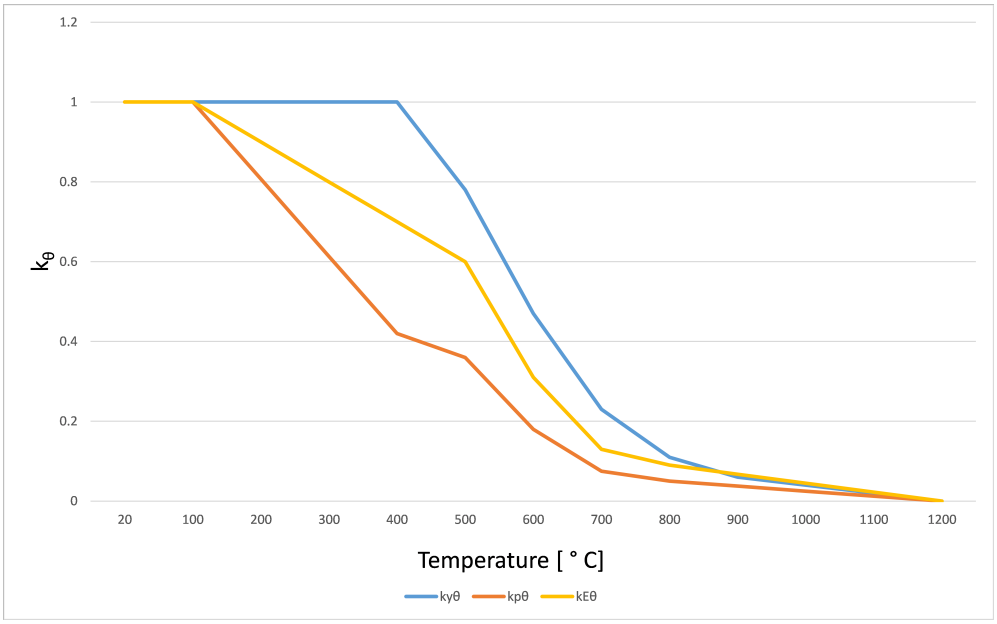



Figure 3.6: Reduction factors for stress-strain relationship of carbon steel at elevated temperatures [103].

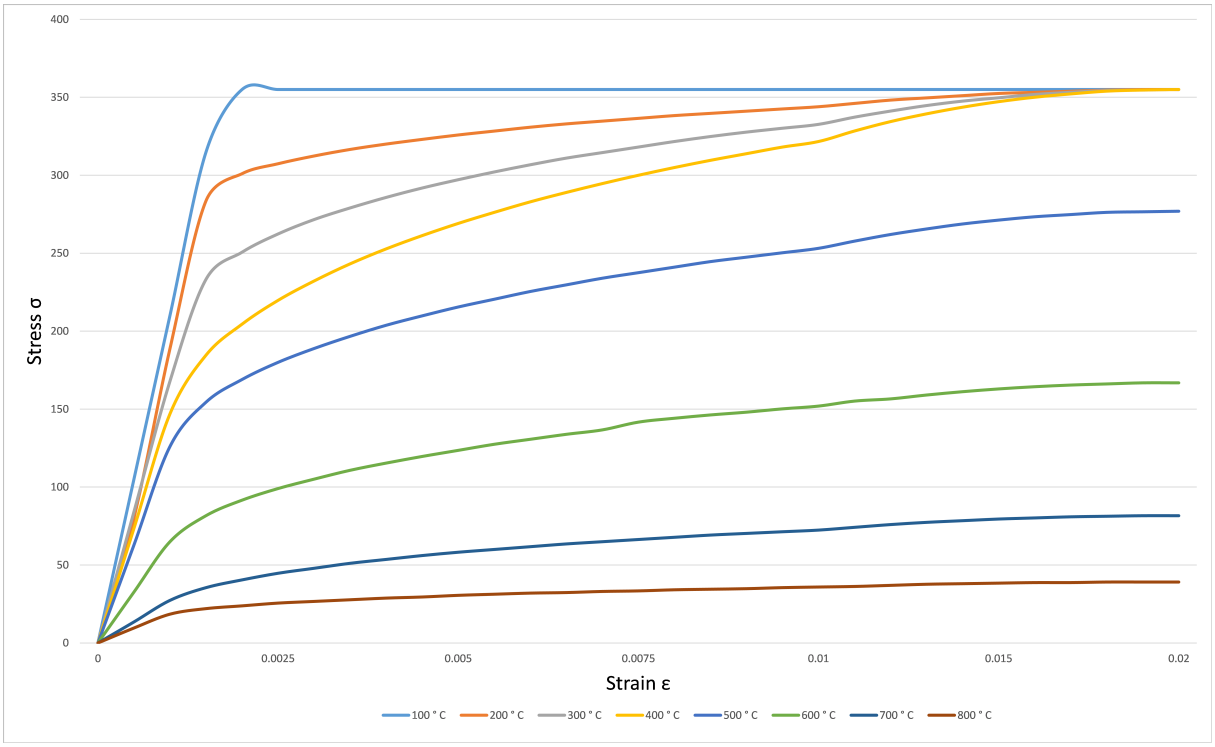



Figure 3.7: Stress-strain relationship of S355 at elevated temperatures [103, 104].

- for $750°C \leq \theta_a \leq 860°C$

$$\Delta l/l = 1.1 \cdot 10^{-2} \tag{3.2}$$

- for 860°C < $\theta_a \leq$ 1200°C

$$\Delta l/l = 2 \cdot 10^{-5}\theta_a - 6.2 \cdot 10^{-3} \tag{3.3}$$

where:

$l$ = the length at 20°C

$\Delta l$ = the temperature induced elongation

$\theta_a$ = the steel temperature [20°C]

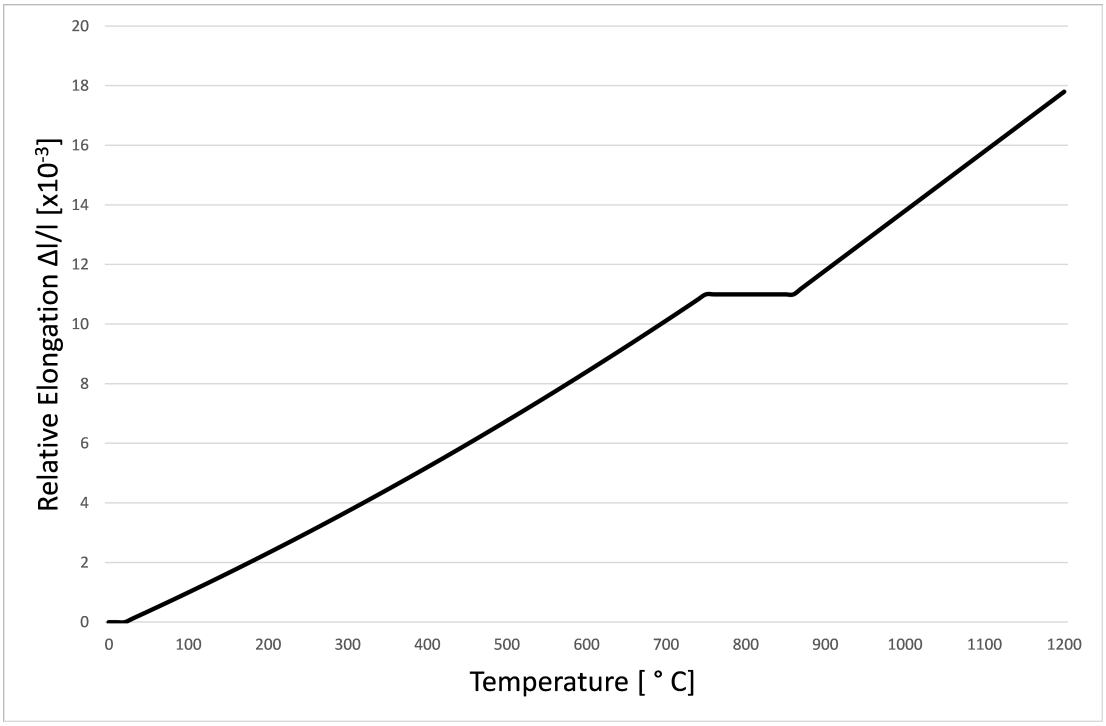



Figure 3.8: Relative thermal elongation of carbon steel [103].

### 3.2.3.2 Specific heat

The specific heat of steel can be obtained by using Equations 3.4, 3.5, 3.6 and 3.7 [105].

- for 20°C $\leq \theta_a <$ 600°C

$$c_a = 425 + 7.73 \cdot 10^{-1}\theta_a - 1.69 \cdot 10^{-3}\theta_a^2 + 2.22 \cdot 10^{-6}\theta_a^3 \quad [J/kgK] \tag{3.4}$$

- for $600°C \leq \theta_a < 735°C$

$$c_a = 666 + \frac{13002}{738 - \theta_a} \quad [J/kgK] \tag{3.5}$$

- for $735°C \leq \theta_a < 900°C$

$$c_a = 545 + \frac{17820}{\theta_a - 731} \quad [J/kgK] \tag{3.6}$$

- for $900°C \leq \theta_a \leq 1200°C$

$$c_a = 650 \quad [J/kgK] \tag{3.7}$$

where:

$\theta_a$ = the steel temperature [20°C]

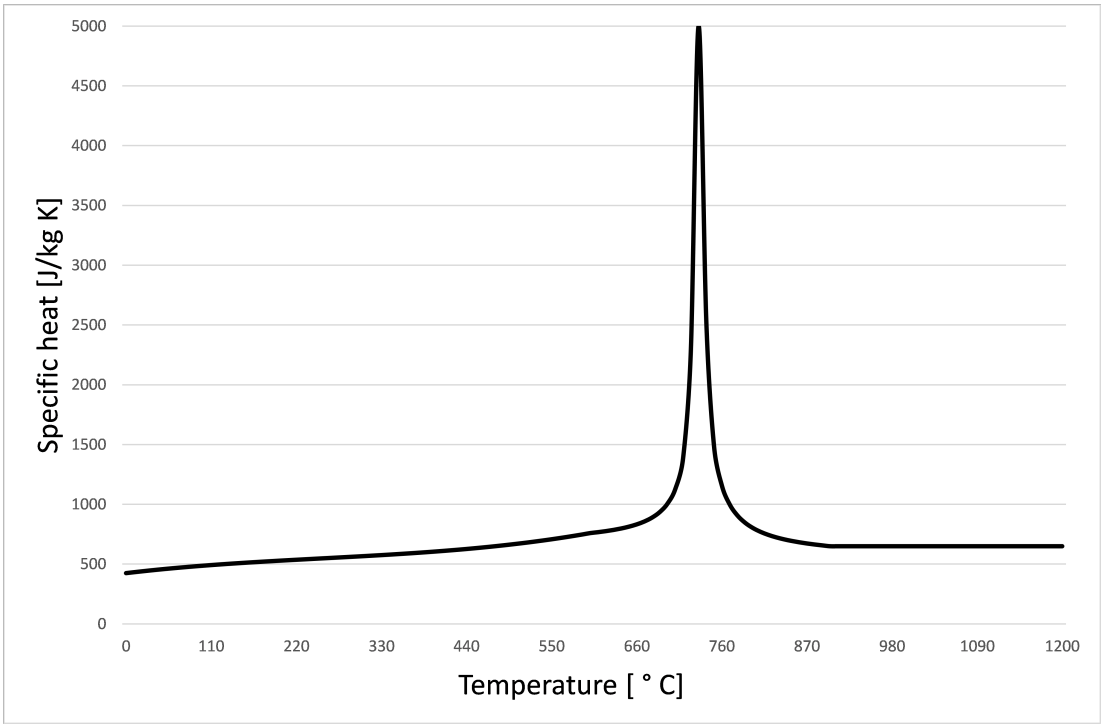



Figure 3.9: Specific heat of carbon steel [103].

#### 3.2.3.3 Thermal conductivity

The thermal conductivity of steel can be obtained by using Equations 3.8 and 3.9 [105].

- for 20°C $\leq \theta_a <$ 800°C

$$\lambda_a = 54 - 3.33 \cdot 10^{-2} \theta_a \quad [W/mK] \tag{3.8}$$

- for 800°C $\leq \theta_a <$ 1200°C

$$\lambda_a = 27.3 \quad [W/mK] \tag{3.9}$$

where:

$\theta_a$ = the steel temperature [20°C]

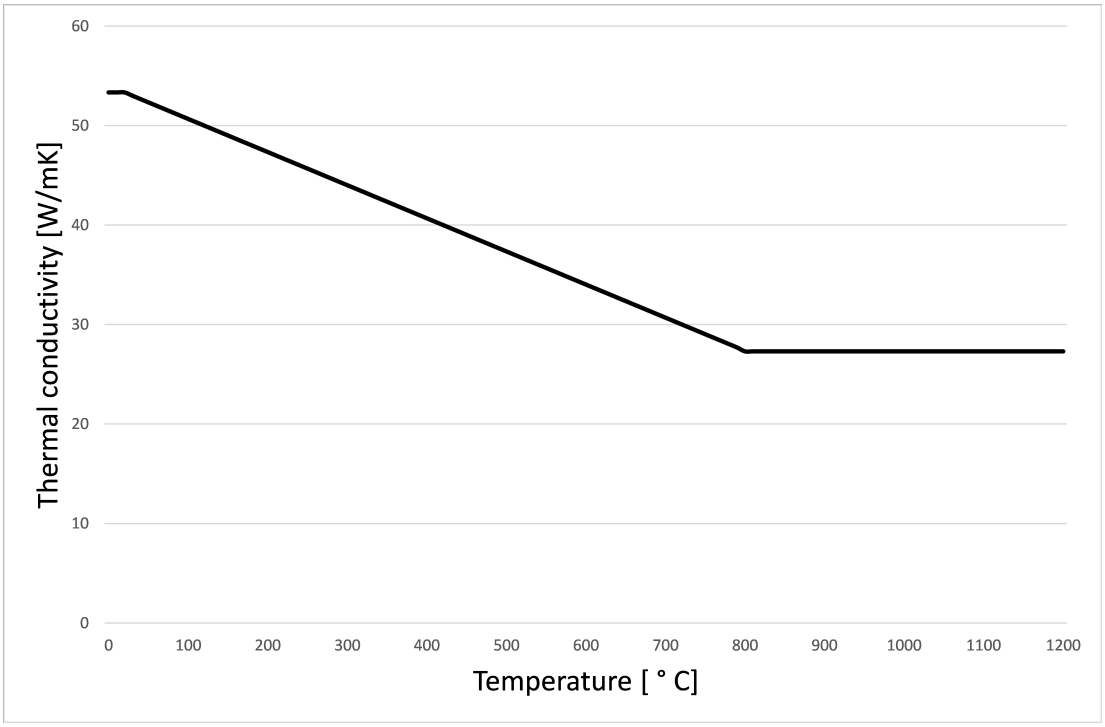



Figure 3.10: Thermal conductivity of carbon steel [103].

Further information can be found in the literature and standards.

## 3.3 Experimental work in Residual Stresses and Post-Welding Metallurgy

### 3.3.1 The Contour method

The contour method is a stress relaxation method, where residual stresses are obtained by measuring deformations after the relaxation has occurred. The contour method, based on Brueckner's superposition principle, evaluates residual stress levels by means of carefully cutting the specimen of interest into two pieces using wire electric discharge machining (WEDM) and then measuring the out-of-plane deformation profile that occurs after stress relaxation. The resulting deformations are then averaged and introduced in an un-deformed FE elastic model, filtering out experimental noise, applying the reverse of the averaged profile as nodal prescribed displacement boundary conditions, and performing elastic stress analysis. The finite element model takes into account the material properties and uses the initial geometry of the part. The output comes in the form of a two-dimensional map of residual stress normal to the cutting plane (Figure 3.11). The contour method offers good results for spatially varying residual stress fields that are difficult or slow to map using conventional point-wise measurement techniques, as is the case of welding residual stresses. Contour method measurements are typically performed on metallic parts, there are no specific size restrictions, but the measurement signal (displacement) scales with specimen size, and performing measurements on parts smaller than 5 mm by 5 mm in cross-section requires extreme precision. There are no restrictions on the shape of the specimen because the complex geometry is accounted for using a finite element model of the part [17, 106–109].

The size of the specimens are *250x250x58* extracted from Sample 1 and *600x400x58* extracted from Sample 2, shown in Figures 3.12 - 3.14; The samples were cut using WEDM perpendicular to the welds and thus allowing for the residual stresses present in the sample to relax and distort the four resulting pieces. During the cutting process of Sample 1, the wire broke, and the cut was restarted from the other side. In order to avoid this issue, for Sample 2, two 5 mm pilot holes were drilled and the remaining ligaments were sectioned afterward. The cutting of the specimens was performed at Iteum, in Santo Tirso, Portugal, on an ONA AF 35 machine (Figure 3.15) using a 250 µm diameter brass wire at a speed of approximately 1.3 mm/min for Specimen 1 and at Tornitrofa, in Trofa, Portugal, for Specimen 2. The resulting parts were then shipped to CATIM,

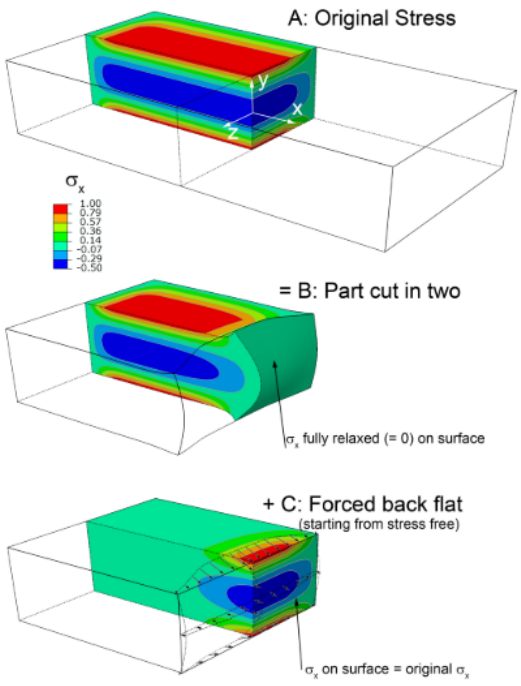



Figure 3.11: Superposition principle for the contour method. Stresses are plotted on one quarter of the original body [106].

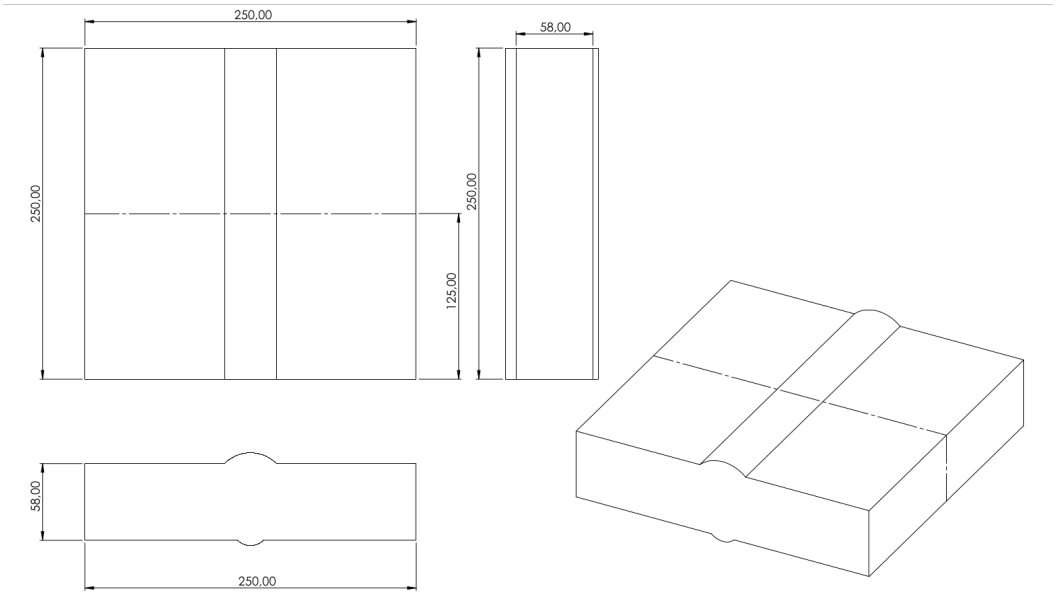



Figure 3.12: Specimen 1 extracted from Sample 1.

where the topography measurement was performed using a Zeiss UPMC Coordinate Measuring Machine (CMM) to map out the surface topography of the pieces after residual stress relaxation.

The resulting surface topographies were imported and averaged using Matlab and the surface

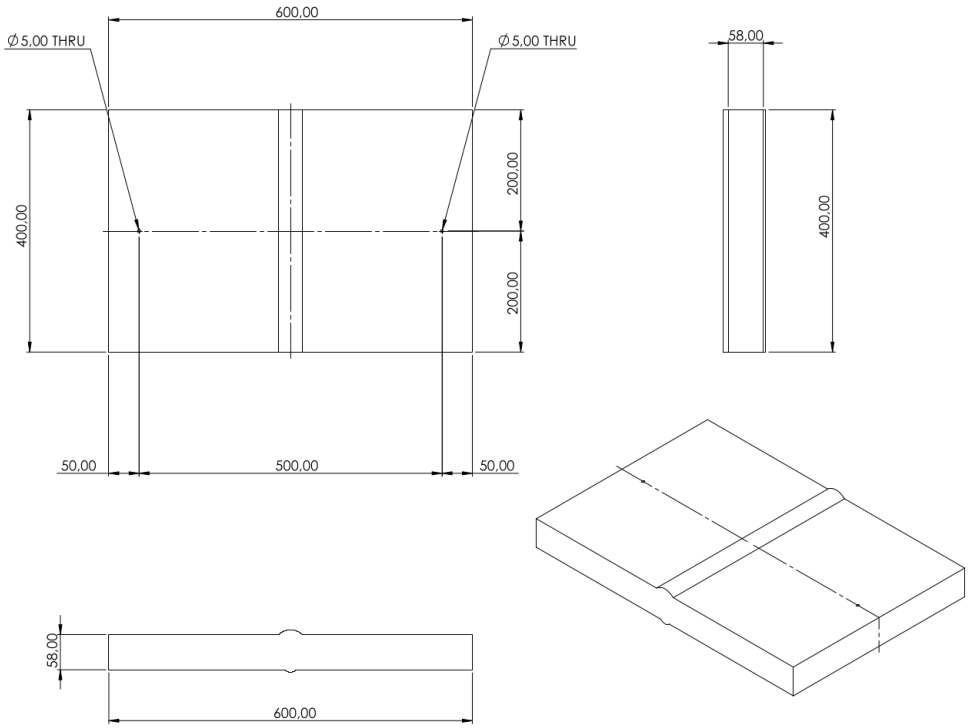



Figure 3.13: Specimen 2 extracted from Sample 2.



Figure 3.14: Specimen 1 from door cut-out prepared for EDM cutting.




Figure 3.15: ONA AF35 EDM machine at Iteum.

was applied as an initial nodal displacement to a FE elastic model of the part. The a mesh was composed of brick elements, and the calculations were performed using Abaqus. By doing this, the initial stress condition present in the pieces before cutting was obtained. Thus, by applying this procedure, the magnitude of residual stresses generated by the welding process can be obtained, evaluated, and compared.

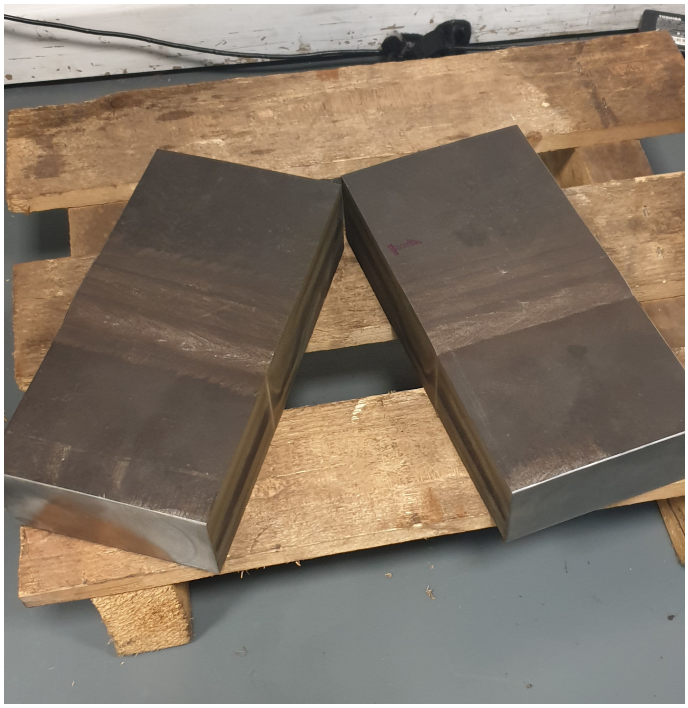


Figure 3.16: Specimen 1 after cutting.

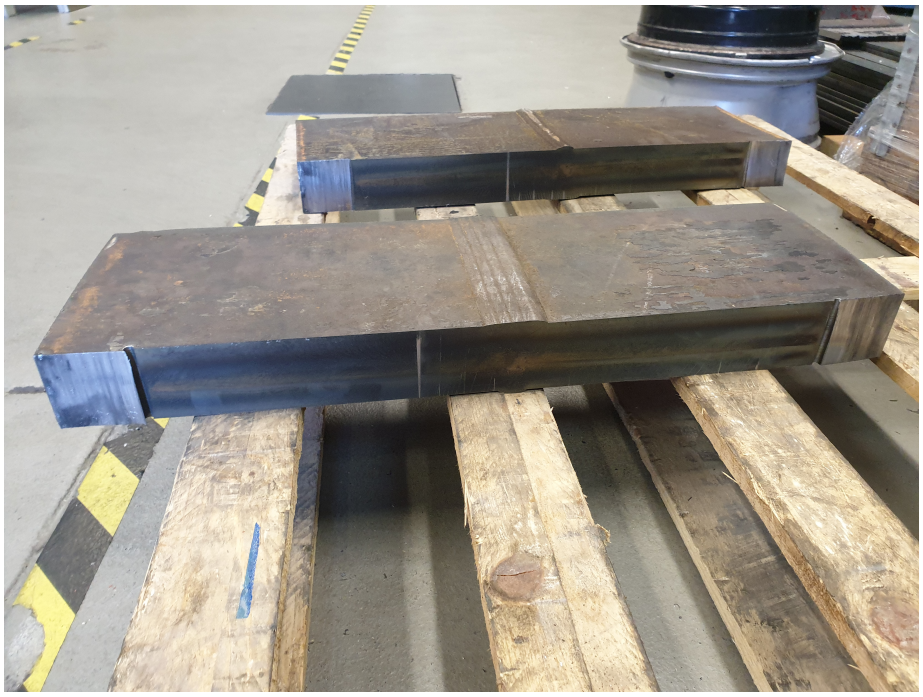


Figure 3.17: Specimen 2 after cutting.

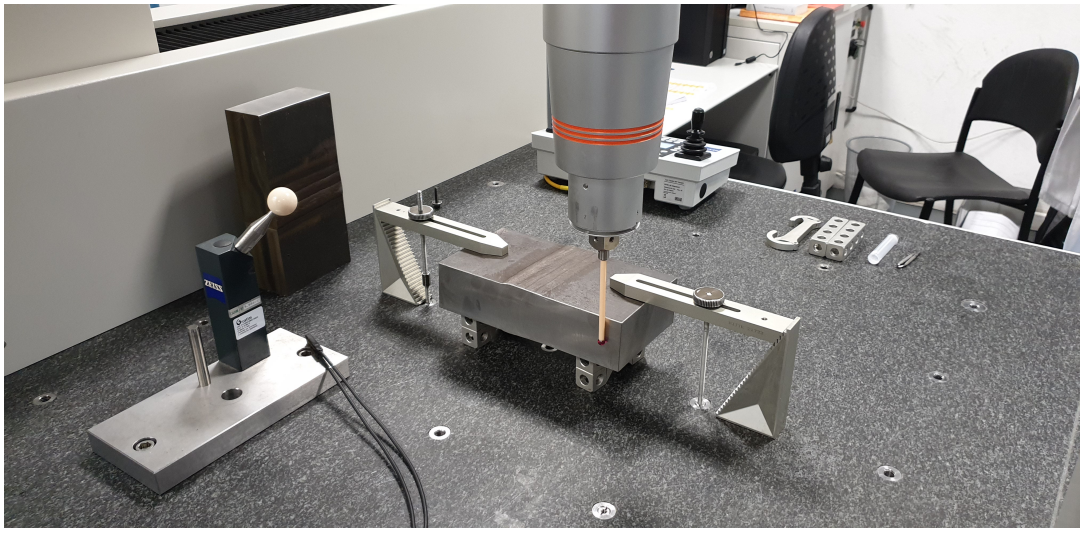


Figure 3.18: Specimen 1 during topography measurement at CATIM.

### 3.3.2 Microstructure and Macrostructure analysis and comparison

Metallographic testing is an important step that allows for the evaluation of the changes that occur in the microstructure of the material due to the welding process. The microstructural changes affect fatigue strength, toughness, ductility, brittleness, and hardness among others. Microstructural analysis of welded specimens and base material was performed by standard metallography and the micro-structure was recorded by optical microscopy (OM). In order to analyze the microstructure of the weld and the welding effects on the material, the specimens need to undergo a specific procedure.

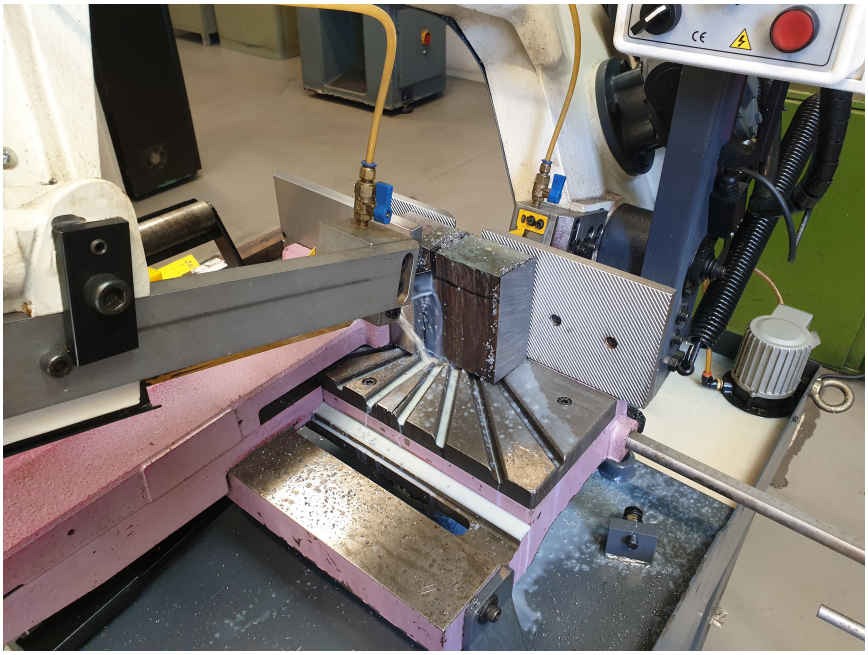


Figure 3.19: Specimen 1 during cutting.

Two welded specimens were obtained from both samples, sectioned perpendicularly to the weld, and reduced in size in order to ensure easier handling. Afterward, they underwent a polishing procedure. First, they were polished using *Buehler CarbiMet P80* grit sandpaper on a *Struers RotoPol-21* machine using water lubrication. Afterwards, using the same *Struers RotoPol-21* the grit of the sandpaper was reduced to *P180*, *P320* and lastly *P800*. The second step consisted of polishing on different *Struers* rotary polishing units utilizing a soft pad with aluminum oxide and water until the surface marks from the previous step were removed altogether and the surfaces were mirror-like in appearance. The last step was to use microcrystalline diamond solution first of




Figure 3.20: Struers RotoPol-21.

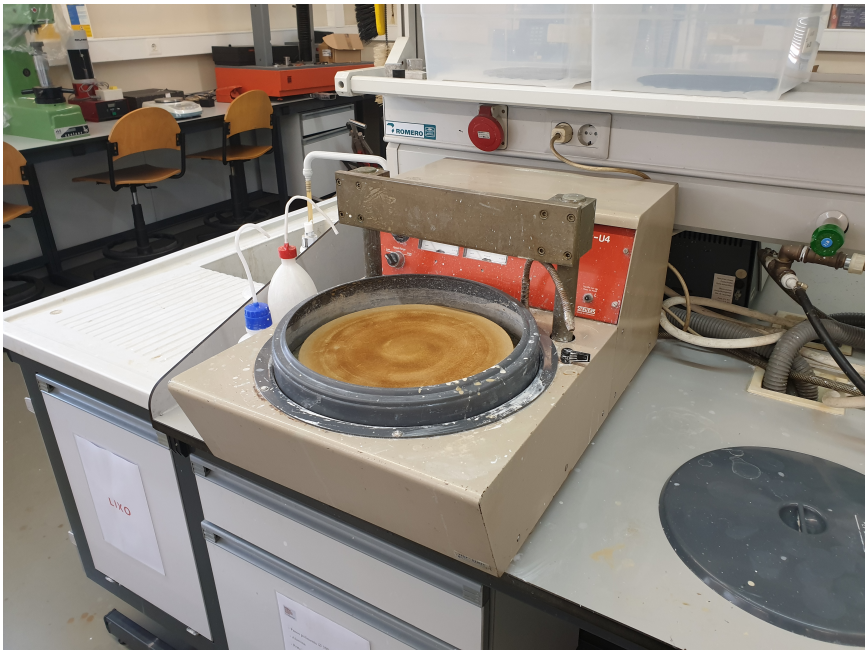



Figure 3.21: Second Struers rotary polishing unit.

6 microns and then 1 micron on a *Struers Rotopol-21* with soft pads and lubricant. The resulting surfaces can be seen in Figures 3.22 and 3.23.

After the grinding and polishing the surfaces were chemically etched using 2% Nital Solution (ethanol $C_2H_5OH$ + nitric acid $HNO_3$) for 60 seconds at room temperature and then cleaned with

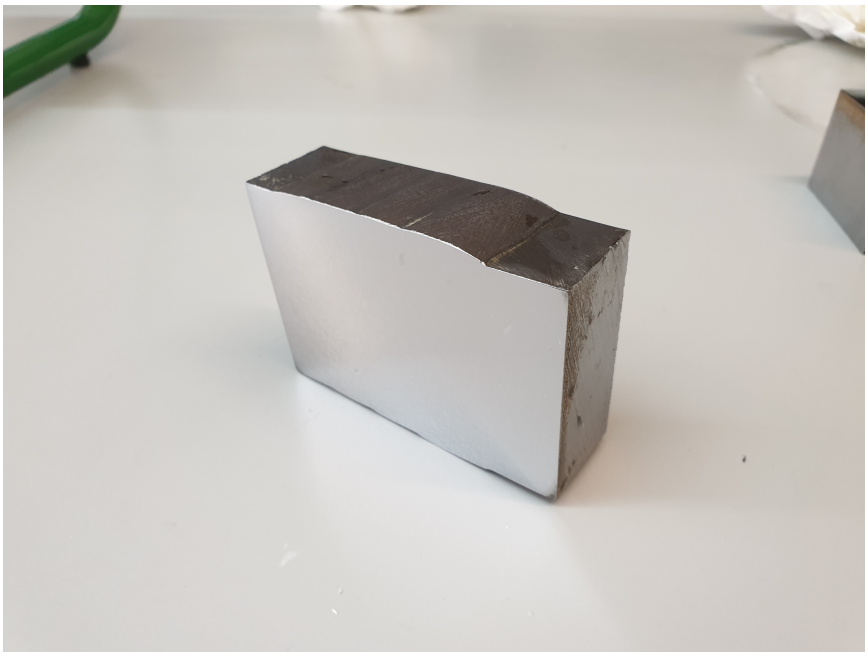


Figure 3.22: Specimen 1 after polishing.



Figure 3.23: Specimen 2 after polishing.

96% ethanol solution. To observe the microstructure a Zeiss Axiophot optical microscope (Figure 3.24) connected to a video camera was utilized to capture the required images. The locations that were observed are shown in Figures 3.25 and 3.26.

Further testing involved using the same specimens that were again chemically etched using

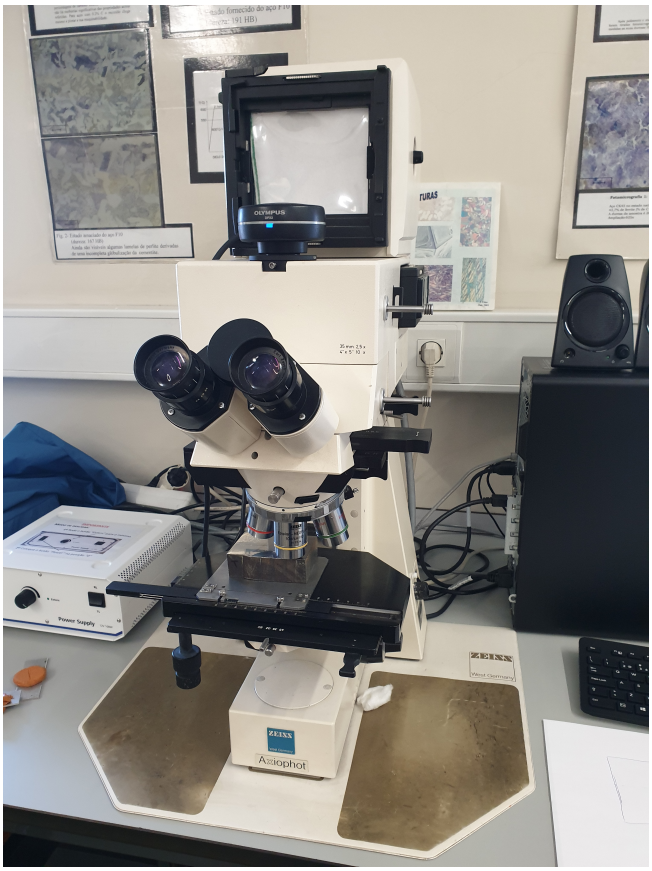



Figure 3.24: Zeiss Axiophot optical microscope

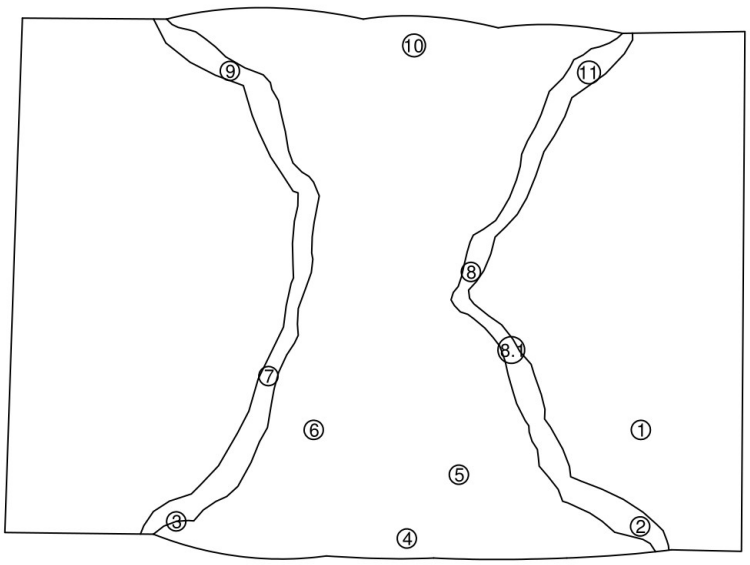



Figure 3.25: Specimen 1 numbered locations.

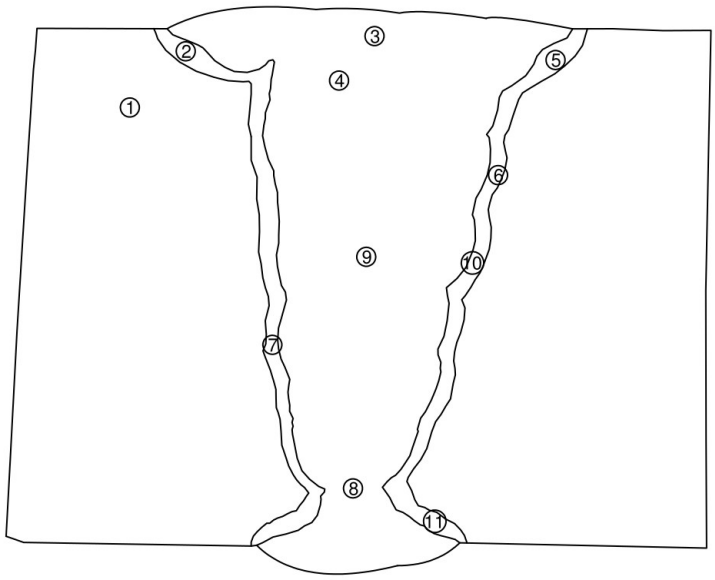



Figure 3.26: Specimen 2 numbered locations.

5% Nital solution for 180 seconds and a further etching step using SuperPicral (4% picric acid $(O_2N)_3C_6H_2OH$ and a few drops of hydrochloric acid HCl in ethanol solution) for approximately 5 minutes and again cleaned with 96% ethanol solution. This second chemical etching was performed to obtain the macrostructure and reveal the individual weld passes and the HAZ.

### 3.3.3 Hardness test

The Vickers hardness test was developed by Robert L. Smith and George E. Sandland, which were employees of Vickers Ltd. in 1921, as an alternative to the Brinell method. The basic principle of the method is that it measures the material's plastic deformation capabilities. A diamond indenter in the shape of a square-based pyramid is pressed against the material surface with a known load and the diagonals of the indentations are measured (Figure 3.27). This method can be used for a wide range of metals. The unit used to express the hardness of the material is Vickers Pyramid Number (HV).

After the microstructure and macrostructure images were captured, a Vickers Hardness test was performed using an *Wolpert-Werke Dia Testor 2 Rc* universal hardness testing machine (Figure 3.28) with a pyramid diamond tip and 10 kg weight with a loading time of approximately 20 s. Two line indentations were done at a distance of 10 mm from the top and bottom of the specimen

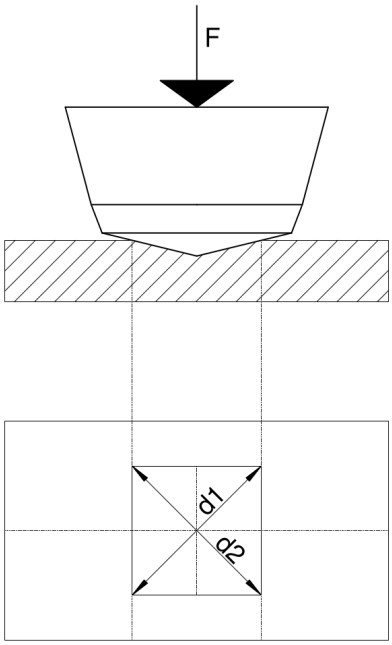



Figure 3.27: Vickers test principle.

transversely to the weld with an additional line passing in the root of the weld and a longitudinal line in the center of the weld. The distance between indentation points is 2 mm. Extra indentations were performed in the HAZ of both specimens at random locations. The locations are shown in Figures 3.29 and 3.30.



Figure 3.28: Wolpert Dia testor 2 RC.

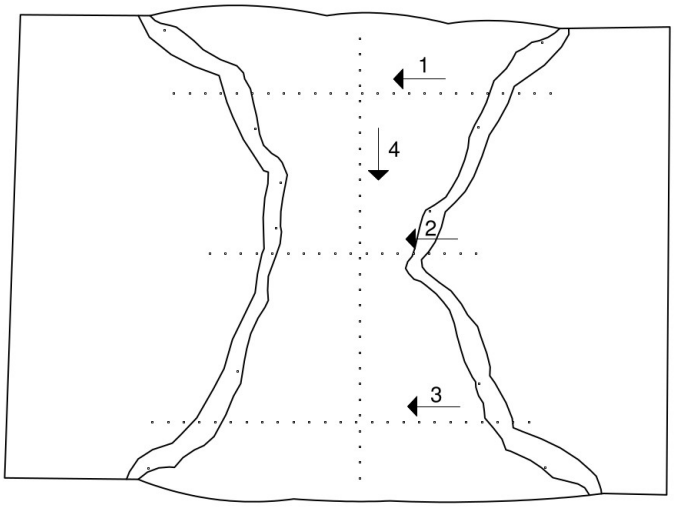



Figure 3.29: Specimen 1 Hardness measurement points.

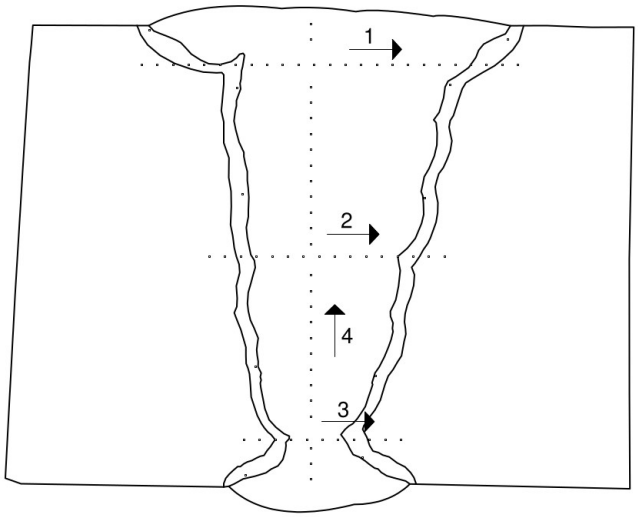



Figure 3.30: Specimen 2 Hardness measurement points.

### 3.3.4 Charpy Impact test

The Charpy impact test, also known as the Charpy V-notch test, is a standardized high strain-rate test that determines the amount of energy absorbed by a material during fracture. This absorbed energy is a measure of a given material's notch toughness and acts as a tool to study temperature-

Table 3.10: Charpy specimen type and and location.

| Specimen type | Location | No. of specimens |
|---|---|---|
| A | 1 | 6 |
| | 2 | 6 |
| | 3 | 6 |
| | 4 | 6 |
| B | 1 | 3 |
| | 2 | 3 |
| | 3 | 3 |
| | 4 | 3 |

dependent ductile-brittle transition. It is widely applied in the industry since it is easy to prepare and conduct and results can be obtained quickly and cheaply. The Charpy test has been chosen in the case of fusion welded materials because usually, the welding process has an influence on the impact toughness. V-notch specimens were obtained from the welded samples in accordance with ISO 15614-1:2017, EN ISO 9016:2012, and EN ISO 148-1:2016. A total of thirty-six specimens were obtained, the locations and numbers are shown in Figures 3.31 and 3.32 and Table 3.10.

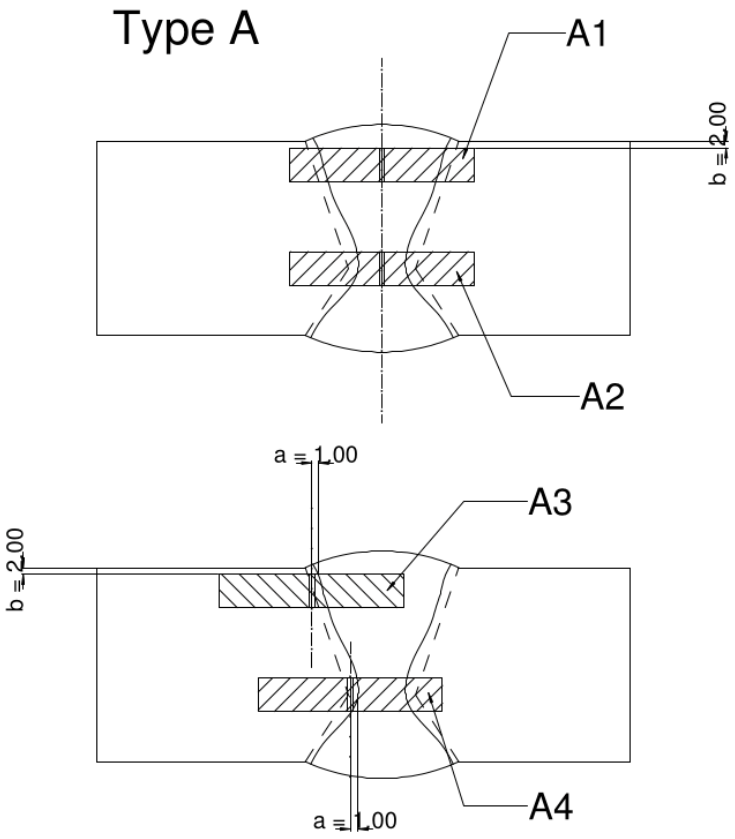



Figure 3.31: Sample 1 Charpy specimen locations.

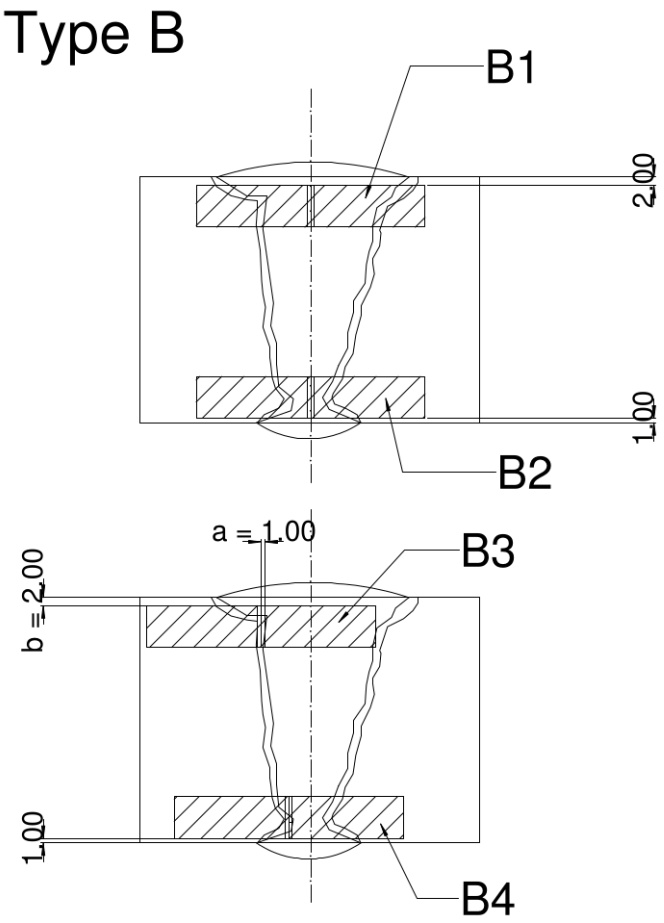



Figure 3.32: Sample 2 Charpy specimen locations.

The size of the specimens is *55x10x10 mm* with a V notch of 45° and 2 mm depth at the centre of one of the faces. The specimens are equivalent to the ISO 9016 designations, type A1/B1 to VWT (V: Charpy V-notch – W: notch in weld metal – T: notch through the thickness) and type A3/B3 to VHT (V: Charpy V-notch – H: notch in heat affected zone – T: notch through the thickness). Extra specimens were taken from the root of the welds, both for the weld metal and heat affected zone because of the specimen thickness, t > 50 mm. The Charpy pendulum used was a *Ametek/Riehle PI-2* impact testing machine that has a maximum striking energy of 325 J, with a striker radius of 8 mm, the striker weight is approximately 27 kg and the height of the drop is 122 cm (Figure 3.33a).

The tests were performed at a temperature of -20°C (± 2°C) for both sets of specimens in order to have a valid comparison. The specimens were cooled via a gaseous medium with pressurized liquid nitrogen (LN2). The specimens were placed on the anvil, covered while cooling and the




(a) Impact testing machine. (b) LN2 container.

Figure 3.33: Impact testing setup with the cooling device.

temperature was measured with a K-type thermocouple connected to a multi-meter. After reaching the desired temperature, the specimens were maintained for 30 minutes at this temperature. Besides these tests, an additional set of A-type specimens were produced and tested at lowered temperatures in order to obtain the Energy absorbed/Temperature (KV/T) curve.

### 3.3.5 Geometry Acquisition and 3D Modelling of a Wind Tower using a 3D Laser Scanning Technology

This work aims to acquire the interior geometry of a wind towers section by means of a 3D Laser Scanning System (LSS), the developed setup consists of a camera and a circular laser module mounted on the welding robot's arm traveling through the tower at a constant velocity.

The deployed system assists in examining the tower's interior surface, making it possible to build up its 3D profile. By using the 3D LSS system developed by dr. Behzad Farahani and designed at LOME, comprising a Logitech QuickCam Pro 9000 camera and a circular laser mounted on a *20x20* $mm_2$ Bosch profile (1.00 m long), the geometry of a 9.0 m section produced at Tegopi

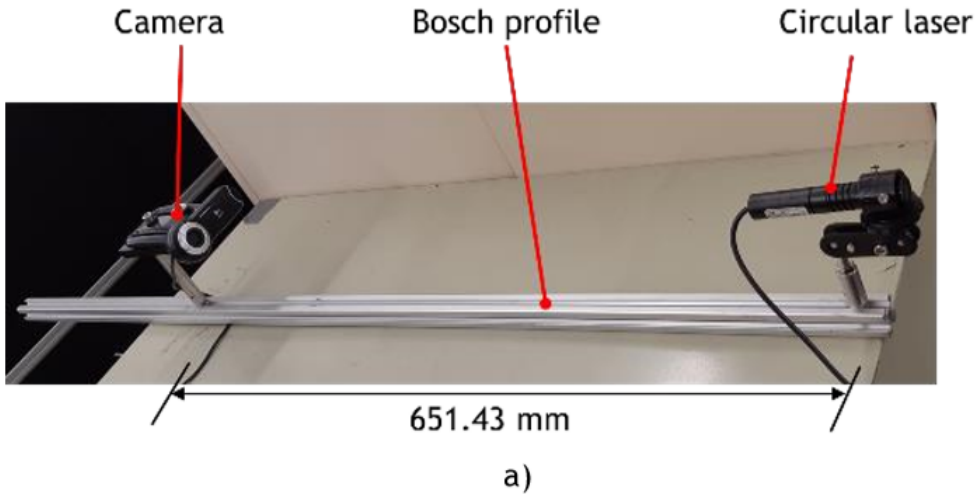



Figure 3.34: 3D LSS setup [110].

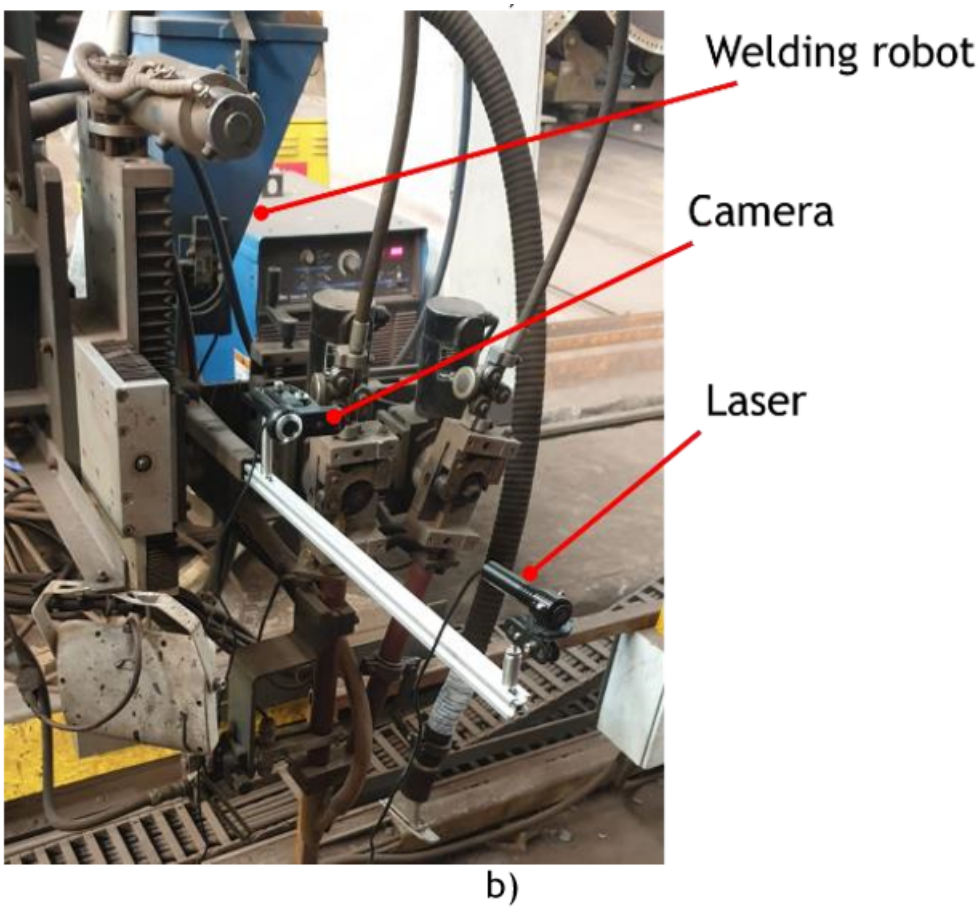



Figure 3.35: 3D LSS setup mounted [110].

was assessed. Only the 3.0 meter level region was measured due to the limitations of the system used to move the camera in the interior of the part.

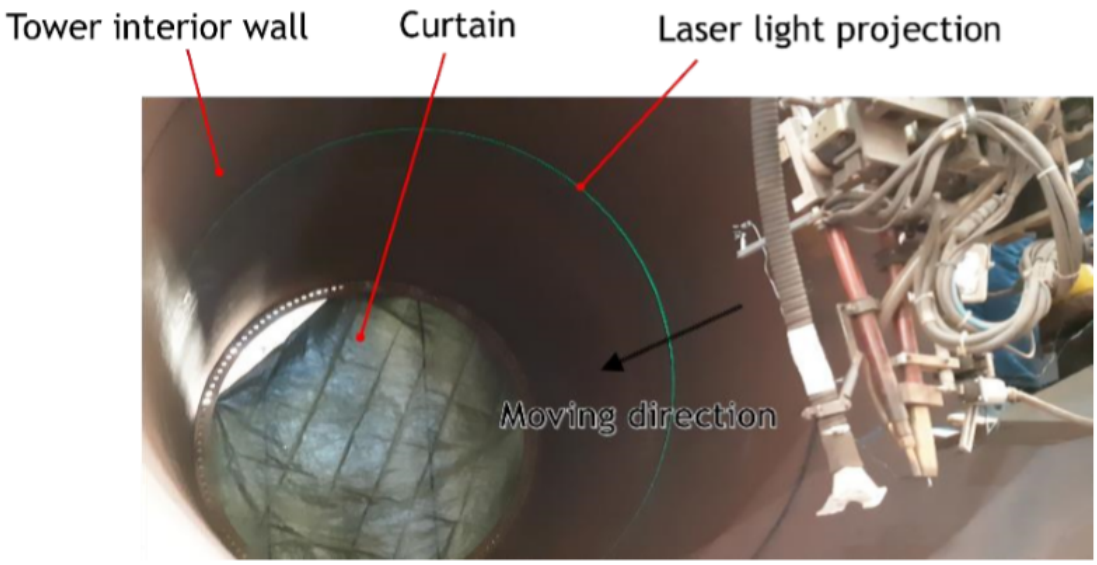



Figure 3.36: 3D LSS setup 2 [110].

The 3D LSS system was mounted at the end of the welding robot arm; the opposite end of the section was covered to prevent environmental light shine prior to the acquisition start-up. A *9x8* calibration pattern spaced at 80 mm was used to proceed with the calibration procedure. Because of the limited field-of-view of the camera, the acquisition was performed in two steps, the first part of the section was captured and after rotating it 180° by means of the rollers which were supporting the tower section, the second part was acquired. The traveling speed of the robot arm was 32 mm/s [110].

# Chapter 4

# Results and discussion

## 4.1 Introduction

This chapter presents the experimental results obtained, the effect that the welding process has on the residual stress state, and micro-structure, as well as revealing the number of weld passes and the heat-affected zone from the macro-structural analysis, hardness values, the energy impact absorption properties, and 3D LSS results. These serve as a basis for comparing the welding processes used for the two samples.

## 4.2 Residual Stress measurements

The topography measurements, using a CMM, were performed successfully for both samples, shown in Figures 4.1 and 4.2. The topographies are roughly similar, with the characteristic peak in the center of the weld. Although Sample 1 lacks the complete expected shape and is less steep, this can be explained by the overall smaller length and possible stress-relieving that might have occurred during specimen preparation.

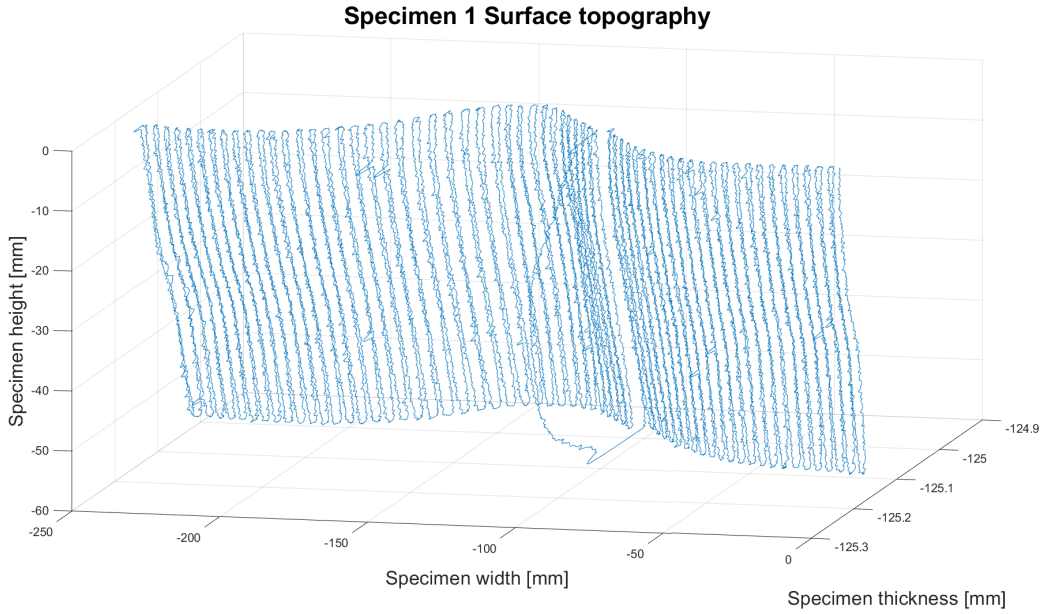



Figure 4.1: Sample 1 raw CMM measurements

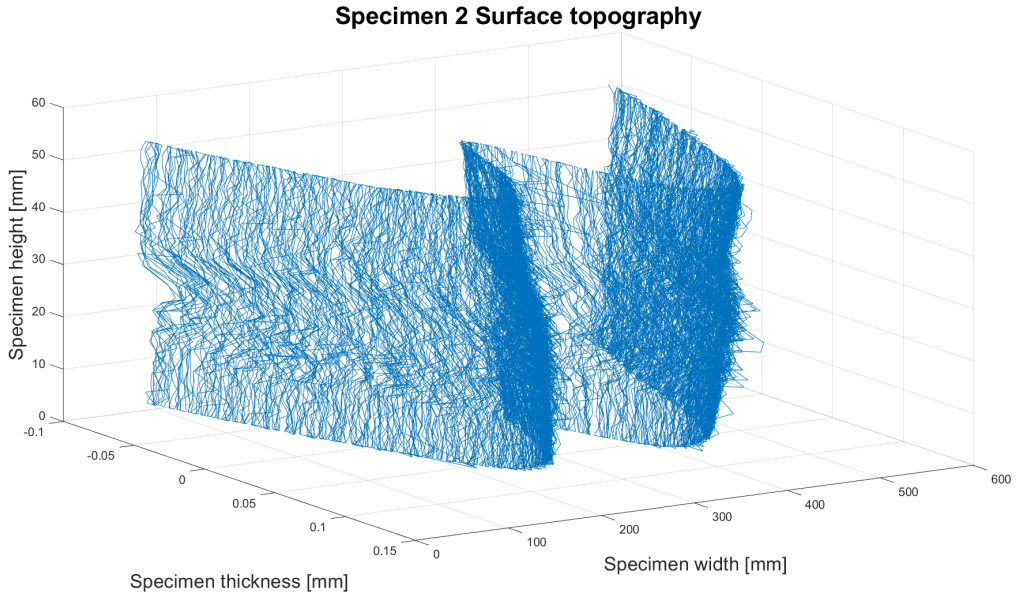



Figure 4.2: Sample 2 raw CMM measurements

The transverse residual stress was measured successfully in one of the two samples using the contour method, with results for the other sample having not been obtained yet, thus proving the viability of the proposed measurement method to obtain the residual stress map. The topography measurement yielded the expected results, in accordance with the literature. The two averaged surfaces of Sample 2 are shown in Figure 4.3 and the smoothed surface in Figure 4.4. The resulting residual stress fields are shown in Figures 4.5 and 4.6.

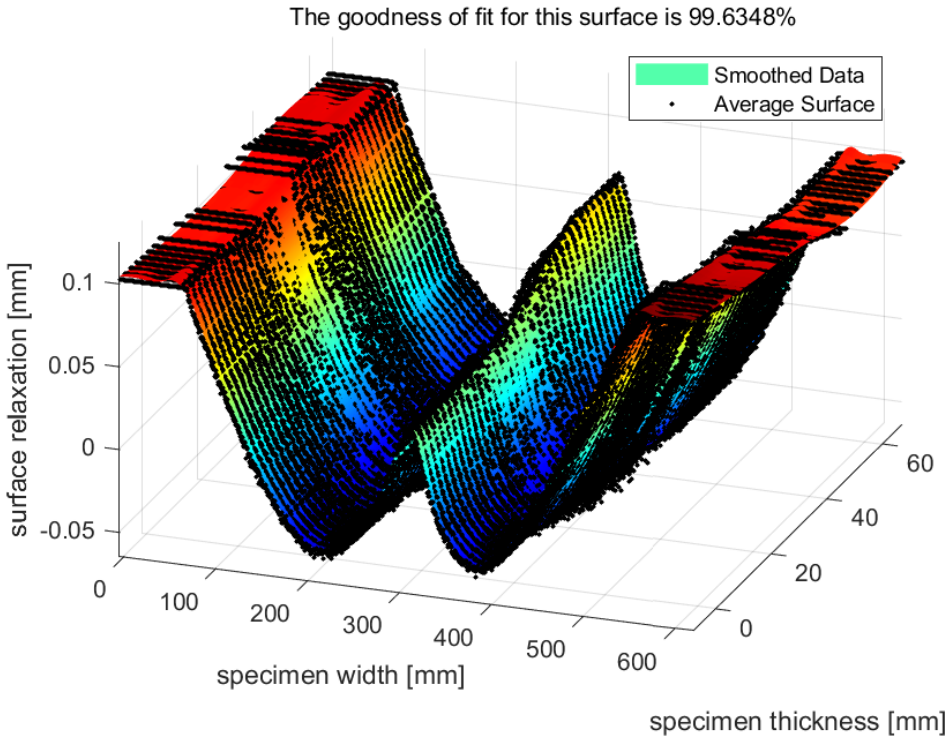



Figure 4.3: Averaged surfaces resulting from the averaged points for Sample 2.

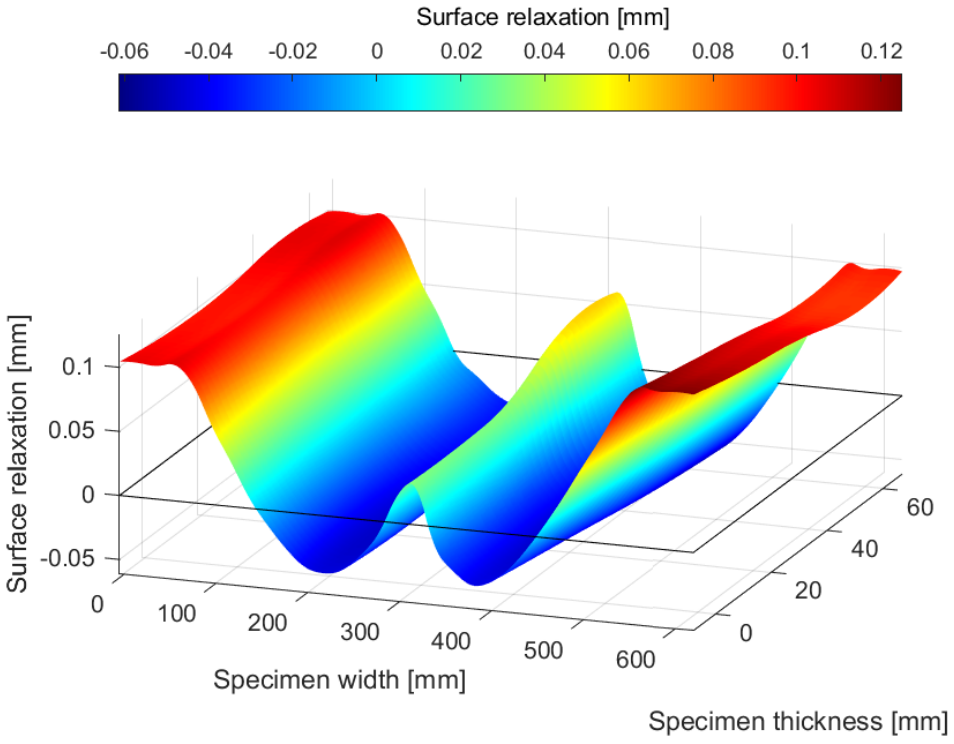



Figure 4.4: Resulting averaged smooth surface for Sample 2.

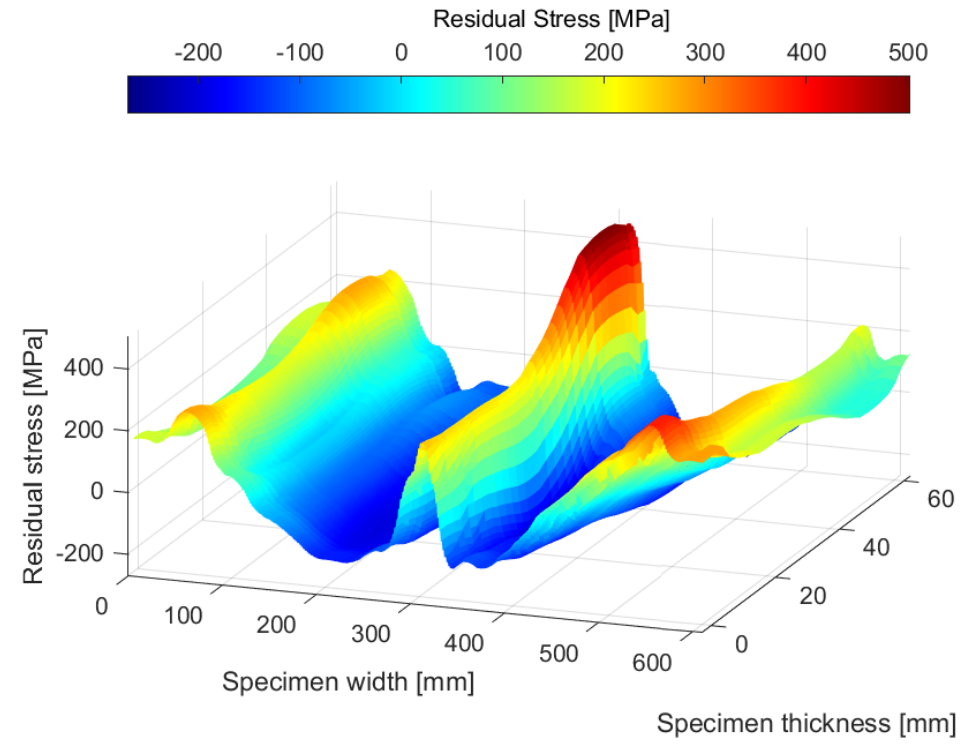



Figure 4.5: 3D residual stress profile for Sample 2.

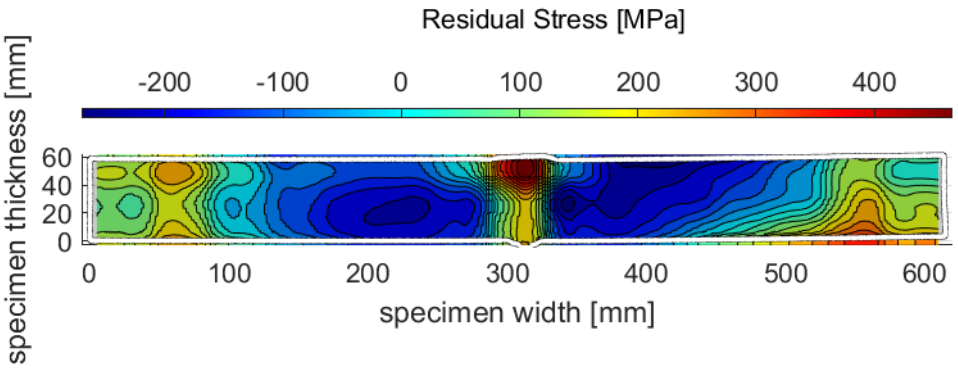



Figure 4.6: 2D residual stress profile for Sample 2.

The results are in accordance with the literature and the bevel geometry shown in Figure 4.8, where a larger number of weld beads were deposited at the top of the sample and the corresponding area has a concentration of residual stress.

## 4.3 Micro-structure and Macro-structure analysis

After undergoing two etching procedures that revealed the micro and macrostructure of the welded samples, the results are presented below. Figures 4.7 and 4.8 reveal the bevels geometries that were used as well as the number of passes. For *Specimen 1* the bevel is double-V with 30 identified passes, while for *Specimen 2* the bevel is single-U and 25 passes were identified. Because the thickness of the plates is the same, but fewer welding passes were utilized for Sample 2 the weld beads are larger, with less overlapping in comparison with Sample 1, where a larger number of passes allowed for smaller and wider weld beads that overlap frequently and have a tempering effect. The size of the HAZ is similar for both samples, except for the root area of the weld, where it is much smaller than Sample 1 and the grains appear to be more refined.

The specimen size is *83 x 59 x 27* [mm] for Specimen 1 and *78 x 58 x 41* [mm] for Specimen 2.

As for the micro-structural analysis (Figures 4.9 - 4.16), the identified structures are acicular ferrite and grain boundary ferrite in the WM, for the HAZ upper and lower bainite with aligned and non-aligned carbides, is present as well as pro-eutectoid ferrite and possible martensite, although the hardness values shown in Subchapter 4.4 support the claim that if martensite is present, it was not revealed during the testing and a low percentage is present.

The HAZ was revealed and shown in Figure 4.17. Because the thermal cycle is dependent on the heat input and distance from the fusion boundary, the areas closer to it will have harder micro-structures that will progressively soften while moving away from the fusion boundary. Near the fusion boundary, the coarse-grained super-critical area shows rapid austenite grain growth, typically occuring above 1000 ° C, while further away the fine-grained super-critical area does not reach similar temperatures, and thus does not produce the same effect. The inter-critical area of the HAZ is far enough from the fusion boundary to present only partial transformation to austenite and substantial grain refinement. The sub-critical HAZ is far enough from the fusion boundary to only show some pearlite spherodizing and little grain refinement. Sample 2 has a larger grain size in the HAZ and WM, especially noticeable in the CGSC zone of the HAZ. This fact is supported by the higher HV Hardness values for Sample 2, presented in Subchapter 4.4.



Figure 4.7: Macro-structure Specimen 1.

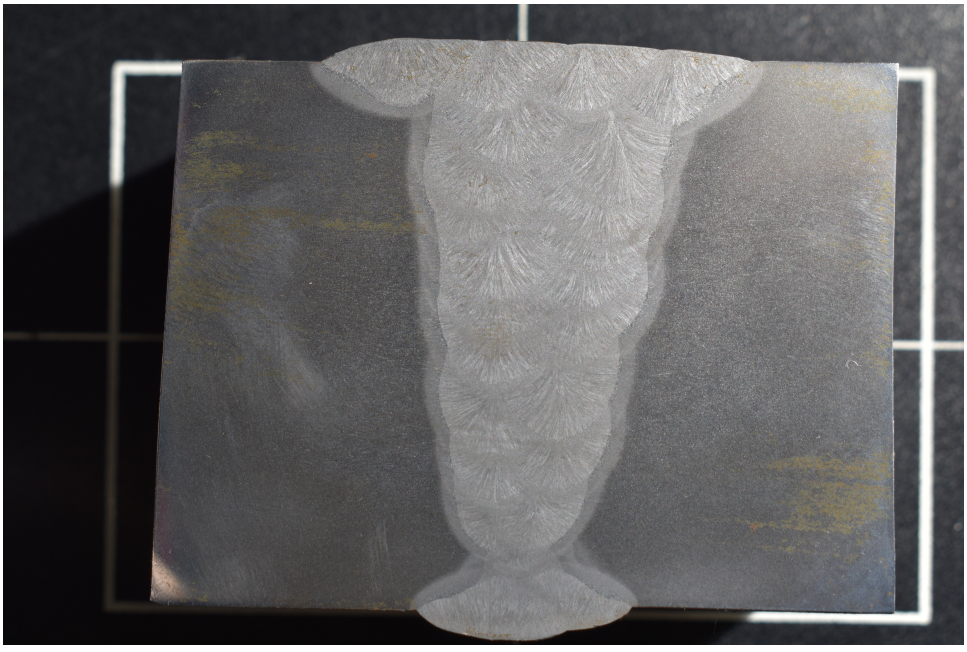


Figure 4.8: Macro-structure Specimen 2.

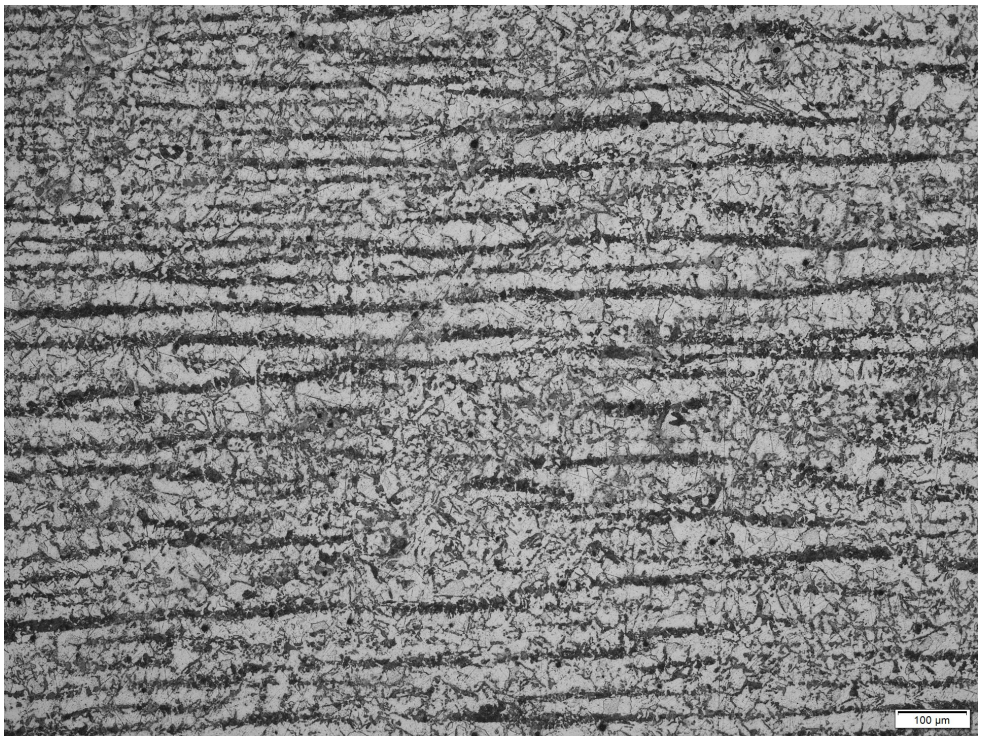



Figure 4.9: Base metal Specimen 1 Location 1 (magnification 10x, scale 100 µm).

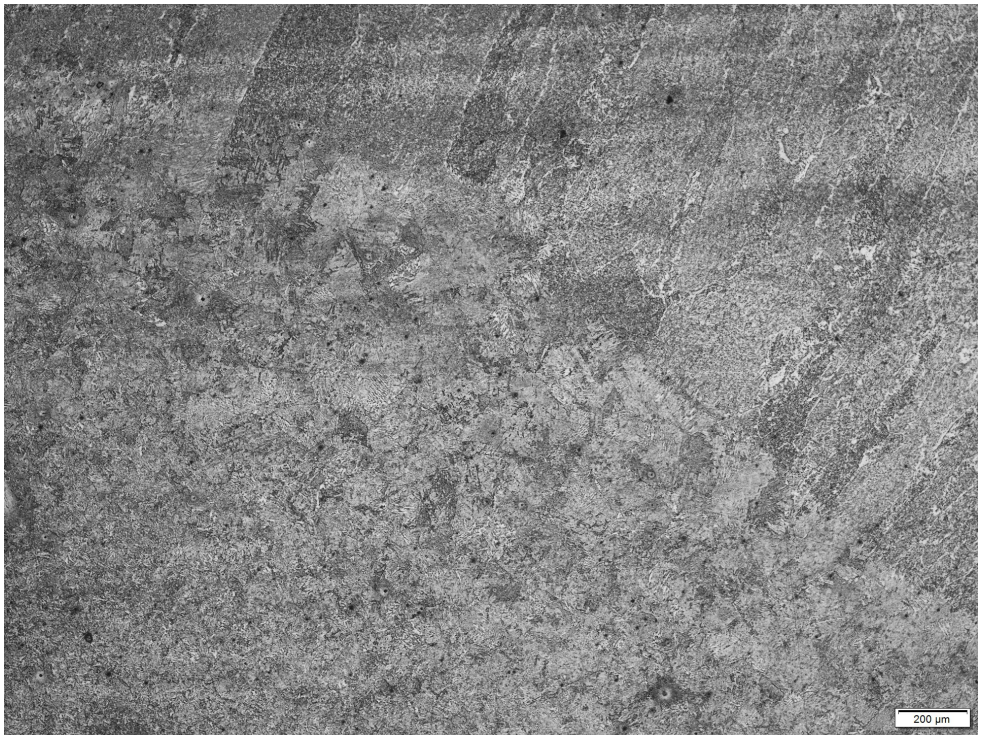



Figure 4.10: Transition zone between HAZ-Weld metal Specimen 1 Location 2 (magnification 5x, scale 200 µm).

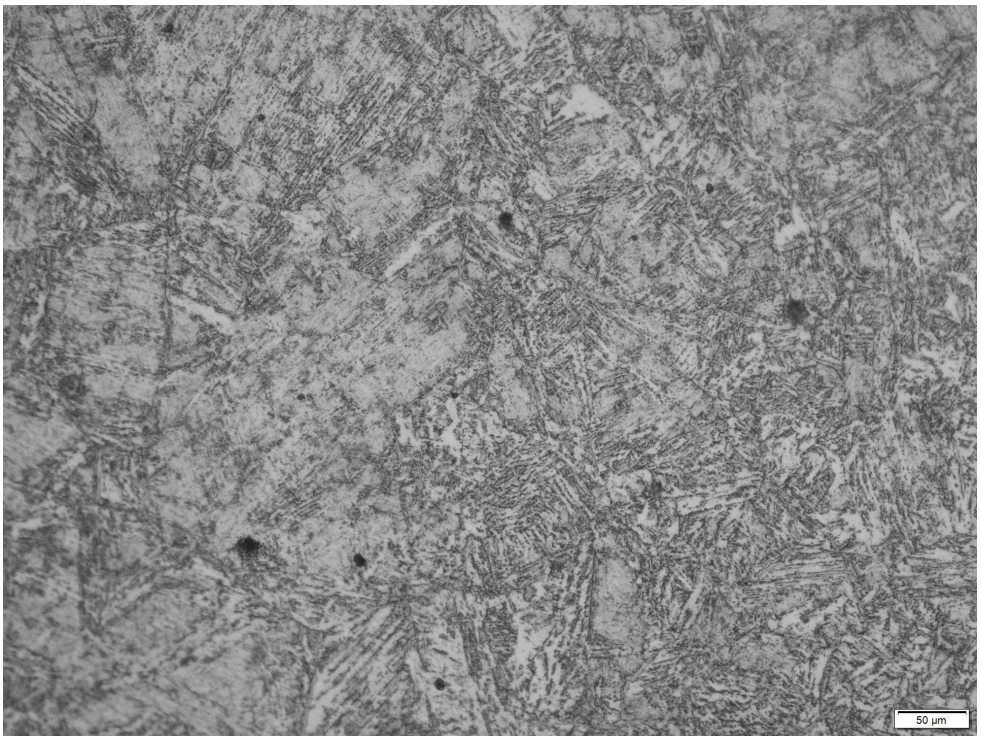



Figure 4.11: HAZ Specimen 1 Location 3 (magnification 50x, scale 50 µm).

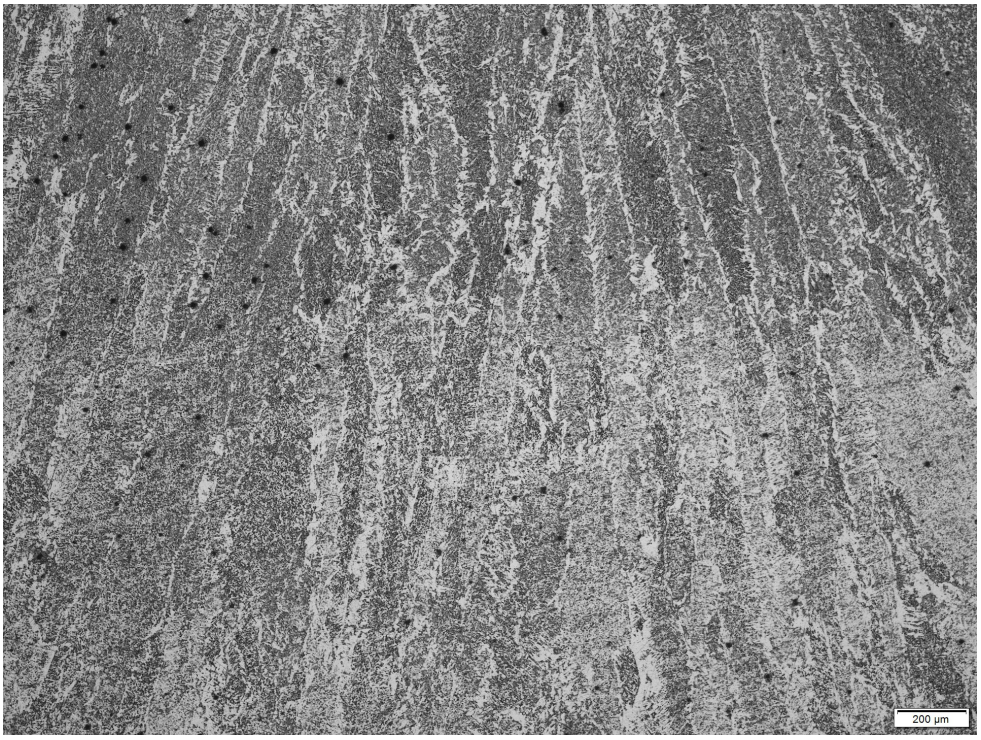



Figure 4.12: Weld metal Specimen 1 Location 5 (magnification 5x, scale 200 µm).

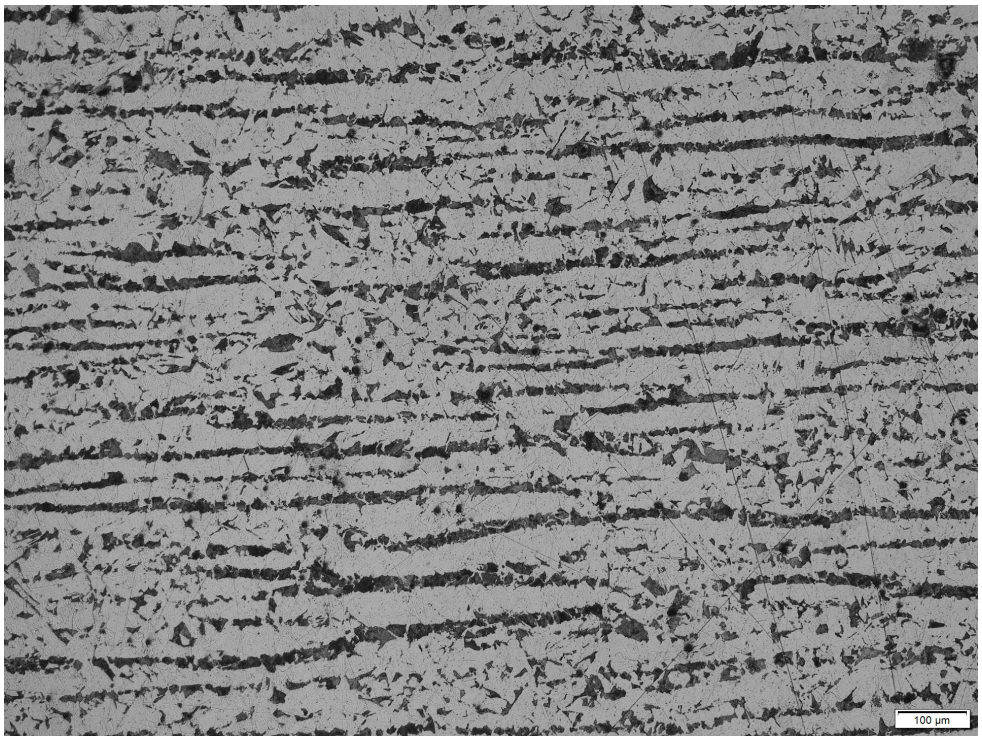



Figure 4.13: Base metal Specimen 2 Location 1 (magnification 10x, scale 100 µm).

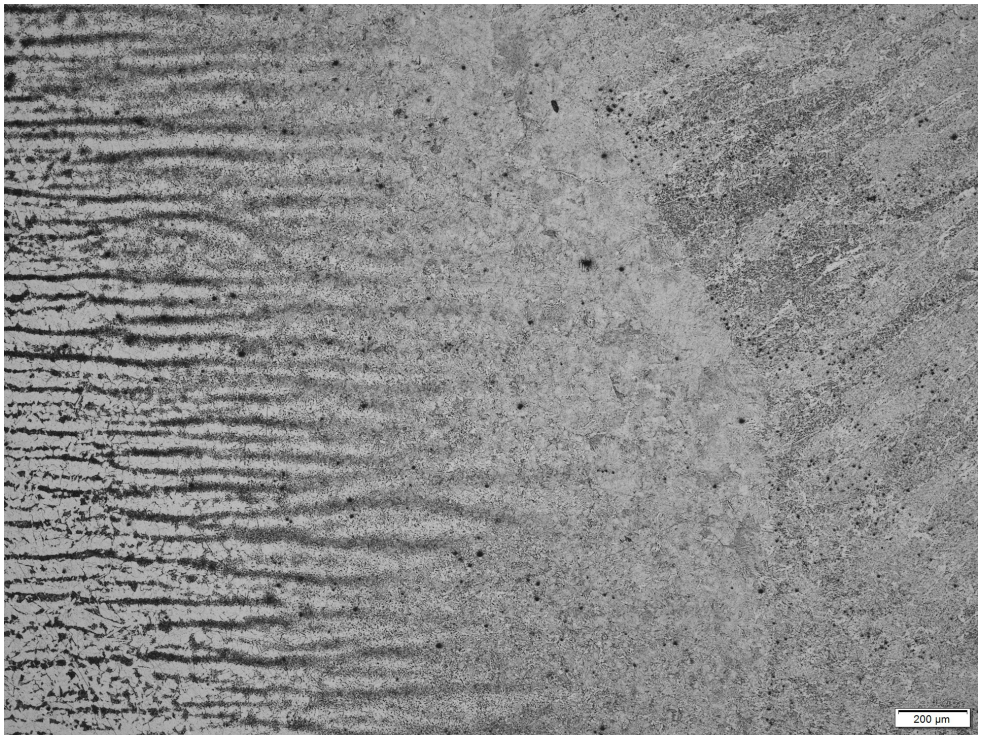



Figure 4.14: Transition zone between Base metal-HAZ-Weld metal Specimen 2 Location 7 (magnification 5x, scale 200 µm).

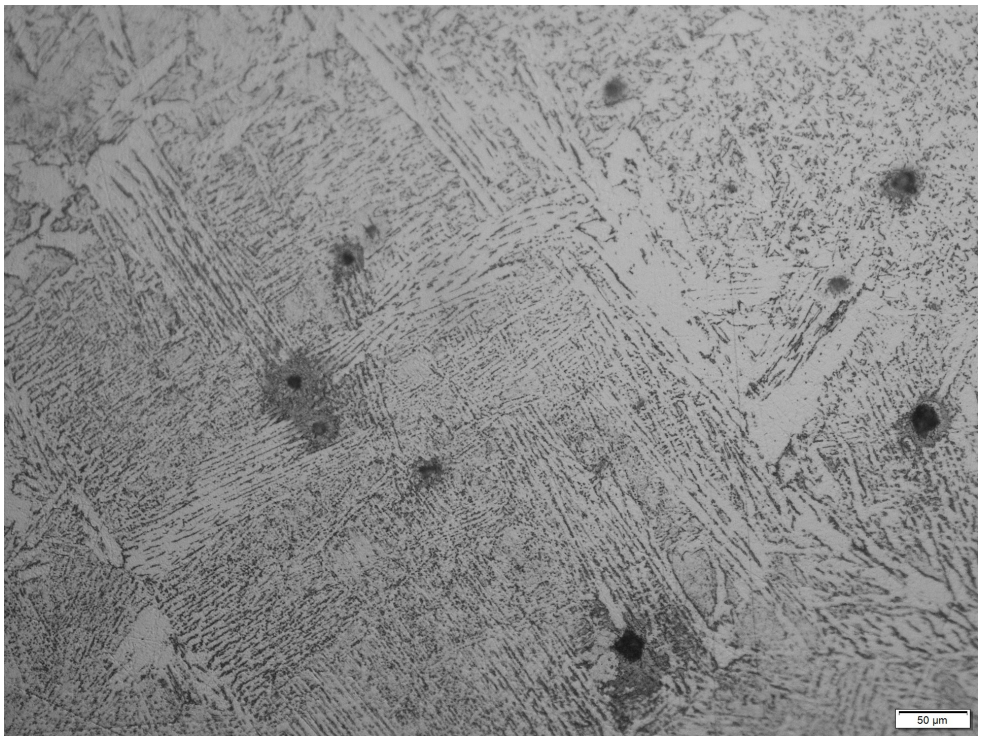



Figure 4.15: HAZ Specimen 2 Location 2 (magnification 50x, scale 50 µm).

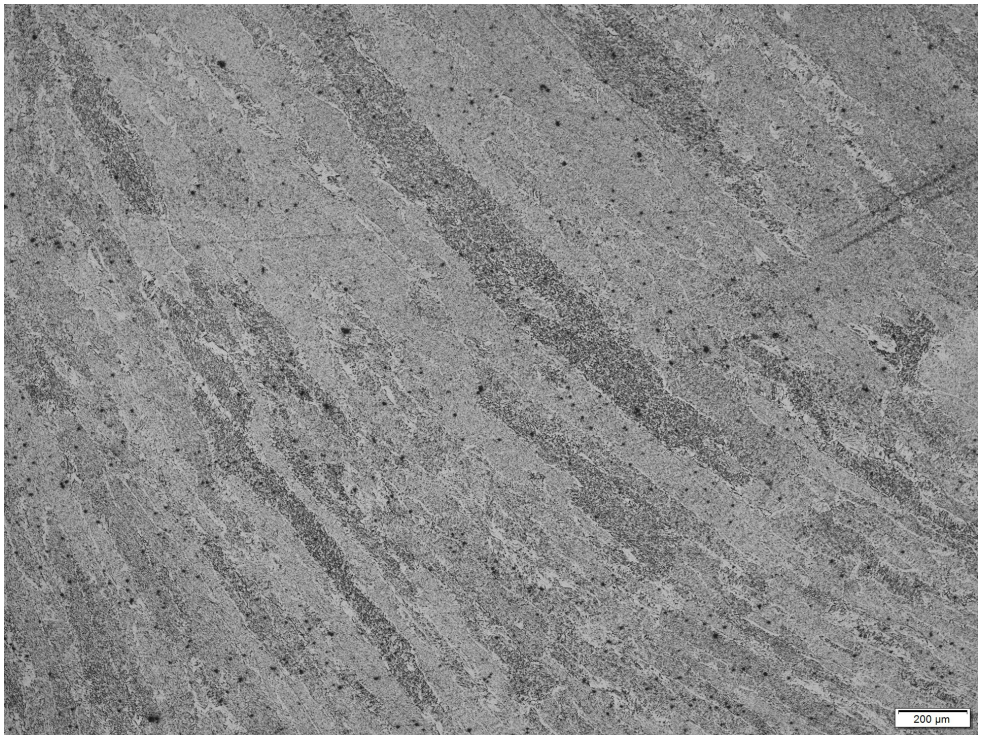



Figure 4.16: Weld metal Specimen 2 Location 3 (magnification 5x, scale 200 µm).

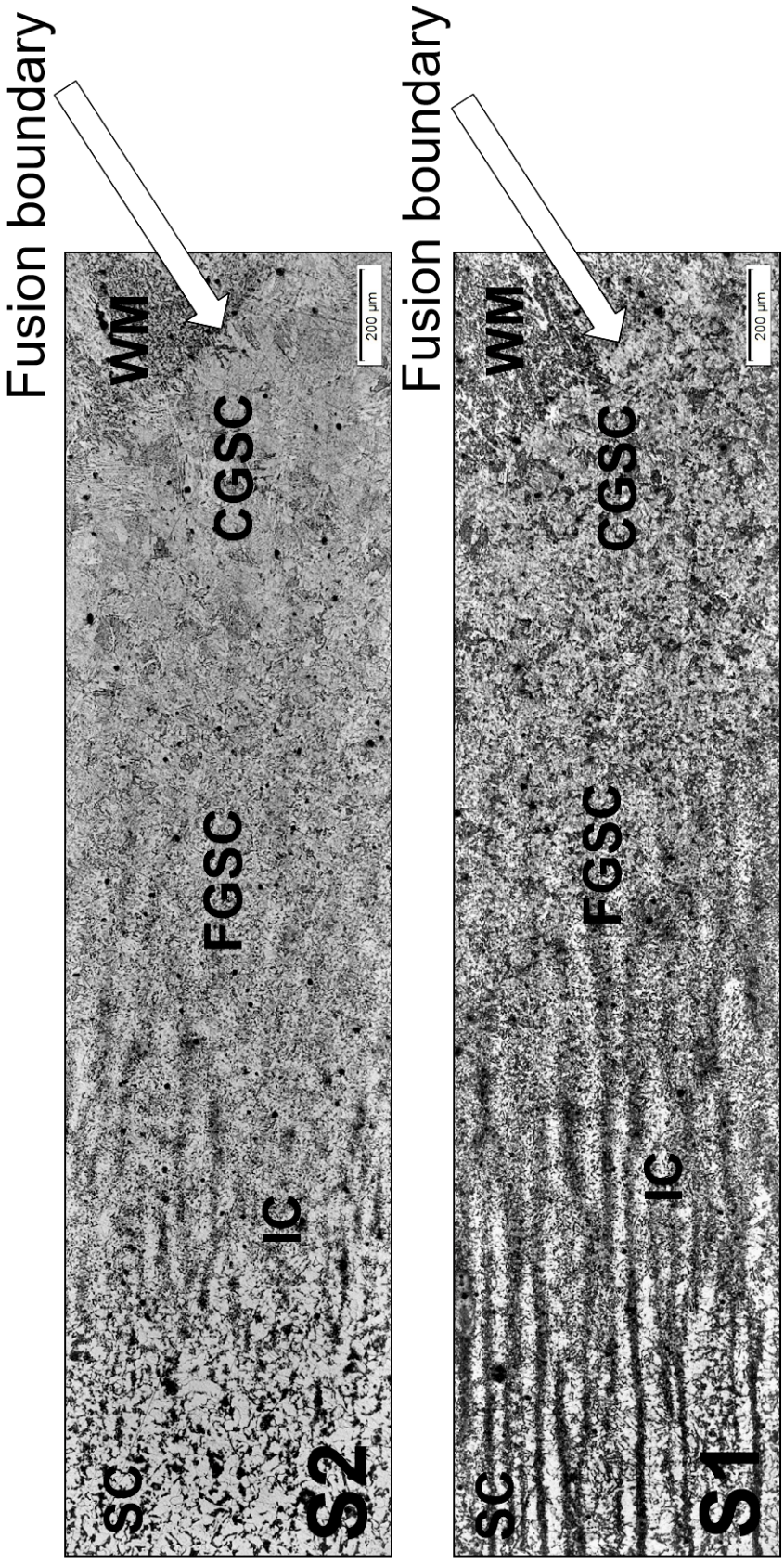



Figure 4.17: HAZ areas of both Specimens; Scale 200µm .

## 4.4 Hardness test

The locations of the Vickers Hardness measurements are shown in Figures 3.29 and 3.30, and the corresponding results for Sample 1 in Figures 4.18, 4.19, 4.20 and 4.21, and Sample 2 in Figures 4.22, 4.23, 4.24 and 4.25. The values obtained for both samples support the fact that the welds did not undergo rapid cooling as the values are not high enough to suggest a large presence of martensite.

The Vickers hardness values obtained are lower than expected but mostly in accordance with the literature. This points towards the fact that rapid cooling was partially avoided, and the successive passes may have re-heated the weld metal deposited in the previous pass and tempered it, thus resulting in a softer, more ductile microstructure. The typically expected profile is the one shown in Figure 4.19, with progressively lower values from HAZ to WM and BM respectively.

The values tend to be lower for Sample 1 in nearly all the locations except the HAZ, which can be a result of the increased number of weld passes and possible higher input used for Sample 2. Lower values were expected for the WM in both samples, but this can be due to the nature of the test itself, the indentations may have been done in a portion of the samples that have a harder micro-structure at the point of contact than the surrounding area. As for the values obtained for the HAZ of both specimens, they are indicative of the expected harder micro-structure, but the variations can be explained by the locations in which the indentations were made, the CGSC are will always present higher hardness values than the other areas of the HAZ due to its proximity to the heat source.

An extra set of HV hardness measurements were performed strictly for the HAZ of both specimens (Figures 4.26 and 4.27). They were performed in order to obtain a better understanding of the hardness of the HAZ that the initial measurements cannot offer since there are only a few indentations done in the HAZ in each of the lines. The measurements are consistent with the expected results and show higher values for the HAZ than the initial measurements. The values obtained from Sample 1 are slightly higher than those from Sample 2. A comparison of the line indentatntions is presented in Figure 4.28 and the 3D profiles in Figures 4.29 and 4.30.

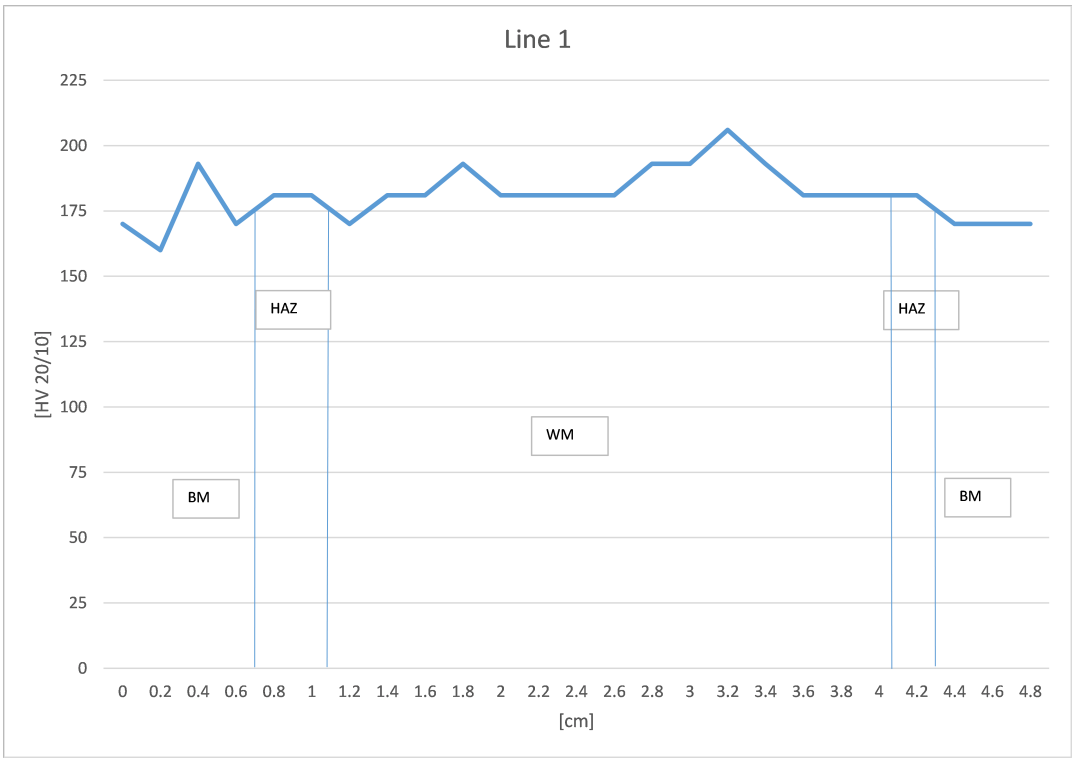



Figure 4.18: HV values Sample 1 Line 1.

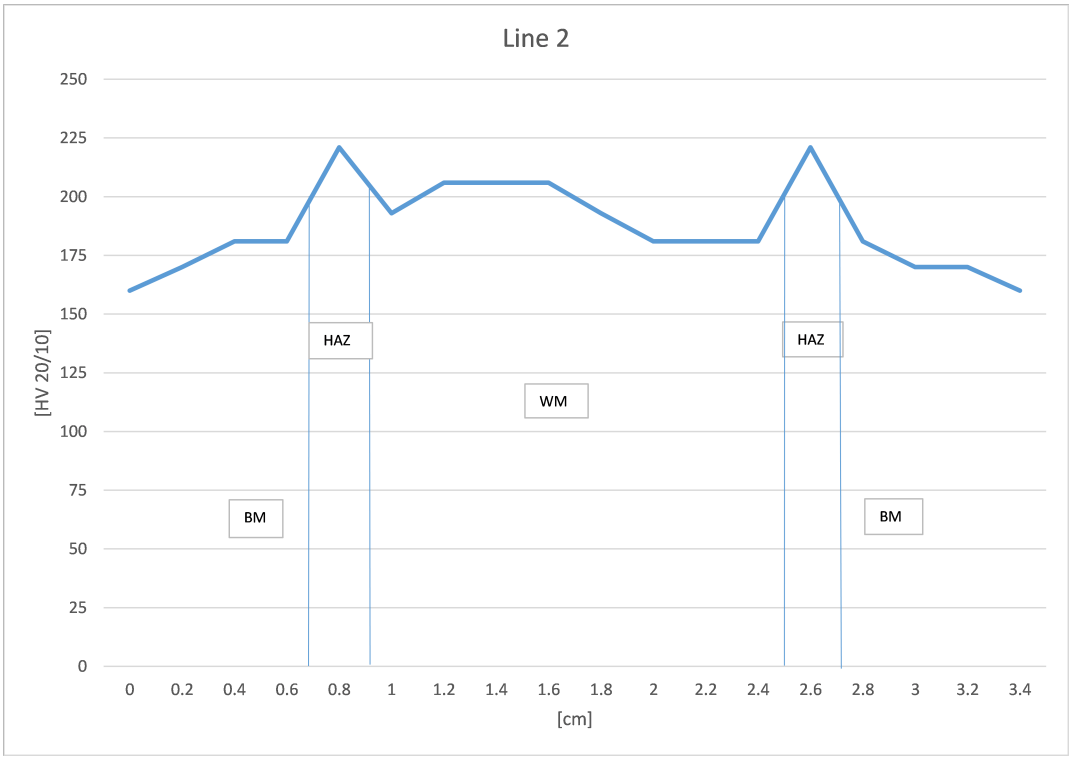



Figure 4.19: HV values Sample 1 Line 2.

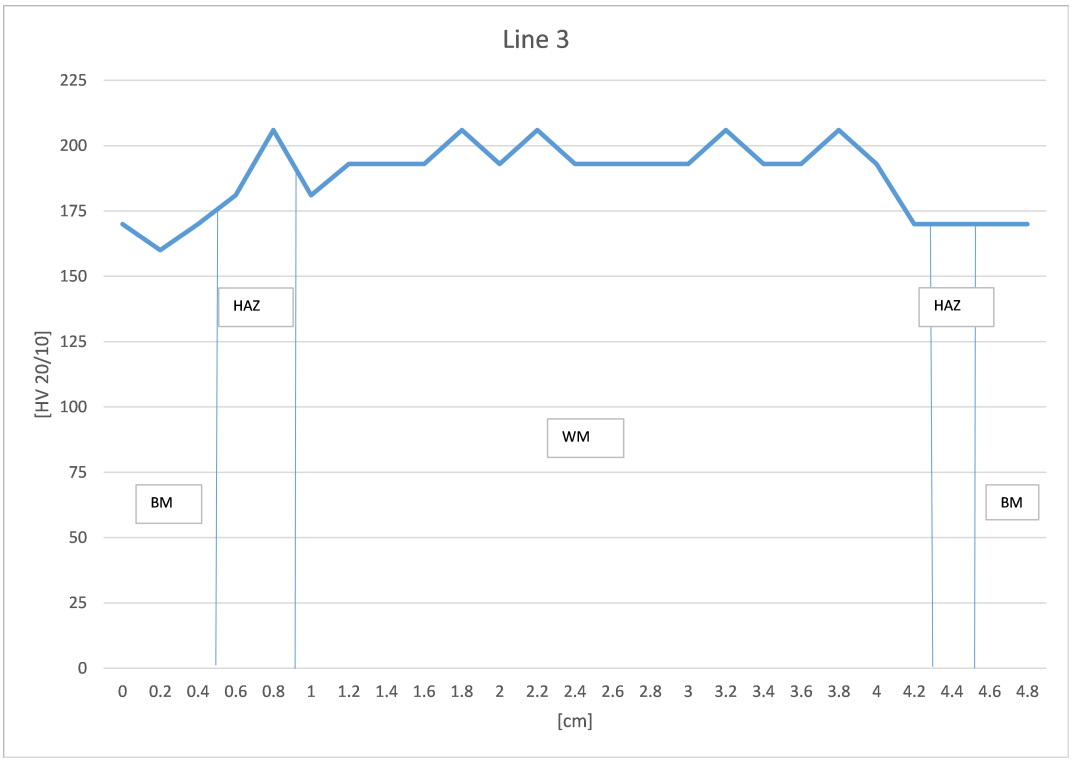



Figure 4.20: HV values Sample 1 Line 3.

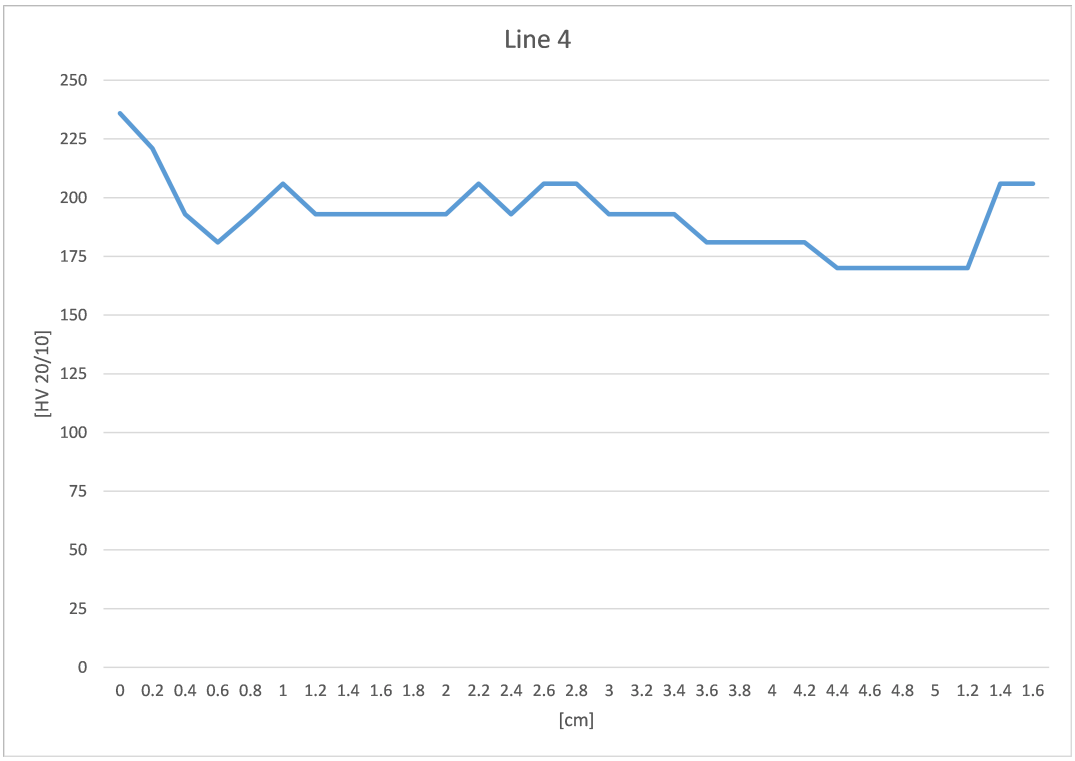



Figure 4.21: HV values Sample 1 Line 4.

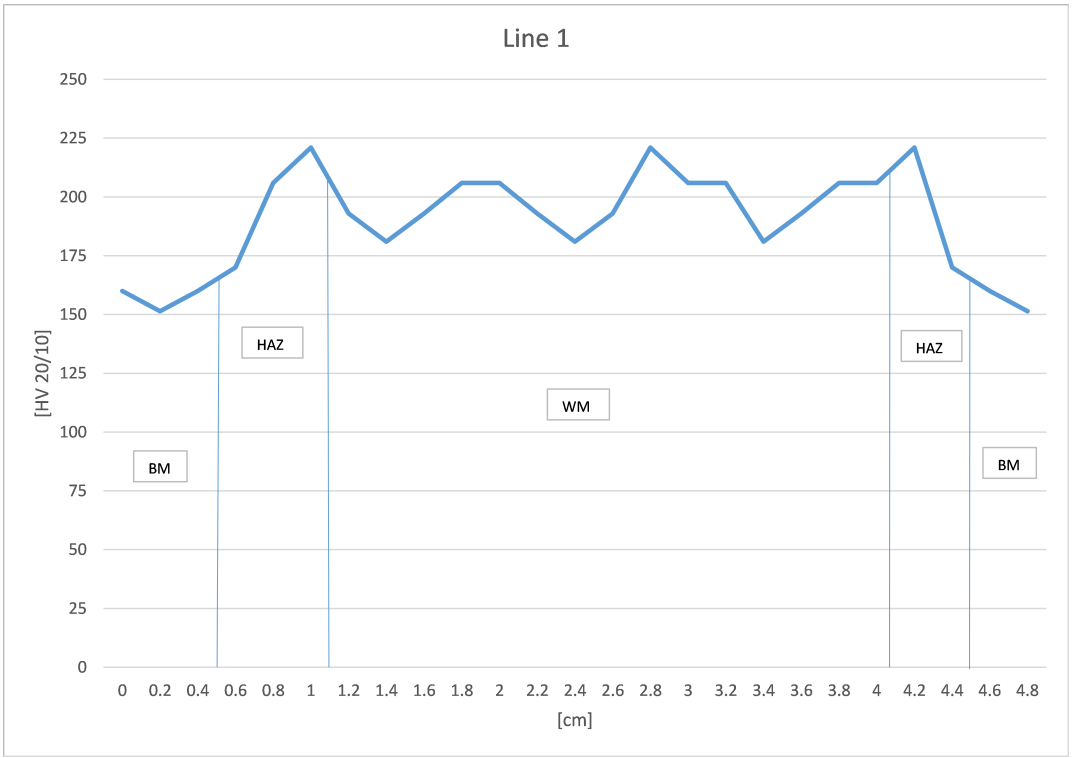



Figure 4.22: HV values Sample 2 Line 1.

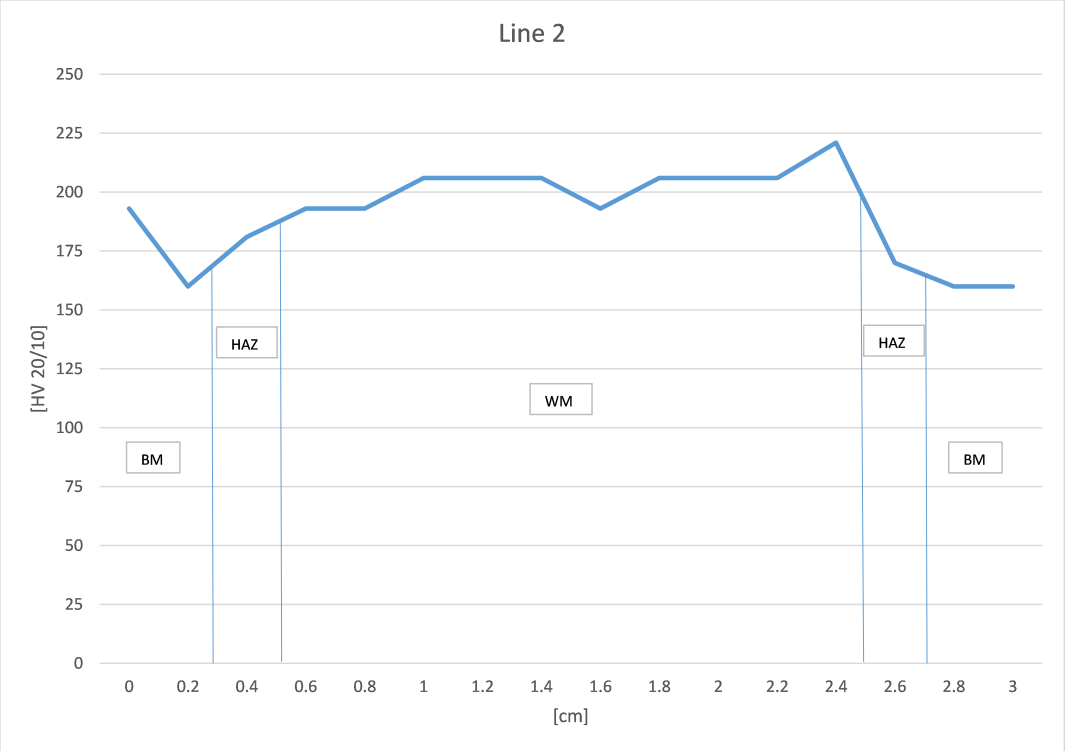



Figure 4.23: HV values Sample 2 Line 2.

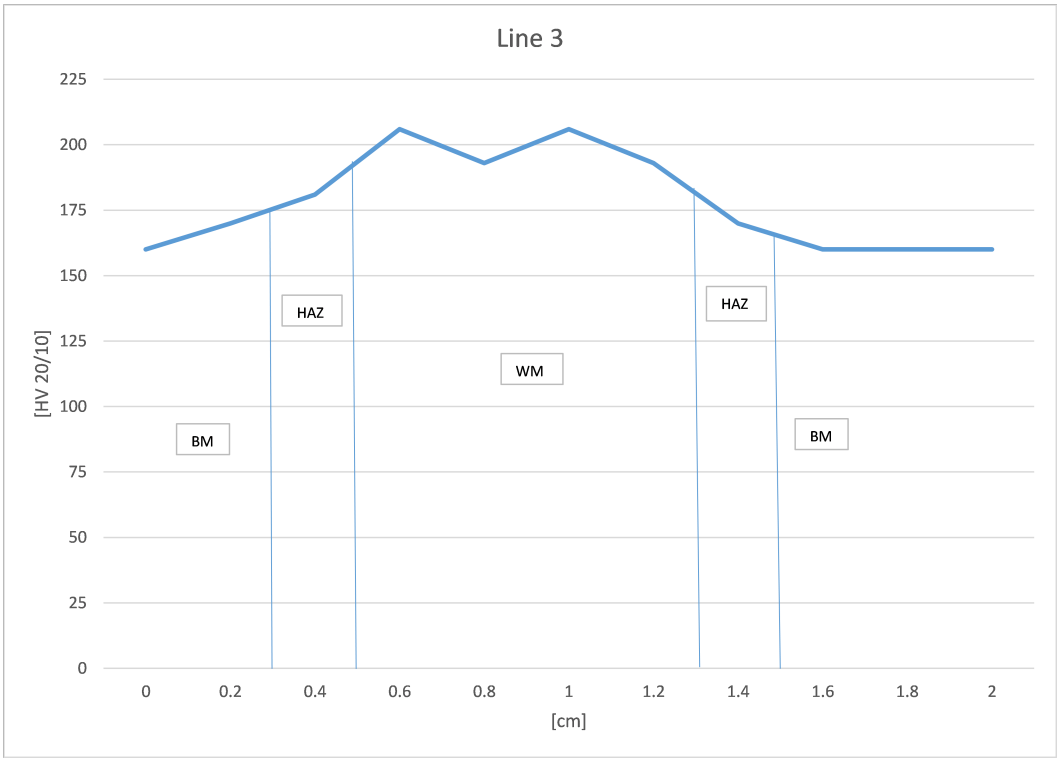



Figure 4.24: HV values Sample 2 Line 3.

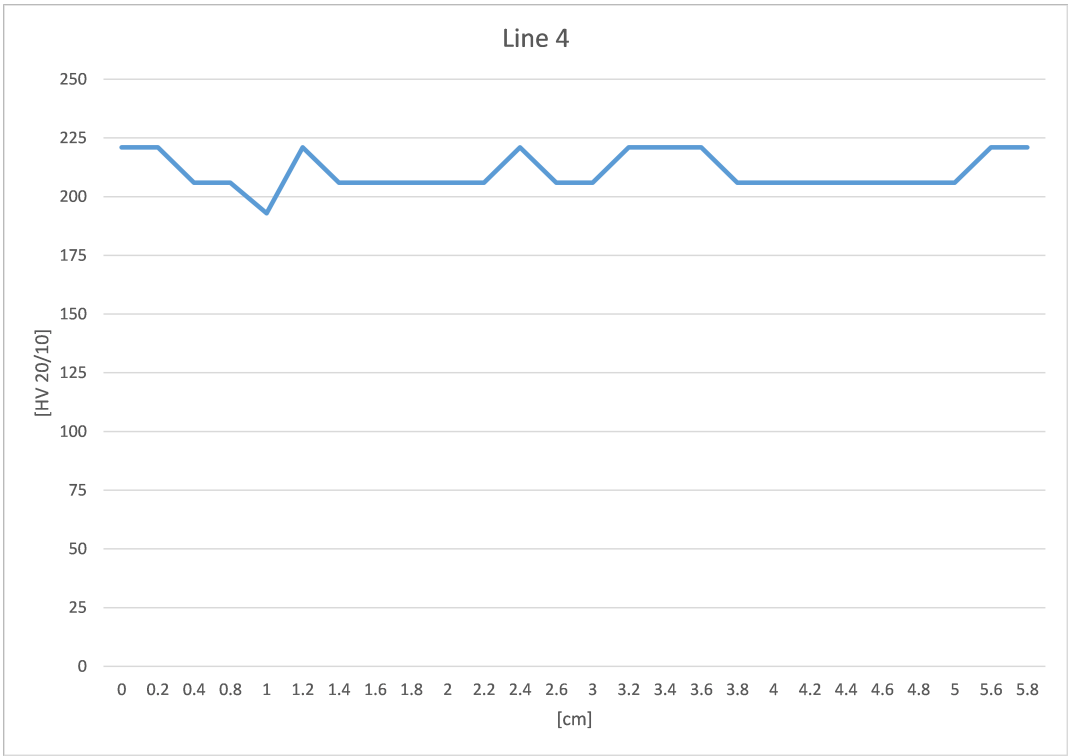



Figure 4.25: HV values Sample 2 Line 4.

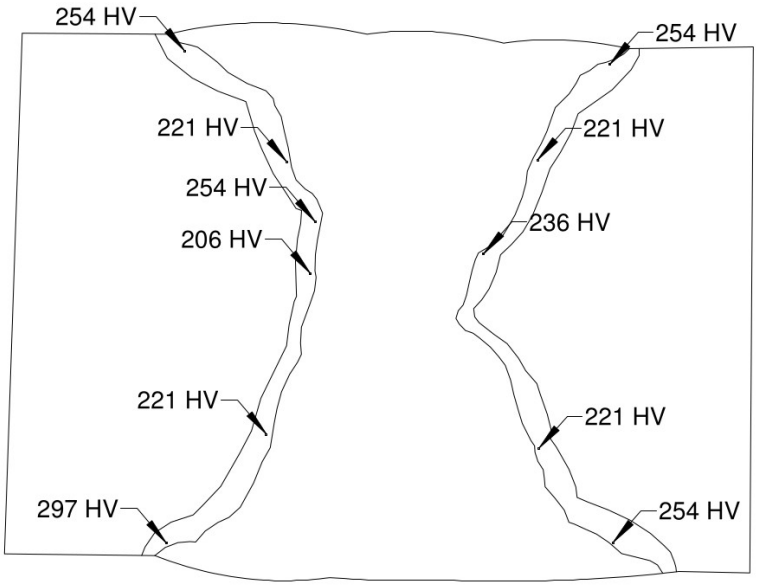



Figure 4.26: HV values HAZ Sample 1.

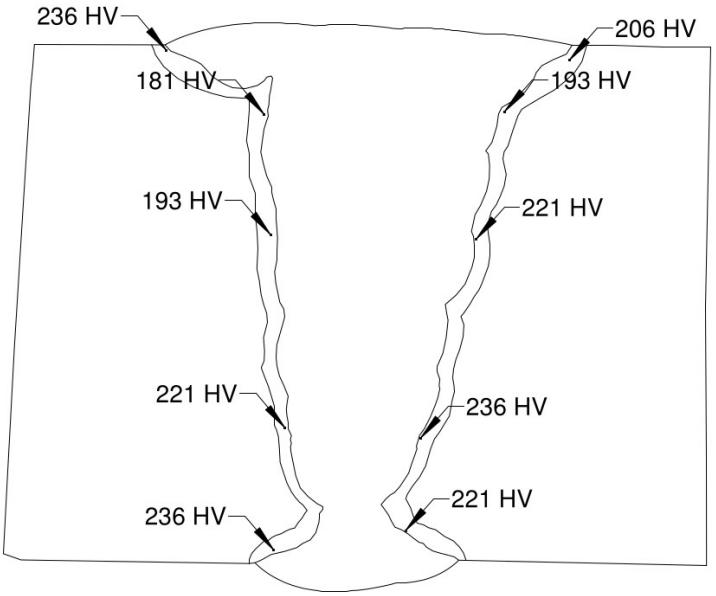



Figure 4.27: HV values HAZ Sample 2.

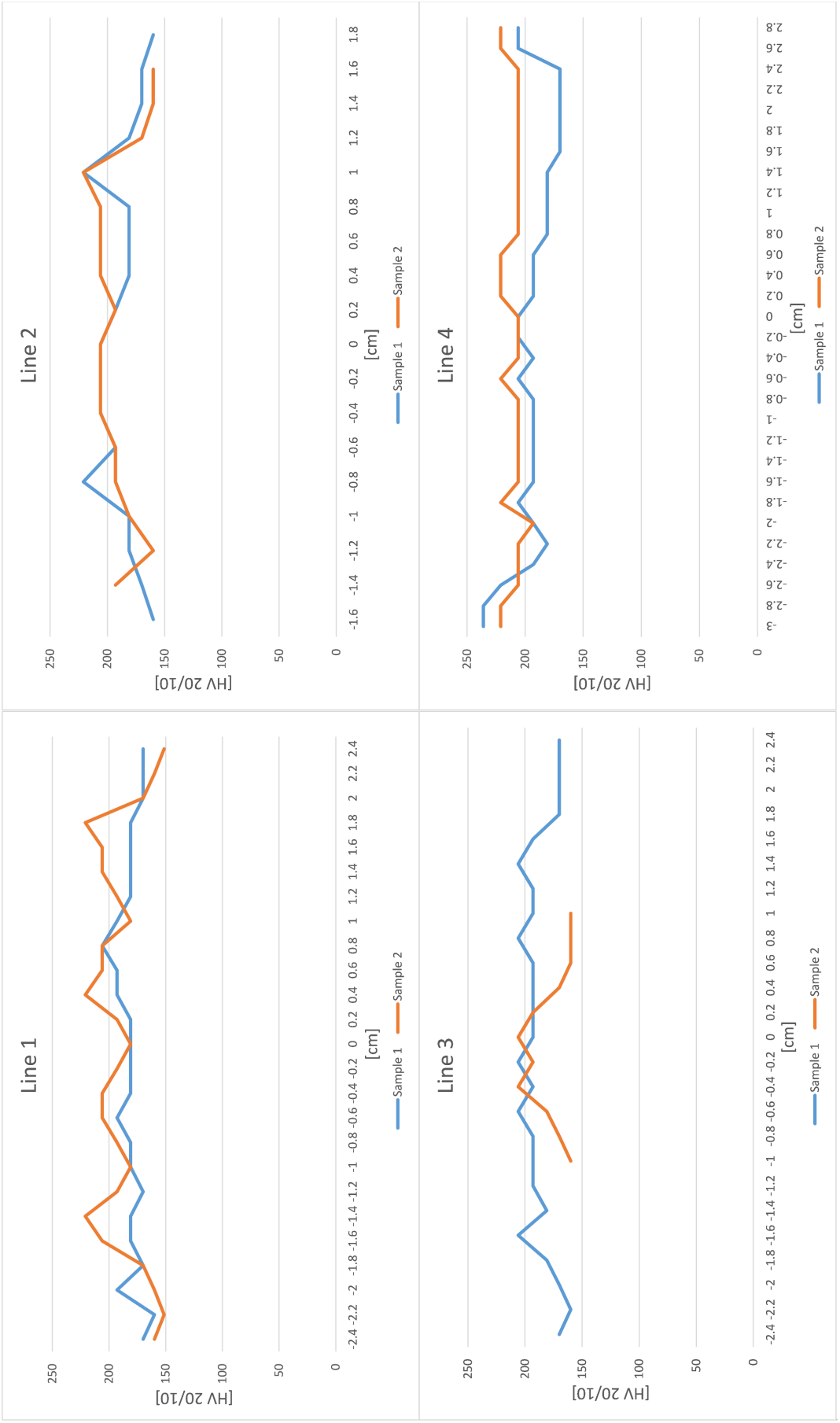



Figure 4.28: Hardness values comparison.

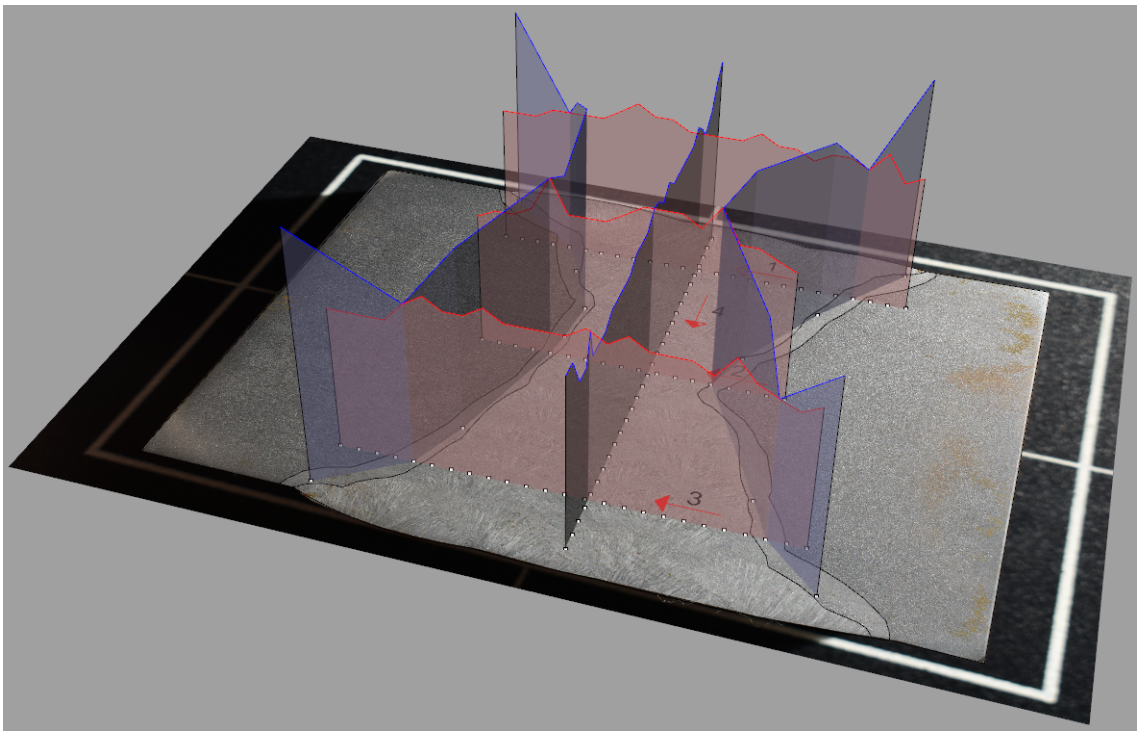



Figure 4.29: 3D Hardness profiles Sample 1.

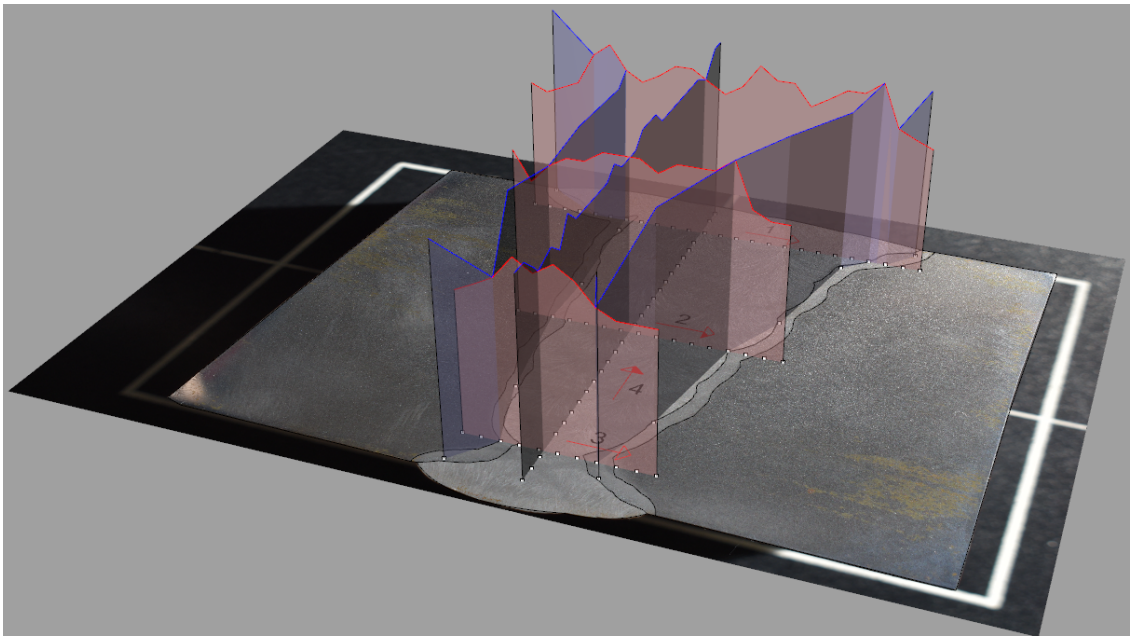



Figure 4.30: 3D Hardness profiles Sample 2.

## 4.5 Charpy Impact test

The Charpy impact values, shown in Tables 4.1, 4.2 and 4.3, are in accordance with the material properties provided by the manufacturers, presented in Tables 3.3 and 3.6, and are generally positive, although varying slightly. Tables 4.1 and 4.2 present the results of 3 tested specimens per location at - 20 ° C, as well as the average, while Table 4.3 displays 3 specimens per location but at varying temperatures. There is one anomaly, namely for Specimens A2, where the values for the impact test at - 20 ° C are lower than that for - 40 ° C. This fact can be explained by the presence of weld defects in the area or a repair to the weld that was undertaken or other impurities, although no defects were seen while the specimens were machined. Another explanation could be provided by the location of this specimen, in the root of the weld, where tack welds are placed before the SAW process and air-arc gauging is performed. The former explanation is more plausible since the impact values at - 40 ° C are higher than those at - 20 ° C. The rest of the results are in accordance with the standards and literature. The energy absorbed/temperature (KV/T) curve, shown in Figures 4.31 and 4.32, indicate softer micro-structures that exhibit more ductility for specimens A2 and A3, where the results at - 80 ° C are significantly higher than those of specimens A1 and A4.

Table 4.1: Impact values Sample 1.

| Type and Location | No. | Impact absorbed energy [J] | Impact toughness [J/cm$^2$] | Temperature [° C] |
|---|---|---|---|---|
| A1 | 1 | 221.03 | 276.29 | - 20 ° C |
| | 2 | 151.87 | 189.84 | - 20 ° C |
| | 3 | 181.70 | 227.13 | - 20 ° C |
| | Average | 184.87 | 231.09 | - 20 ° C |
| A2 | 1 | 97.63 | 122.04 | - 20 ° C |
| | 2 | 119.33 | 149.16 | - 20 ° C |
| | 3 | 84.07 | 105.09 | - 20 ° C |
| | Average | 100.34 | 125.43 | - 20 ° C |
| A3 | 1 | 199.33 | 249.17 | - 20 ° C |
| | 2 | 249.50 | 311.88 | - 20 ° C |
| | 3 | 259.00 | 323.75 | - 20 ° C |
| | Average | 235.94 | 294.93 | - 20 ° C |
| A4 | 1 | 238.66 | 298.32 | - 20 ° C |
| | 2 | 257.64 | 322.05 | - 20 ° C |
| | 3 | 214.25 | 267.81 | - 20 ° C |
| | Average | 243.74 | 304.68 | - 20 ° C |

Table 4.2: Impact values Sample 2.

| Type and Location | No. | Impact absorbed energy [J] | Impact toughness [J/cm$^2$] | Temperature [° C] |
|---|---|---|---|---|
| B1 | 1 | 111.19 | 138.99 | - 20 ° C |
| | 2 | 202.04 | 252.56 | - 20 ° C |
| | 3 | 206.11 | 257.64 | - 20 ° C |
| | Average | 173.12 | 216.40 | - 20 ° C |
| B2 | 1 | 200.69 | 250.86 | - 20 ° C |
| | 2 | 188.48 | 235.61 | - 20 ° C |
| | 3 | 195.26 | 244.08 | - 20 ° C |
| | Average | 194.81 | 243.52 | - 20 ° C |
| B3 | 1 | 261.71 | 327.14 | - 20 ° C |
| | 2 | 242.72 | 303.41 | - 20 ° C |
| | 3 | 267.13 | 333.92 | - 20 ° C |
| | Average | 257.19 | 321.49 | - 20 ° C |
| B4 | 1 | 235.94 | 294.93 | - 20 ° C |
| | 2 | 264.42 | 330.53 | - 20 ° C |
| | 3 | 253.57 | 316.97 | - 20 ° C |
| | Average | 251.31 | 314.14 | - 20 ° C |

Table 4.3: Impact values Sample 1 at lowered temperatures.

| Type and Location | No. | Impact absorbed energy [J] | Impact toughness [J/cm$^2$] | Temperature [° C] |
|---|---|---|---|---|
| A1 | 1 | 146.45 | 183.06 | - 40 ° C |
| | 2 | 81.36 | 101.70 | - 60 ° C |
| | 3 | 9.49 | 11.87 | - 80 ° C |
| A2 | 1 | 130.18 | 162.72 | - 40 ° C |
| | 2 | 86.78 | 108.48 | - 60 ° C |
| | 3 | 56.95 | 71.19 | - 80 ° C |
| A3 | 1 | 162.72 | 203.40 | - 40 ° C |
| | 2 | 109.84 | 137.30 | - 60 ° C |
| | 3 | 61.02 | 76.28 | - 80 ° C |
| A4 | 1 | 105.77 | 132.21 | - 40 ° C |
| | 2 | 59.66 | 74.58 | - 60 ° C |
| | 3 | 5.42 | 6.78 | - 80 ° C |

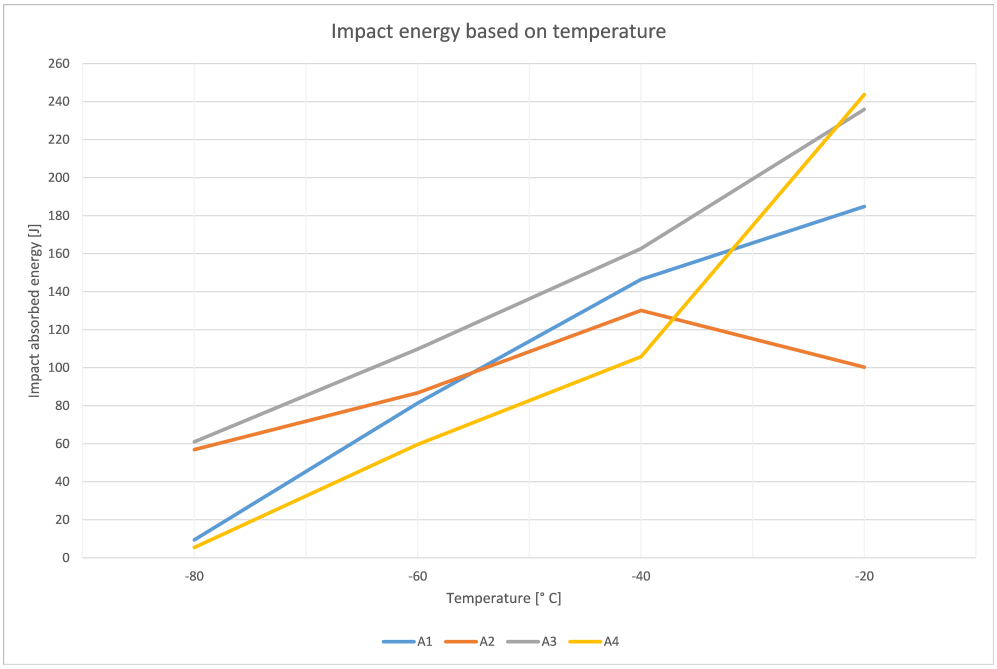



Figure 4.31: The energy absorbed/temperature curve for A type specimens at -20°C, -40°C, -60°C,-80°C.

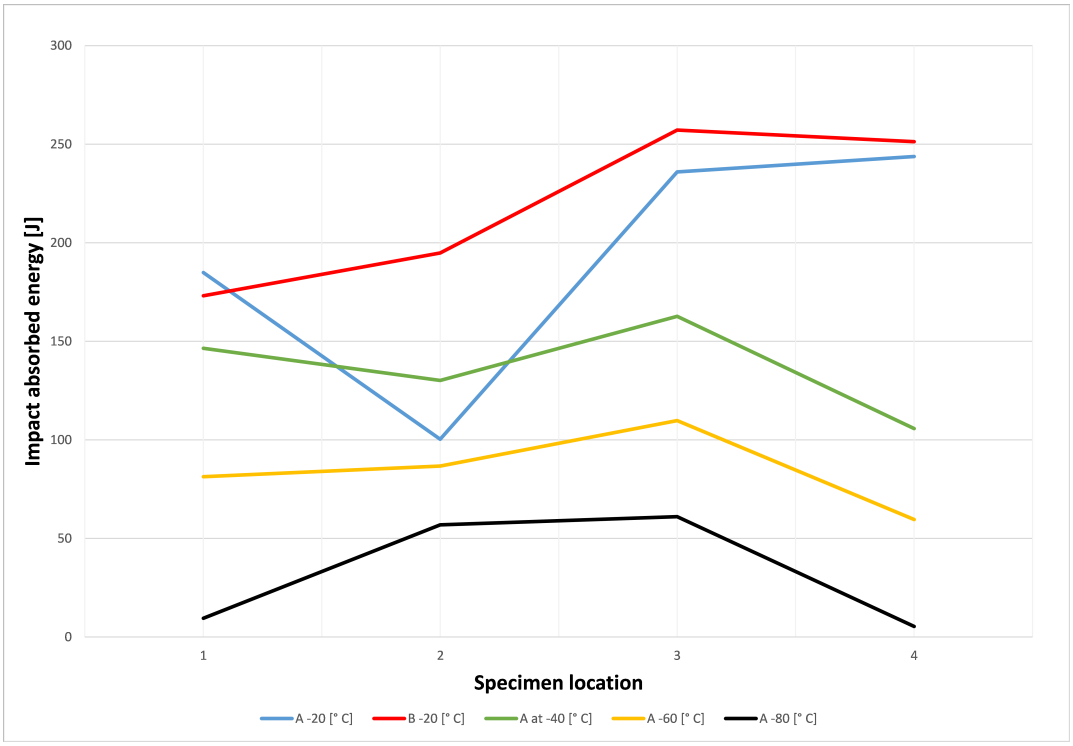



Figure 4.32: Energy absorbed for A type specimens at -20°C, -40°C, -60°C,-80°C and B type specimens at- 20°C.

The fracture appearance and later expansion are shown in Figures 4.33, 4.34 and 4.35. The

fracture appearance is similar for all the samples tested at -20°C, although for the samples that absorbed less energy, the areas tend to have a larger brittle fracture area, where crystallizing is clearly visible. This phenomenon can be observed in greater detail in Figure 4.35, where the brittle fracture area increases as the temperature decreases, until the fracture is completely brittle at -80°C. The same phenomenon can be observed in the case of lateral expansion as well, the specimens that absorbed more energy have a larger lateral expansion in comparison to the ones that absorbed less. This progression is evident in Figure 4.35, where no lateral expansion occurred for the specimen tested at -80°C.

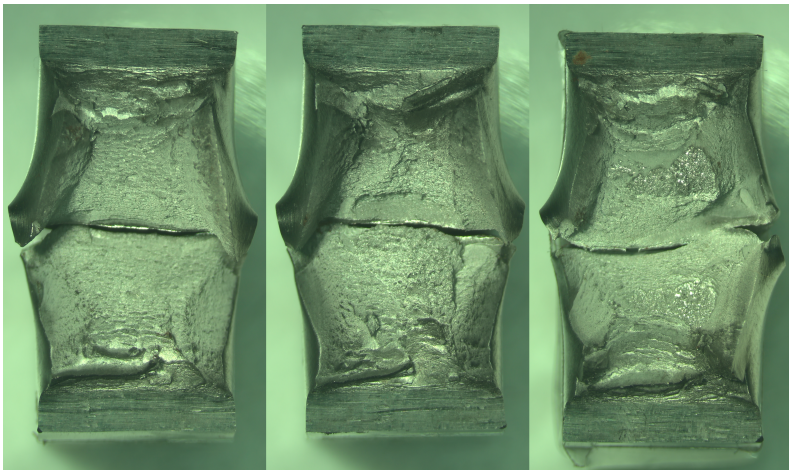


Figure 4.33: Fracture surface of Charpy test pieces A4 at -20°C.

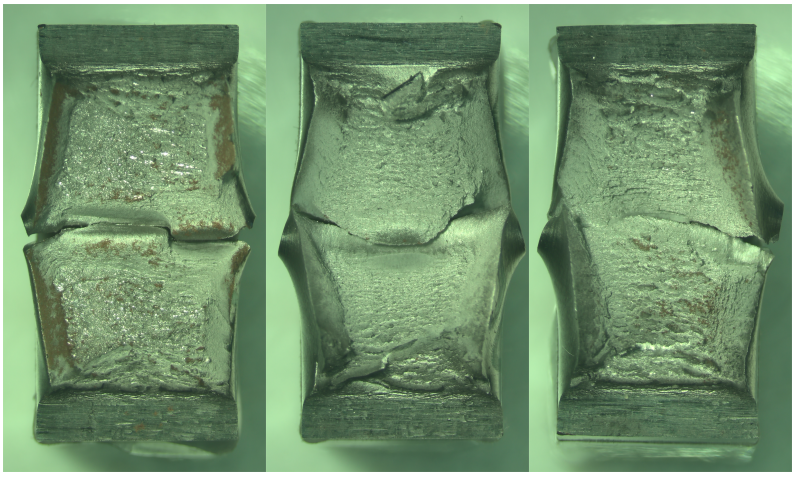


Figure 4.34: Fracture surface of Charpy test pieces B1 at -20°C.

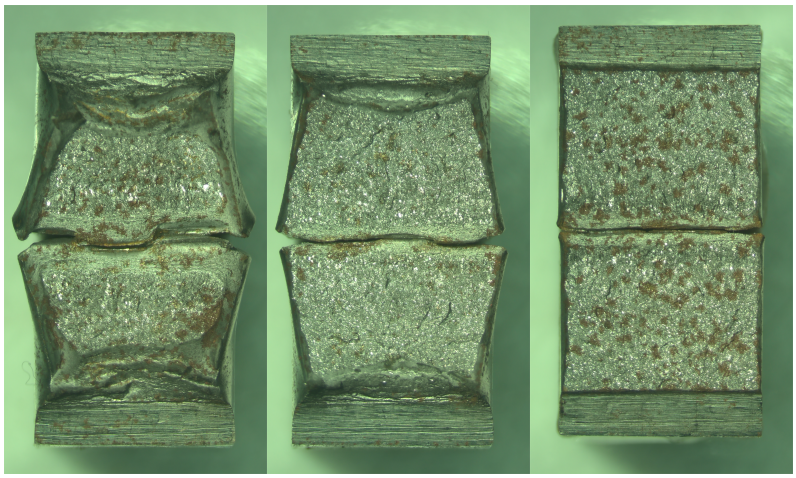


Figure 4.35: Fracture surface of Charpy Impact test pieces A1 at -40°C, -60°C and -80°C.

## 4.6 3D LSS

Having applied an image processing algorithm and the two parts stitched together, the result of the inner diameter was $D_LSS$ = 4.01577 m, comparing with the diameter provided by Tegopi $D_i$ = 4.177 m the measured results had a 3.7% deviation. This implies that the methodology applied is accurate and has the potential to be used in order to gather information regarding distortions more easily than standard gauge measuring. It will therefore be beneficial to monitor the geometric changes which occur during and after the welding process. Encouraging results have been achieved in the characterization of the tower's geometry, contributing to the assessment of robustness and accuracy of deployed 3D LSS [110].

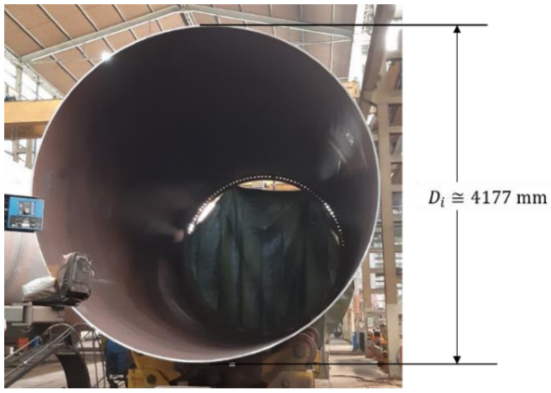



Figure 4.36: A-9-meter-long cylindrical part of a wind tower section [110].

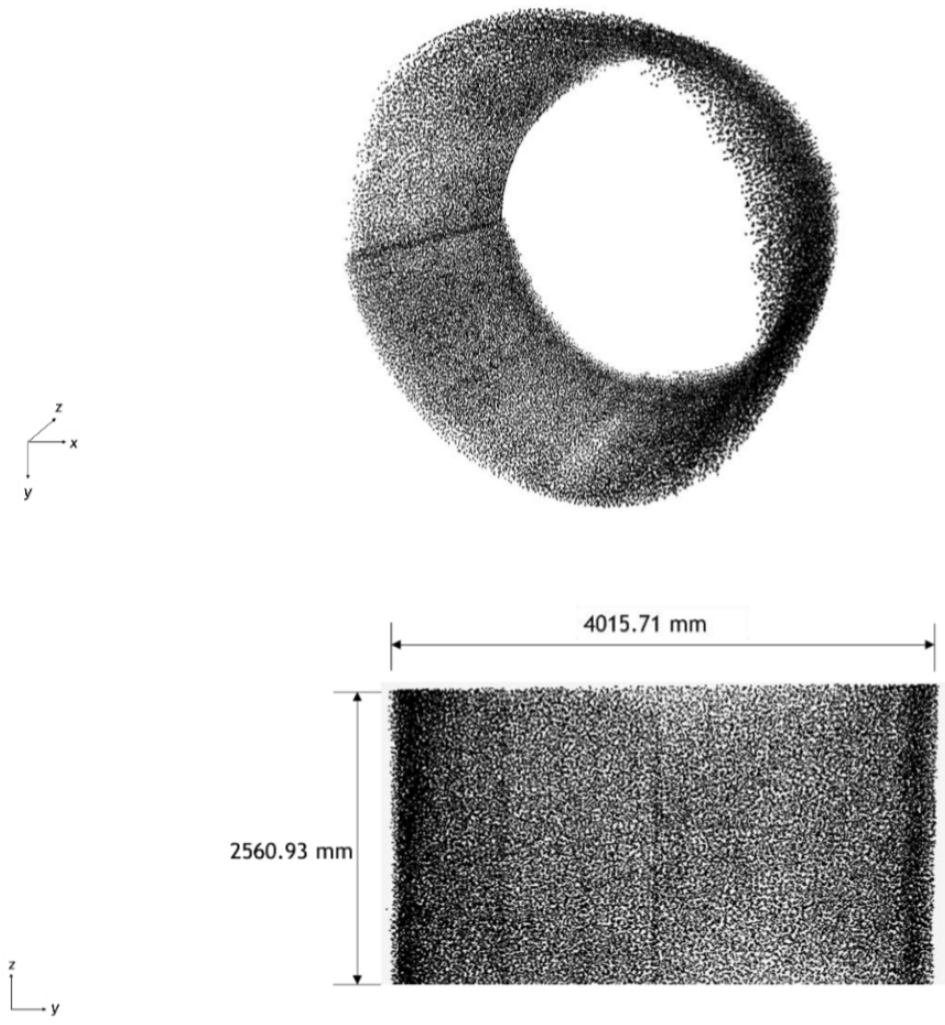



Figure 4.37: A 3D view of the tower profile and b) a top view of the tower with its dimensions obtained by 3D LSS [110].

# Chapter 5

# Conclusions and Future Work

This chapter presents the main conclusions, as well as an overview of the work and future research possibilities.

## 5.1 Conclusions

The motivation and interest in this project were twofold, one was the nature of the project, set in an industrial environment, which would allow not only insight into the production processes but rather offer hands-on experience instead of the traditional project which takes place mostly in an academic environment. The second one is the area in which it was set, the renewable energy sector, specifically wind turbine manufacturing, which play a major role in the movement away from fossil fuels and offers great future prospects.

The main objectives at the onset of this work were to aid Tegopi in identifying the causes of their unplanned outcomes. This translated into obtaining a balance between welding distortions and residual stress by means of optimizing the production process of wind tower sections. The proposed method was to investigate the submerged-arc welding process and assess the outcomes based on experimental work performed on a large number of samples, where the welding parameters could be varied, alongside numerical simulation. Using the experimental results, the numerical simulations could be refined and become robust enough to use as a control tool.

The time spent at Tegopi proved to be invaluable for the insights into the production process. The main problems that the company was facing were unplanned distortions that delayed deliveries and increased production costs. Highly skilled laborers were kept from performing their usual tasks because they had to spend time on re-rolling the distorted shells or machining the flanges in order to meet tolerances. Besides the time loss, it also led to increased manual labor and kept roller machines from producing more shells. The larger the distortions were, the more time it took the operators to correct the geometries. It was also observed that a higher volume of welds or higher heat inputs tended to result in higher distortions. The way in which the distortions tended to occur led to the conclusion that the problem could be, in part, caused by the rolling process. The machinery had some limitations in rolling the ends of the shells and required experienced operators to do so. The shells need to be tack-welded before the SAW process and because the shape was mismatched and not perfectly circular they were forced in position and then welded. For circular welds, due to buckling distortions, braces were welded inside the shells in order to bring them to the required positions. Another aspect was that the consumables needed to be kept in a controlled environment and away from moisture. The bevel geometry and surface could have had an effect on the distortions, and because the bevels were performed manually this led to imperfect results. During the SAW process, the internal welding specifications offered an upper and lower limit for the welding parameters controlled by the welding operator and were not recorded. The welding speed was kept constant for every individual weld pass but could vary between passes. It was controlled by the operators via welding robots for longitudinal welds, and roller beds for the circumferential welds.

Unfortunately, before these issues could be addressed, the company completely withdrew from the project due to economic circumstances and could not provide all the samples and assistance required to continue the work. Before this, a small number of samples were collected from door cut-outs that contained circumferential welds, which could offer a more comprehensive overview of the residual stress state and weld characteristics than mock-ups could.

The withdrawal of Tegopi coincided with the onset of the COVID-19 pandemic and its subsequent lock-downs, which caused major delays.

After the withdrawal of Tegopi, the approach and objectives had to be changed. Having already obtained the initial samples, which came from parts that would normally be scrapped, ASM was

contacted to assess the availability of providing similar samples in order to compare the welding process. They agreed and the second set of samples was provided from the same location as the first set of samples.

As a result of the experimental work, both sets of welds proved to be of high quality, with relatively good impact properties and hardness levels. There was one anomaly in the impact test results, the impact toughness was lower for the A2 type specimens at -20° C than the ones performed at -40° C for the same specimen type and location, but this can be attributed to the presence of weld defects or repairs that were not noted or observed previously. Because the A2 specimen tested at -40° C showed higher impact toughness, it can be concluded that if a defect was present it was localized, and not a general characteristic of the entire weld. The results of the impact tests performed at -20° C point to a higher impact toughness in the HAZ area of the welds than in the WM, but this changes as the temperature are reduced. Meanwhile, the hardness values were somewhat atypical, in the sense that it was expected to be higher in the HAZ, but some values were high for the WM area as well. The separate measurements performed specifically in the HAZ concur with the expected results, with Sample 1 having provided marginally higher values than Sample 2.

The macro-structure revealed the bevel geometry and number of weld passes, which is a double-V with 30 identifiable passes for Sample 1 and single-U with 25 passes for Sample 2. When a lower number of passes is used, it implies that a larger heat input may have to be used, which in turn can lead to coarse grain growth and lowered impact properties. Also, in order to increase weld deposition rates, a higher current must be used which increases the welding speed and leads to higher heat inputs. On the other hand, lowered heat inputs can lead to hydrogen cracking. The single-U bevel has the disadvantage that it is more costly and difficult to prepare and weld, but it usually is less costly to fill.

## 5.2 Future Work

The thesis plan at the onset of the project was to perform a detailed analysis of the welding parameters and obtain an insight into the balance between residual stress and distortions. Because the company which initiated the project withdrew before the experimental work began, the goals

had to be modified. In essence, the initial goals became the prospects for future work. Obtaining a large number of samples, some from door-cutouts and some that would be welded mock-ups, in which the welding parameters and geometries can be varied and controlled in order to ascertain the effects they have on the residual stress and distortions. Distortions can be measured using a 3D LSS, that INEGI already has. A new method of obtaining multiple components of residual stress can be applied, this method was discussed in Chapter 2, Primary Slice Removal (PSR) Mapping, which combines the contour method and slitting method. This, coupled with Computational welding mechanic (CWM) simulations, recording the values of welding parameters and scanning the resulting distortions could be gathered and fed into an Artificial Neural Network, which would be trained to predict future welding distortions or used as a control tool. It was proved that the residual stress values can be obtained experimentally, the resulting distortions can be quantified and the weld characteristics pertaining to impact toughness, hardness, and microstructural changes can be easily obtained and employed to optimize the submerged-arc welding process used in wind turbine support structures.

# References


[1] Dieter Radaj. *Heat Effects of Welding*. 2012.

[2] Klas Weman. *Welding processes handbook*. Woodhead Publishing Limited, 2nd edition, 2012.

[3] Tom Gray, Duncan Camilleri, and Norman McPherson. *Control of Welding Distortion in Thin-Plate Fabrication: Design Support Exploiting Computational Simulation*. 01 2014.

[4] Tegopi.pt. http://www.tegopi.pt/?mod=pdinamicas_pagid=2&_topitem=8&a_ling=gb March 2019.

[5] eurostat.eu. Renewable energy statistics. Eurostat.eu (2019, April 5). Retrieved from Eurostat:, 04 2019.

[6] eurostat.eu. Renewable energy statistics. Eurostat.eu (2022, January). Retrieved from Eurostat:, 01 2022.

[7] P.J. Withers and H.K.D.H. Bhadeshia. Residual stress. part 1 – measurement techniques. *Materials Science and Technology*, 17(4):355–365, 2001.

[8] P.J. Withers and H.K.D.H. Bhadeshia. Residual stress. part 2 – nature and origins. *Materials Science and Technology*, 17(4):366–375, 2001.

[9] Juhwa Lee, Jeongho Hwang, and Dongho Bae. Welding residual stress analysis and fatigue strength assessment at elevated temperature for multi-pass dissimilar material weld between alloy 617 and P92 steel. *Metals and Materials International*, 24(4):877–885, 2018.

[10] Mike C. Smith, Ann C. Smith, Carsten Ohms, and Robert C. Wimpory. The NeT Task Group 4 residual stress measurement and analysis round robin on a three-pass slot-welded plate specimen. *International Journal of Pressure Vessels and Piping*, 164(April 2016):3–21, 2018.

[11] Mads R. Sonne, Pierpaolo Carlone, and Jesper H. Hattel. Assessment of the contour method for 2-D cross sectional residual stress measurements of friction stirwelded parts of AA2024-T3—numerical and experimental comparison. *Metals*, 7(11), 2017.

[12] R. Citarella, P. Carlone, R. Sepe, and M. Lepore. DBEM crack propagation in friction stir welded aluminum joints. *Advances in Engineering Software*, 101:50–59, 2016.

[13] M. Farahani, S. Hakkak Zargar, and D. Akbari. Investigation of the effects of the weld groove shape on the residual stress formation in the butt-welded plates. *Scientia Iranica*, 23(5):2230–2237, 2016.

[14] Mitchell D. Olson, Michael R. Hill, Eric Willis, Artie G. Peterson, Vipul I. Patel, and Ondrej Muránsky. Assessment of weld residual stress measurement precision: Mock-up design and results for the contour method. *Journal of Nuclear Engineering and Radiation Science*, 1(3):1–10, 2015.

[15] Lang Shi, Angie Hill Price, and Wayne Nguyen Hung. Use of Contour Method for Welding Residual Stress Assessment. *Procedia Manufacturing*, 26:276–285, 2018.

[16] M. D. Olson, A. T. DeWald, and M. R. Hill. Assessment of Primary Slice Release Residual Stress Mapping in a Range of Specimen Types. *Experimental Mechanics*, 58(9):1371–1388, 2018.

[17] Anais Jacob, Jeferson Oliveira, Ali Mehmanparast, Foroogh Hosseinzadeh, Joe Kelleher, and Filippo Berto. Residual stress measurements in offshore wind monopile weldments using neutron diffraction technique and contour method. *Theoretical and Applied Fracture Mechanics*, 96(January):418–427, 2018.

[18] Khalid Nasim, A. F.M. Arif, Y. N. Al-Nassar, and M. Anis. Investigation of residual stress development in spiral welded pipe. *Journal of Materials Processing Technology*, 215(1):225–238, 2015.

[19] Wei Tong. *Wind Power Generation and Wind Turbine Design*. WIT Press, 2010.

[20] Erich Hau. *Wind Turbines: Fundamentals, Technologies, Application, Economics*. 2013.

[21] Muyiwa Adaramola. *Wind Turbine Technology: Principles and Design*. Taylor Francis Group, 2014.

[22] Jan van der Tempel. Design of support structures for offshore wind turbines, 2006.

[23] Peter Jamieson. *Innovation in wind turbine design: Second edition*. 2017.

[24] Tony Burton, Nick Jenkins, David Sharpe, and Ervin Bossanyi. Wind energy handbook, second edition. *Wind Energy Handbook, Second Edition*, 2011.

[25] Felix Von König. *Windenergie in praktischer Nutzung. Räder, Rotoren, Mühlen, Windkraftwerke*. Pfriemer, 1981.

[26] Wolfgang Fröde. *Windmühlen*. Ellert Richter, 1987.

[27] Notebaart J.C. *Windmühlen*. Mouton-Verlag, 1972.

[28] Torrey V. *Wind Catchers*. The Stephen Greene Press, 1976.

[29] Rex Wailes. Horizontal windmills. *Transactions of the Newcomen Society*, 40(1):125–145, 1967.

[30] A.Y. Al-Hassan, M. Ahmed, and A.Z. Iskandar. *Science and Technology in Islam: The exact and natural sciences*. Different aspects of Islamic culture. UNESCO Pub., 2001.

[31] Adam Lucas. *Wind, Water, Work: Ancient and Medieval Milling Technology*. 2011.

[32] R.L. Hills. *Power from Wind: A History of Windmill Technology*. Cambridge University Press, 1993.

[33] E.W. Golding. *The Generation of Electricity by Wind Power*. London : E. F.N. Spon ; New York : Distributed by Halsted Press, 1977.

[34] H.C. Hansen. *Forsøgsmøllen in Askov*. Dansk Udysyns Forlag, 1981.

[35] La Cour P. *Forsøgsmøllen*. Det Nordiskke Forlag, 1900.

[36] D. Stein. *Windkraftanlagen in Dänemark*. RAW-Denkschrift 4, 1942.

[37] C. Westh. *Experiences with the F.L. Smidth Aeromotors*. In: 6th IEA Expert Meeting LS-WECS, Aalborg, 1981.

[38] K. Bilau. *Die Windkraft in Theorie und Praxis*. Paul Parey Verlag, 1927.

[39] K. Bilau. *Die Windausnutzung für die Krafterzeugung, 2nd ed.* Paul Parey Verlag, 1933.

[40] A. Betz. *Das Maximum der theoretisch möglichen Ausnutzung des Windes durch Windmotoren, Zeitschrift für das gesamte Turbinenwesen*. 1920.

[41] A. Betz. *Windenergie und ihre Ausnutzung durch Windmühlen, Vandenhoekk and Ruprecht*. 1926.

[42] H. Honnef. *Windkraftwerke*. Vieweg & Sohn, 1932.

[43] P.C. Putnam. *Power from the Wind*. Van Nostrand Reinold Company, 1947.

[44] U. Hütter. *Die Entwicklung von Windkraftanlagen zur Stromerzeugung in Deutschland*. vol. 6, no. 7, BWK, 1954.

[45] Ministry of Energy (Danish Energy Agency). *Wind Energy in Denmark, Research and Technological Development*. 1990.

[46] A. Zervos. Wind power as a mainstream energy source. 2009.

[47] V. Nelson. Wind energy – renewable energy and the environment. 2009.

[48] Moubayed N. Outbib R. El-Ali, A. Comparison between solar and wind energy in lebanon. 2007.

[49] P. Gipe. Wind energy comes of age. 1995.

[50] E2P.INEGI. Wind farms in portugal. Retrieved on the 3rd of April 2022 http://e2p.inegi.up.pt.

[51] Global Wind Atlas. Retrieved on March 29th 2022 from https://globalwindatlas.info/.

[52] Energy BC. Retrieved from http://www.energybc.ca/wind.html, April 2019.

[53] Annette Evans, Vladimir Strezov, and Tim J. Evans. Assessment of sustainability indicators for renewable energy technologies. *Renewable and Sustainable Energy Reviews*, 13(5):1082–1088, 2009.

[54] NREL. Nrel: Dynamic maps, gis data, and analysis tools – wind maps. Retrieved from https://www.nrel.gov/gis/wind.html, Septemeber 2013.

[55] S. Barber, Y. Wang, S. Jafari, N. Chokani, and R. S. Abhari. The Impact of Ice Formation on Wind Turbine Performance and Aerodynamics. *Journal of Solar Energy Engineering*, 133(1), 01 2011. 011007.

[56] A. Quilligan, A. O'Connor, and V. Pakrashi. Fragility Analysis of Steel and Concrete Wind Turbine Towers. *Engineering Structures 36 J.ENGSTRUCT*, 133(1), January 2012. 011007.

[57] Wiser Ryan, Bolinger Mark, and Lawrence Berkeley National Laboratory. Land-based wind market report: 2021 edition. Office of Energy Efficiency and Renewable Energy U.S. Department of Energy.

[58] Charalambos Baniotopoulos, Claudio Borri, and Theodore Stathopoulos. *Environmental Wind Engineering and Design of Wind Energy Structures*. 01 2011.

[59] ESAB. Retrieved from https://www.esabna.com/us/en/products/welding-automation-robotics/submerged-arc-welding-saw/controllers/a2-a6-pek-process-controller.cfm.

[60] ESAB. Technical handbook. submerged arc welding. Retrieved from https://assets.esab.com/assetbank-esab/assetfile/12295.pdf, March 2017.

[61] K. Masubuchi. *Analysis of welded structures*, volume 15. 1982.

[62] P T Houldcroft. *SUBMERGED-ARC Welding*. 1989.

[63] L.T. Jones, H.E. Kennedy, and M.A. Rotermund. Us patent 2043960.

[64] Serope Kalpakjian and Steven R. Schmid. *Manufacturing, Engineering Technology, 5th Edition*. Prentice Hall, 2005.

[65] Larry Jeffus. *Welding: Principles and Applications 8th Edition*. Delmar Learning, 2002.

[66] P. Michaleris. *Minimization of Welding Distortion and Buckling: Modelling and Implementation*. 2011.

[67] Ajitanshu Vedrtnam, Gyanendra Singh, and Ankit Kumar. Optimizing submerged arc welding using response surface methodology, regression analysis, and genetic algorithm. *Defence Technology*, 14(3):204–212, 2018.

[68] M. Sailender, G. Chandramohan Reddy, and S. Venkatesh. Influences of process parameters on weld strength of low carbon alloy steel in purged SAW. *Materials Today: Proceedings*, 5(1):2928–2937, 2018.

[69] Aman Singh and R. P. Singh. A review of effect of welding parameters on the mechanical properties of weld in submerged Arc welding process. *Materials Today: Proceedings*, 26:1714–1717, 2019.

[70] Prachya Peasura. Investigation of the Effects of Submerged Arc Welding Process Parameters on the Mechanical Properties of Pressure Vessel Steel ASTM A283 Grade A. *Journal of Engineering (United Kingdom)*, 2017, 2017.

[71] J. Edwin Raja Dhas and S. Kumanan. Optimization of parameters of submerged arc weld using non conventional techniques. *Applied Soft Computing Journal*, 11(8):5198–5204, 2011.

[72] Deepak Gupta Mohit Sharma and Karun. Submerged Arc Welding : A Review. *International Journal of Current Engineering and Technology*, 4(3):1814–1817, 2014.

[73] A Batta, J Aggarwal, V Khurana, and A Sandhu. Optimization of Submerged Arc Welding Process: A Review. *IOSR Journal of Mechanical and Civil Engineering Ver. II*, 12(2):2320–334, 2015.

[74] German Standard. DIN 1910-100:2008-02.

[75] H. Koch. *Beitriige zu den Fragen der Formabweichungen und Eigenspannungen beim Schmelz- schweil3en. In: Schweilen und Schneiden, Forschritte in den Grundlagen und in der Anwen- dung, pp. 130-135. Dusseldorf: DVS-Verlag*. 1966.

[76] L Karlsson. *Thermal stresses in welding. In: Thermal stresses, Vol. 1 (Ed.: R.B. Hetnarski), pp. 299-389. Amsterdam: North-Holland*. 1986.

[77] N. Rykalin. *Berechnung der Wiirmevorgiinge beim SchweiBen. Berlin: VEB Verlag Technik (Original: Raschety teplovykh protsessov pri svarke. Moscow: Mashgiz 1951)*. 1957.

[78] European Comittee for Standardization. EN 1011-1:2009 Welding - Recommendations for welding of metallic materials - Part 1: General guidance for arc welding.

[79] B. Buchmayr. *WEZ-Kalkulator, ein Softwarepaket zum Berechnen schweiBtechnischer Kenn- werte. SchweiB. u. Schneid. 41 no. 3, pp. 69-75*. 1989.

[80] Lars-Erik Lindgren. *Computational welding mechanics*.

[81] Zhili Feng. *Processes and mechanisms of welding residual stress and distortion*.

[82] N.O. Okerblom. *The calculation of deformations of welded metal structures.(Original: Raschet deformatsii metallokonstruktsii pri svarke. Moscow: Mashgiz 1955)*. H. M. Stationery Office, London, 1958.

[83] German Standard. DIN 8528-1.

[84] S. Buchmayr, B.and Kirkaldy. *Modeling of the temperature field, transformation behavior, hardness and mechanical response of low alloy steels during cooling from the austenite region. J. Heat Treat. 8 no. 2, pp. 127-136*. 1990.

[85] Barbara Kitchenham and Pearl Brereton. A systematic review of systematic review process research in software engineering. *Information and Software Technology*, 55(12):2049–2075, 2013.

[86] David Moher, Alessandro Liberati, Jennifer Tetzlaff, and Douglas G. Altman. Preferred reporting items for systematic reviews and meta-analyses: The PRISMA statement. *International Journal of Surgery*, 8(5):336–341, 2010.

[87] Alessandro Liberati, Douglas G. Altman, Jennifer Tetzlaff, Cynthia Mulrow, Peter C. Gøtzsche, John P.A. Ioannidis, Mike Clarke, P. J. Devereaux, Jos Kleijnen, and David Moher. The PRISMA statement for reporting systematic reviews and meta-analyses of studies that evaluate health care interventions: Explanation and elaboration. *PLoS Medicine*, 6(7), 2009.

[88] Pablo Vicente Torres-Carrion, Carina Soledad Gonzalez-Gonzalez, Silvana Aciar, and Germania Rodriguez-Morales. Methodology for systematic literature review applied to engineering and education. *IEEE Global Engineering Education Conference, EDUCON*, 2018-April:1364–1373, 2018.

[89] Matthew J. Page, Joanne E. McKenzie, Patrick M. Bossuyt, Isabelle Boutron, Tammy Hoffmann, Cynthia D. Mulrow, Larissa Shamseer, and David Moher. Mapping of reporting guidance for systematic reviews and meta-analyses generated a comprehensive item bank for future reporting guidelines. *Journal of Clinical Epidemiology*, 118:60–68, 2020.

[90] AH Mahmoudi, S Hossain, CE Truman, DJ Smith, and MJ Pavier. A new procedure to measure near yield residual stresses using the deep hole drilling technique. *Experimental Mechanics*, 49(4):595 – 604, August 2009. Publisher: Springer Boston.

[91] Houichi Kitano, Shigetaka Okano, and Masahito Mochizuki. A study for high accuracy measurement of residual stress by deep hole drilling technique. *Journal of Physics: Conference Series*, 379:012049, aug 2012.

[92] Veqter Ltd. Centre hole drilling. Retrieved on 25 February 2014 https://www.veqter.co.uk/residual-stress-measurement/centre-hole-drilling.

[93] G2MT Laboratories. Residual stress measurement by rosette hole drilling per astm e 837. Retrieved on February 3rd 2020 . https://www.g2mtlabs.com/residual-stress-measurement-rosette-hole-drilling-astm-837/.

[94] ASTM. ASTM E 837: Standard Test Method for Determining Residual Stress by the Hole Drilling Strain-Gauge Method, ASTM Standard, American Society for Testing and Materials.

[95] Paolo Ferro and Filippo Berto. *Residual Stress Analysis on Welded Joints by Means of Numerical Simulation and Experiments*. IntechOpen, Rijeka, 2018.

[96] Roberto Montanari, Alessandra Fava, and Giuseppe Barbieri. Experimental techniques to investigate residual stress in joints. In Paolo Ferro and Filippo Berto, editors, *Residual Stress Analysis on Welded Joints by Means of Numerical Simulation and Experiments*, chapter 1. IntechOpen, Rijeka, 2018.

[97] J. Ribeiro, J. Monteiro, M. Vaz, H. Lopes, and P. Piloto. Measurement of residual stresses with optical techniques. *Strain*, 45(2):123–130, 2009.

[98] Tomas Navrat, Dávid Halabuk, and P. Vosynek. Efficiency of plasticity correction in the hole-drilling residual stress measurement. *Materials*, 13:3396, 07 2020.

[99] M. B. Prime. Cross-Sectional Mapping of Residual Stresses by Measuring the Surface Contour After a Cut . *Journal of Engineering Materials and Technology*, 123(2):162–168, 11 2000.

[100] P. Pagliaro, M. B. Prime, J. S. Robinson, B. Clausen, H. Swenson, M. Steinzig, and B. Zuccarello. Measuring inaccessible residual stresses using multiple methods and superposition. *Experimental Mechanics*, 51(7):1123 – 1134, 2011.

[101] Hans Schindler. Residual stress measurement in cracked components: Capabilities and limitations of the cut compliance method. *Materials Science Forum - MATER SCI FORUM*, 347-349:150–155, 05 2000.

[102] Michael R. Hill. *The Slitting Method*, chapter 4, pages 89–108. John Wiley Sons, Ltd, 2013.

[103] European Comittee for Standardization. EN 1993-1-1:2005 Eurocode 3: Design of steel structures - Part 1-1: General rules and rules for buildings.

[104] Jean-Marc Franssen and Paulo Vila Real. *Fire Design of Steel Structures Annex C: Mechanical Properties of Carbon Steel and Stainless Steel*, pages 407–427. John Wiley Sons, Ltd, 2016.

[105] European Comittee for Standardization. EN 1993-1-1:2005 Eurocode 3: Design of steel structures - Part 1-2: General rules-Structural fire design.

[106] Michael B. Prime and Adrian T. DeWald. *The Contour Method*, chapter 5, pages 109–138. John Wiley Sons, Ltd, 2013.

[107] Marc A. Meyers and Krishan K. Chawla. *Mechanical Behavior of Materials.* Cambridge University Press, 2009.

[108] V. Richter-Trummer. *Residual stress effects and damage tolerance behaviour of integral lightweight structures manufactured by FSW and HSM.* Faculty of Engineering of the University of Porto, 2011.

[109] D. Braga. *Contour Method: Procedure Optimization.* Faculty of Engineering of the University of Porto, 2012.

[110] Behzad V. Farahani, Francisco Barros, Mihai A. Popescu, Pedro J. Sousa, Paulo J. Tavares, and Pedro Moreira. Geometry acquisition and 3d modelling of a wind tower using a 3d laser scanning technology. *Procedia Structural Integrity*, 17:712–717, 2019. 3rd International Conference on Structural Integrity, ICSI 2019, 2-5 September 2019, Funchal, Madeira, Portugal.

# Appendix A

Table A.1: Stress-strain relationship of S355 at elevated temperatures [103, 104].

| Strain | Effective yield strength $f_{y,\theta}$ | | | | | | | |
|---|---|---|---|---|---|---|---|---|
| | Steel temperature $\theta_a$ [°C] | | | | | | | |
| | 100 | 200 | 300 | 400 | 500 | 600 | 700 | 800 |
| 0.000 | 0.000 | 0.000 | 0.000 | 0.000 | 0.000 | 0.000 | 0.000 | 0.000 |
| 0.001 | 105.080 | 80.230 | 84.135 | 73.485 | 62.835 | 32.660 | 13.490 | 9.585 |
| 0.001 | 210.080 | 188.860 | 167.915 | 146.970 | 126.025 | 64.965 | 27.335 | 18.460 |
| 0.002 | 314.885 | 283.645 | 233.235 | 184.600 | 154.425 | 81.650 | 35.500 | 22.010 |
| 0.002 | 355.000 | 301.040 | 250.630 | 204.480 | 168.980 | 91.590 | 40.470 | 23.785 |
| 0.003 | 355.000 | 307.430 | 262.345 | 219.745 | 179.985 | 99.045 | 44.730 | 25.560 |
| 0.003 | 355.000 | 312.400 | 271.575 | 232.170 | 188.860 | 105.080 | 47.925 | 26.625 |
| 0.004 | 355.000 | 316.600 | 279.030 | 243.175 | 196.670 | 110.760 | 51.120 | 27.690 |
| 0.004 | 355.000 | 320.050 | 285.775 | 252.760 | 203.770 | 115.375 | 53.605 | 28.755 |
| 0.005 | 355.000 | 323.050 | 291.810 | 261.280 | 209.805 | 119.635 | 56.090 | 29.465 |
| 0.005 | 355.000 | 325.890 | 297.135 | 269.090 | 215.485 | 123.540 | 58.220 | 30.530 |
| 0.006 | 355.000 | 328.375 | 302.105 | 276.190 | 220.455 | 127.445 | 59.995 | 31.240 |
| 0.006 | 355.000 | 330.860 | 306.720 | 282.935 | 225.425 | 130.640 | 61.770 | 31.950 |
| 0.007 | 355.000 | 332.990 | 310.980 | 288.970 | 229.685 | 133.835 | 63.545 | 32.305 |
| 0.007 | 355.000 | 334.765 | 314.530 | 294.650 | 233.945 | 136.675 | 64.965 | 33.015 |
| 0.008 | 355.000 | 336.540 | 318.080 | 299.975 | 237.495 | 141.645 | 66.385 | 33.370 |
| 0.008 | 355.000 | 338.315 | 321.630 | 304.945 | 241.045 | 144.130 | 67.805 | 34.080 |
| 0.009 | 355.000 | 339.735 | 324.825 | 309.560 | 244.595 | 146.260 | 69.225 | 34.435 |
| 0.009 | 355.000 | 341.155 | 327.665 | 313.820 | 247.435 | 148.035 | 70.290 | 34.790 |
| 0.010 | 355.000 | 342.575 | 330.150 | 318.080 | 250.275 | 150.165 | 71.355 | 35.465 |
| 0.010 | 355.000 | 343.995 | 332.635 | 321.630 | 253.115 | 151.940 | 72.420 | 35.855 |
| 0.011 | 355.000 | 346.125 | 337.250 | 328.375 | 257.730 | 155.135 | 74.195 | 36.210 |
| 0.012 | 355.000 | 348.255 | 341.155 | 334.410 | 261.990 | 156.555 | 75.970 | 36.920 |
| 0.013 | 355.000 | 349.675 | 344.705 | 339.380 | 265.540 | 159.040 | 77.390 | 37.630 |
| 0.014 | 355.000 | 351.095 | 347.545 | 343.640 | 268.735 | 161.170 | 78.455 | 37.985 |
| 0.015 | 355.000 | 352.515 | 349.675 | 347.190 | 271.220 | 162.945 | 79.520 | 38.340 |
| 0.016 | 355.000 | 353.225 | 351.805 | 350.030 | 273.350 | 164.365 | 80.230 | 38.695 |
| 0.017 | 355.000 | 353.935 | 353.225 | 352.160 | 274.770 | 165.430 | 80.940 | 38.695 |
| 0.018 | 355.000 | 354.645 | 354.290 | 353.935 | 276.190 | 166.140 | 81.295 | 39.050 |
| 0.019 | 355.000 | 355.000 | 354.645 | 354.645 | 276.545 | 166.850 | 81.650 | 39.050 |
| 0.020 | 355.000 | 355.000 | 355.000 | 355.000 | 276.900 | 166.850 | 81.650 | 39.050 |